ACS OMEGA

http://pubs.acs.org/journal/acsodf Article

Using Molecular Simulations to Unravel the Benefits of Characterizing Mixture Permeation in Microporous Membranes in Terms of the Spreading Pressure

Rajamani Krishna* and Jasper M. van Baten

Cite This: *ACS Omega* 2020, 5, 32769–32780

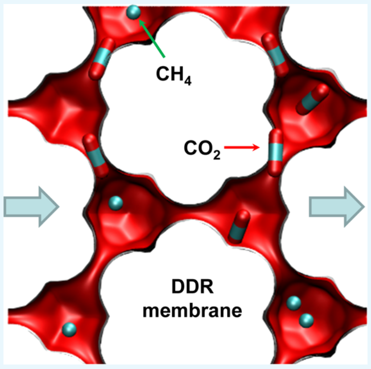

ABSTRACT: The separation performance of microporous crystalline materials in membrane constructs is dictated by a combination of mixture adsorption and intracrystalline diffusion characteristics; the permeation selectivity S_{perm} is a product of the adsorption selectivity S_{ads} and the diffusion selectivity, S_{diff}. The primary objective of this article is to gain fundamental insights into S_{ads} and S_{diff} by use of molecular simulations. We performed configurational-bias Monte Carlo (CBMC) simulations of mixture adsorption equilibrium and molecular dynamics (MD) simulations of guest self-diffusivities of a number of binary mixtures of light gaseous molecules (CO_2, CH_4, N_2, H_2, and C_2H_6) in a variety of microporous hosts of different pore dimensions and topologies. Irrespective of the bulk gas compositions and bulk gas fugacities, the adsorption selectivity, S_{ads}, is found to be uniquely determined by the adsorption potential, Φ, a convenient and practical proxy for the spreading pressure π that is calculable using the ideal adsorbed solution theory for mixture adsorption equilibrium. The adsorption potential Φ is also a proxy for the pore occupancy and is the thermodynamically appropriate yardstick to determine the loading and composition dependences of intracrystalline diffusivities and diffusion selectivities, S_{diff}. When compared at the same Φ, the component permeabilities, Π_i for CO_2, CH_4, and N_2, determinable from CBMC/MD data, are found to be independent of the partners in the various mixtures investigated and have practically the same values as the values for the corresponding unary permeabilities. In all investigated systems, the H_2 permeability in a mixture is significantly lower than the corresponding unary value. These reported results have important practical consequences in process development and are also useful for screening of materials for use as membrane devices.

1. INTRODUCTION

Membrane technologies find applications in a variety of separation applications such as gas separations and water/alcohol pervaporation.[1−5] The perm-selective membrane layers often consist of crystalline microporous materials such as zeolites (alumino-silicates),[6−12] metal−organic frameworks (MOFs),[13] or zeolitic imidazolate frameworks (ZIFs).[14−16]

For any given application, the separation performance of a microporous membrane is characterized by two metrics: permeability and permeation selectivity. The permeability of component i is defined as follows

$$\Pi_i = \frac{N_i}{\Delta f_i/\delta} \tag{1}$$

where N_i is the permeation flux and $\Delta f_i = f_i - f_{i\delta}$ is the difference in the partial fugacities between the upstream (f_i) and downstream ($f_{i\delta}$) faces of the membrane layer of thickness δ. Often, the component permeances, defined by $N_i/\Delta f_i \equiv \Pi_i/\delta$, are more easily accessible from experiments because of uncertainties in the precise values of the membrane thickness, δ. For binary mixtures, the membrane permeation selectivity, S_{perm}, is defined as the ratio of the component permeabilities

$$S_{\mathrm{perm}} = \frac{\Pi_1}{\Pi_2} \tag{2}$$

Following Robeson,[17] it is a common practice to plot the experimental data on S_{perm} as a function of Π_i for evaluation of membrane materials; the best material would occupy the top right corner of such Robeson plots.[18−21]

If the partial fugacities of the components at the downstream face are negligibly small in comparison with those at the upstream face, $\Delta f_i \approx f_i$, the component permeabilities may be estimated from

Received: October 28, 2020
Accepted: November 30, 2020
Published: December 10, 2020

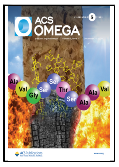

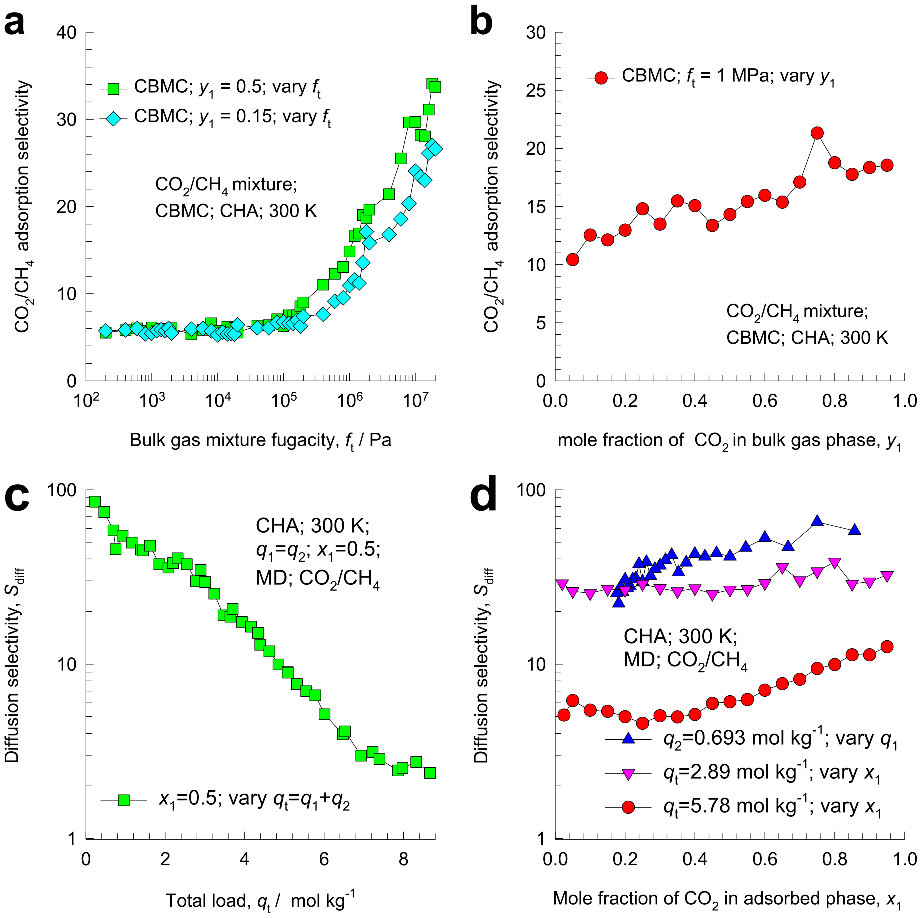

Figure 1. (a,b) CBMC simulations of the adsorption selectivity, S_{ads}, for $CO_2(1)/CH_4(2)$ mixtures in CHA zeolite at 300 K. In the (a) bulk gas-phase, mole fractions are maintained at $y_1 = 0.5$ or $y_1 = 0.15$ and S_{ads} is plotted as a function of the bulk gas mixture fugacity, $f_t = f_1 + f_2$. In the (b) total bulk gas mixture, fugacity is held constant, $f_t = f_1 + f_2 = 10^6$ Pa, and S_{ads} is plotted as a function of the bulk gas mole fraction of CO_2, y_1. (c,d) MD simulations of the diffusion selectivities, S_{diff}, obtained from four different campaigns, plotted as a function of the (c) total load, $q_t = q_1 + q_2$ and (d) mole fraction of CO_2 in the adsorbed phase, $x_1 = q_1/q_t$. All simulation details and input data are provided in the Supporting Information accompanying this publication.

$$\Pi_i = \frac{\rho D_{i,\mathrm{self}} q_i}{f_i} \tag{3}$$

where ρ is the crystal framework density, q_i are the component loadings at the upstream face, and $D_{i,\mathrm{self}}$ are the component self-diffusivities that are readily accessible from either molecular dynamics (MD) simulations or experiments.[19,20,22] Combining eqs 2 and 3, we can express the permeation selectivity S_{perm} as a product of the adsorption selectivity

$$S_{ads} = \frac{q_1/q_2}{f_1/f_2} \tag{4}$$

and diffusion selectivity

$$S_{diff} = \frac{D_{1,\mathrm{self}}}{D_{2,\mathrm{self}}} \tag{5}$$

The detailed derivation of eq 5, starting with the Maxwell–Stefan diffusion formulation,[23,24] is available in earlier works.[19,25] For any guest/host combination, published data from MD simulations and experiments show that the diffusivities $D_{i,\mathrm{self}}$ are strongly dependent on the component loadings q_i.[22,24,26,27] The component loadings, in turn, are strongly dependent on the total fugacity, fluid phase fugacity $f_t = f_1 + f_2$, and gas mixture composition, $y_1 = f_1/f_t$.

As an illustration, Figure 1a,b presents data on S_{ads} obtained from configurational-bias Monte Carlo (CBMC) simulations of $CO_2(1)/CH_4(2)$ mixture adsorption in CHA zeolite at 300 K. CHA zeolite consists of cages of volume 316 Å^3, separated by 8-ring windows of 3.8 Å × 4.2 Å size. Figure 1a shows CBMC data in which the bulk gas-phase mole fractions are maintained at either $y_1 = 0.5$ or $y_1 = 0.15$, and S_{ads} is plotted as a function of the bulk gas mixture fugacity, $f_t = f_1 + f_2$; the value of S_{ads} increases significantly, by about an order of magnitude, with increasing f_t for both sets. Figure 1b shows CBMC data on S_{ads}, for conditions in which the total bulk gas mixture fugacity is held constant, $f_t = f_1 + f_2 = 10^6$ Pa; the S_{ads} is seen to increase with increasing fractions of CO_2 in the bulk gas mixture, y_1.

Figure 1c,d shows MD simulation data for S_{diff} obtained from four different campaigns. When the adsorbed phase composition

$$x_i = q_i/q_t; \qquad q_t = q_1 + q_2; \;\; i = 1,\; 2 \tag{6}$$

is held constant at 0.5, the value of S_{diff} decreases significantly with increased total loading q_t; see Figure 1c. For conditions in which the total loading is held constant, S_{diff} increases with

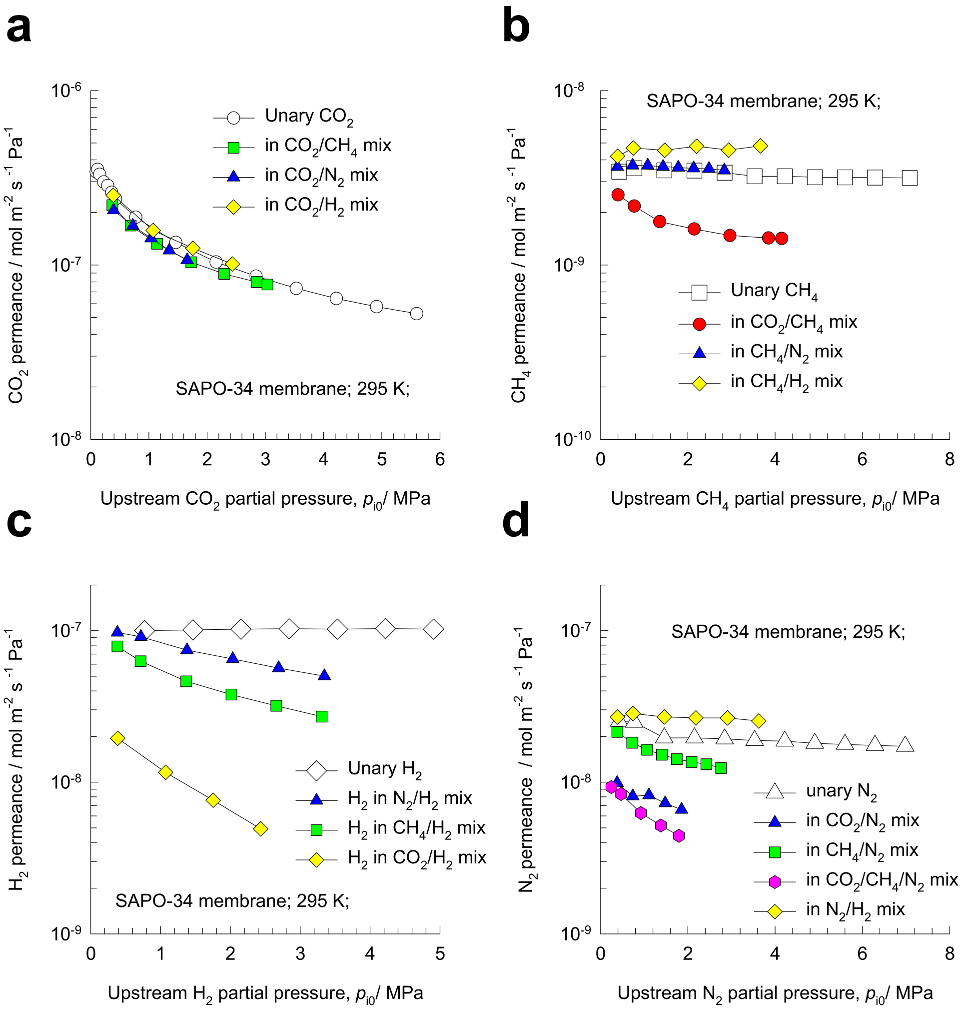

Figure 2. Experimental data[6−8] for permeances of (a) CO_2, (b) CH_4, (c) H_2, and (d) N_2 determined for unary and equimolar binary mixture permeation across the SAPO-34 membrane at 295 K. The permeances are plotted as function of the partial pressures p_i^0 at the upstream face of the membrane. All calculation details and input data are provided in the Supporting Information accompanying this publication.

increasing proportion of CO_2 in the adsorbed phase; see Figure 1d.

On the basis of eqs 3−5 and 7 along with the set of CBMC and MD data on S_{ads} and S_{diff} in Figure 1, we would conclude that the permeation selectivity S_{perm}

$$S_{perm} = S_{ads} \times S_{perm} \tag{7}$$

exhibits a complex dependence of both $f_t = f_1 + f_2$ and y_1 at the upstream face. As a corollary to the composition dependences, we would be prompted to conclude that S_{perm} cannot be estimated on the basis of the data on the permeabilities of the unary guest species. As illustration, Figure 2 presents experimental data[6−8] for permeances of CO_2, CH_4, H_2, and N_2 determined for unary and mixture permeation across the SAPO-34 membrane; SAPO-34 has the same structural topology as CHA zeolite. Compared at the same partial pressures at the upstream face, the CO_2 permeance is hardly influenced by the presence or choice of the partner species in the mixtures. Indeed, the values of CO_2 permeance in any mixture are practically the same as the unary values. The situation is markedly different for the permeances of CH_4, H_2, and N_2. For these less-strongly-adsorbed guest molecules, the component permeances in a mixture depends on choice of the partner species and are usually significantly lower than the corresponding unary permeances. On the basis of the data in Figure 2, we would conclude that the mixture permeation characteristics cannot be estimated on the basis of experimental data on unary permeances.

The primary objective of this article is to gain more fundamental insights into the characteristics of Π_i and S_{perm} in ordered crystalline microporous materials so as to enable their estimations using more easily accessible data inputs on unary adsorption isotherms and unary diffusivities. In particular, we aim to demonstrate the benefits of using the spreading pressure, π, as the thermodynamically correct parameter to quantify the extent of pore occupancy; the π is calculable using the ideal adsorbed solution theory (IAST) of Myers and Prausnitz.[28] We shall establish that data on permeabilities of unary guests may indeed be gainfully employed for prediction of mixture permeation, provided the comparisons are made at the same values of the spreading pressure π.

The desired objectives are met by detailed analysis of CBMC and MD data on adsorption and diffusion of light gaseous molecules (CO_2, CH_4, N_2, H_2, and C_2H_6) and their binary mixtures (CO_2/CH_4, CO_2/N_2, CO_2/H_2, CH_4/H_2, and CH_4/C_2H_6) in a variety of porous crystalline hosts. The host materials are carefully chosen to represent four different pore

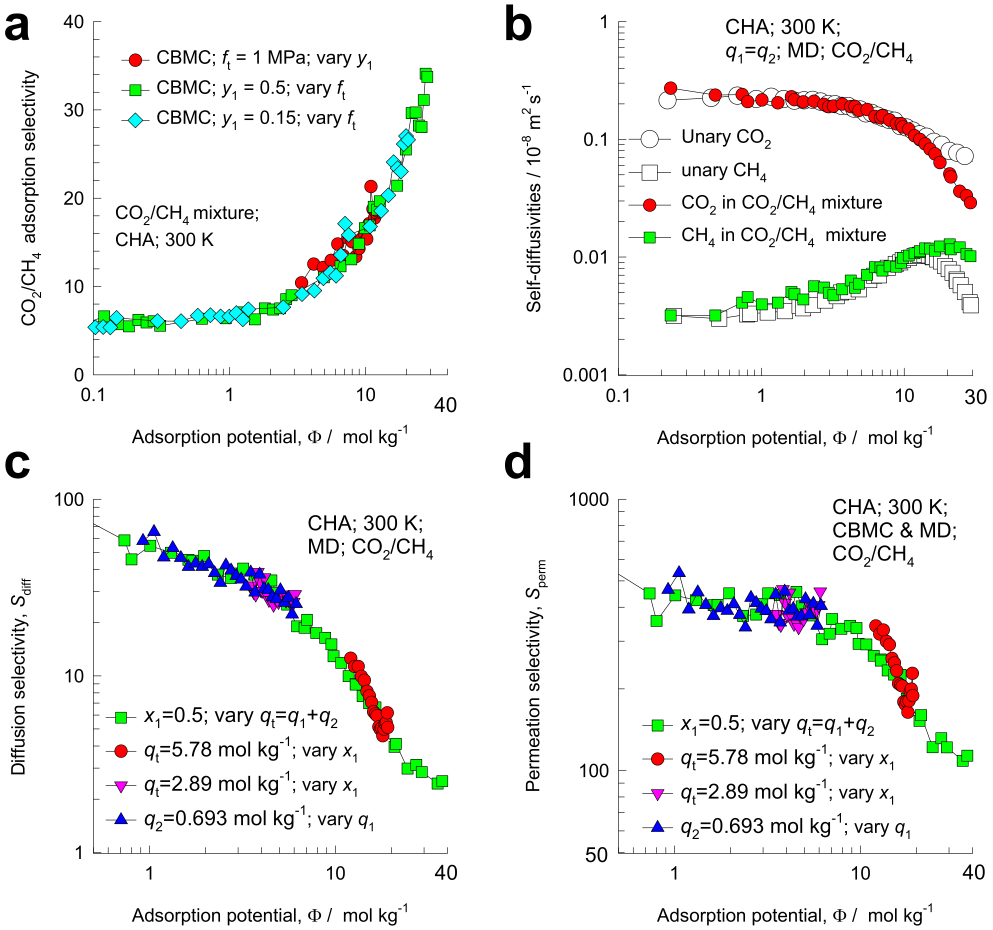

Figure 3. (a) CBMC data on S_{ads} for three different campaigns for $CO_2(1)/CH_4(2)$ mixture adsorption in CHA zeolite at 300 K, plotted as function of the adsorption potential Φ. (b) MD simulations of the self-diffusivities, $D_{i,self}$, of components in equimolar ($q_1 = q_2$) binary CO_2/CH_4 mixtures in CHA, plotted as a function of the adsorption potential, Φ. Also plotted (open symbols) are the corresponding unary self-diffusivities. (c) MD simulations of the diffusion selectivities, S_{diff}, obtained from four different campaigns (see Figure 1c,d), plotted as a function of Φ. (d) Permeation selectivities, S_{perm}, obtained from four different campaigns, plotted as a function of Φ. All simulation details and input data are provided in the Supporting Information accompanying this publication.

topologies: (i) intersecting channels [MFI (≈5.5 Å)], (ii) cages separated by narrow (≈3.3−3.8 Å) windows[29] (CHA, DDR, ZIF-8), and (iii) cavities separated by large (≈7.4 Å) windows (FAU, NaY, NaX), (iv) one-dimensional channels [MgMOF-74 (≈11 Å), and *meso*porous BTP-COF[30] (≈34 Å)]. The Supporting Information accompanying this publication provides (a) detailed structural information on all host materials, (b) CBMC and MD simulation methodologies, (c) CBMC data on unary isotherms and isotherm fits, and (d) CBMC and MD data on adsorption, diffusion, and permeation of variety of mixtures. The entire CBMC and MD data sets are summarized in Figures S9−S55 of the Supporting Information.

2. RESULTS AND DISCUSSION

2.1. Spreading Pressure and Its Proxy.

Within microporous crystalline host materials, the guest constituent molecules exist entirely in the adsorbed phase. The Gibbs adsorption equation in differential form is as follows[31−33]

$$A\,d\pi = \sum_{i=1}^{n} q_i\, d\mu_i \tag{8}$$

In eq 8, A represents the surface area per kg of framework, q_i is the molar loading, μ_i is the molar chemical potential, and π is the spreading pressure. At phase equilibrium, equating the component chemical potentials, μ_i, in the adsorbed phase and in the bulk gas-phase mixture in the upstream membrane compartment, we write

$$d\mu_i = RT\, d\ln f_i \tag{9}$$

The basic equation of IAST of Myers and Prausnitz[28] is the analogue of Raoult's law for vapor−liquid equilibrium that is

$$f_i = P_i^0 x_i; \qquad i = 1,\ 2 \tag{10}$$

where P_i^0 is the pressure for sorption of every component i, which yields the same spreading pressure, π for each of the pure components, as that for the binary mixture

$$\frac{\pi A}{RT} = \int_0^{P_1^0} \frac{q_1^0(f)}{f}\, df = \int_0^{P_2^0} \frac{q_2^0(f)}{f}\, df \tag{11}$$

In eq 11, $q_i^0(f)$ is the *pure* component adsorption isotherm. For general background to the various forms of analytic expressions to model the unary isotherms in different host materials, the reader is referred to the published literature.[34−38] For all of the guest/host combinations considered

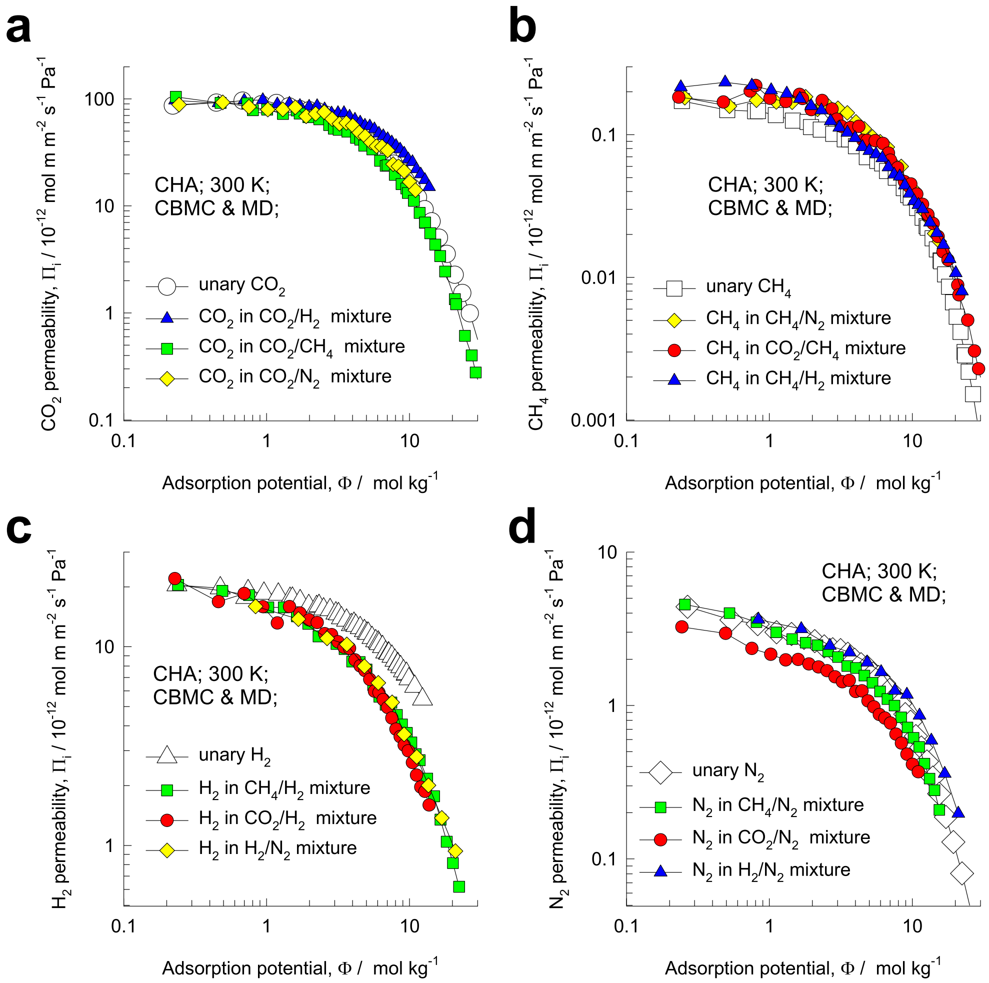

Figure 4. CBMC/MD simulations of the permeabilities, Π_i, of (a) CO$_2$, (b) CH$_4$, (c) H$_2$, and (d) N$_2$ in different equimolar ($q_1 = q_2$) binary mixtures in CHA zeolite at 300 K, plotted as a function of the adsorption potential, Φ. Also plotted (using open symbols) are the corresponding values of the unary permeabilities. All simulation details and input data are provided in the Supporting Information accompanying this publication.

in this article, the unary isotherms, determined from CBMC, are accurately described by the dual-Langmuir−Freundlich model

$$q^0(f) = q_{A,\mathrm{sat}}\frac{b_A f^{\nu_A}}{1 + b_A f^{\nu_A}} + q_{B,\mathrm{sat}}\frac{b_B f^{\nu_B}}{1 + b_B f^{\nu_B}} \tag{12}$$

Each of the integrals in eq 11 can be evaluated analytically

$$\begin{aligned}\frac{\pi A}{RT} &= \int_{f=0}^{P_i^0}\frac{q_i^0(f)}{f}\,\mathrm{d}f\\ &= \frac{q_{A,\mathrm{sat}}}{\nu_A}\ln(1 + b_A(P_i^0)^{\nu_A}) + \frac{q_{B,\mathrm{sat}}}{\nu_B}\ln(1 + b_B(P_i^0)^{\nu_B})\end{aligned} \tag{13}$$

Because the surface area A is not directly accessible from experimental data, the adsorption potential $\pi A/RT \equiv \Phi$,[39−43] with the units mol kg^{-1}, serves as a convenient and practical proxy for the spreading pressure π. For binary mixture adsorption, each of the equalities on the right hand side of eq 11 must be satisfied. These constraints may be solved using a suitable equation solver, to yield the set of values of P_1^0 and P_2^0, both of which satisfy eq 11.

In view of eq 10, we rewrite 4 as the ratio of the sorption pressures

$$S_{\mathrm{ads}} = \frac{x_1/f_1}{x_2/f_2} = \frac{P_2^0}{P_1^0} \tag{14}$$

Applying the restriction specified by eq 11, it follows that S_{ads} is uniquely determined by the adsorption potential Φ; this represents a significant simplification.

A further physical interpretation of Φ becomes transparent if we consider the simple scenario in which each isotherm is described by the single-site Langmuir model with equal saturation capacities for each constituent

$$q_i^0(f) = q_{\mathrm{sat}}\frac{b_i f}{1 + b_i f}; \qquad i = 1,\ 2 \tag{15}$$

The following explicit expression can be derived (see Supporting Information for details)

$$\Phi = q_{\mathrm{sat}}\ln(1 + b_1 f_1 + b_2 f_2) \tag{16}$$

The fractional occupancy, θ, is related to the adsorption potential

$$\theta \equiv \frac{q_t}{q_{\mathrm{sat}}} = 1 - \exp\left(-\frac{\Phi}{q_{\mathrm{sat}}}\right) \tag{17}$$

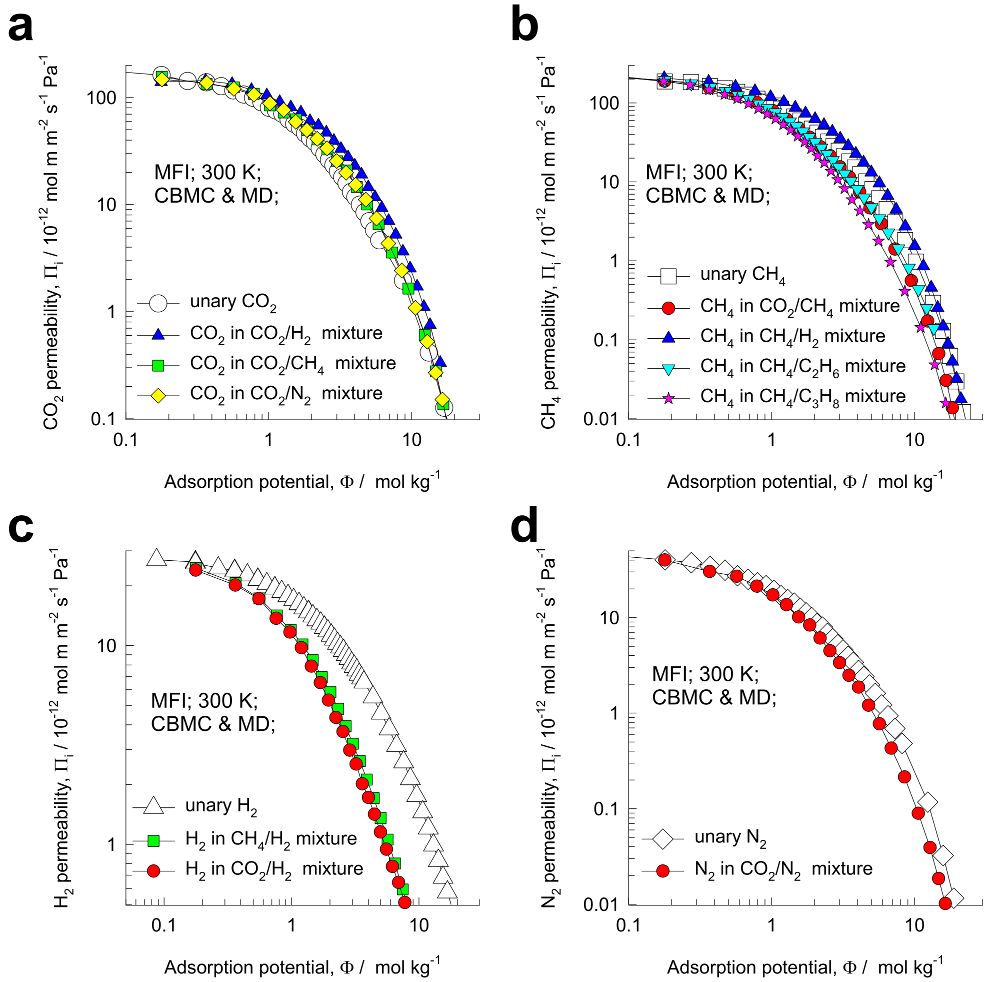

Figure 5. CBMC/MD simulations of the permeabilities, Π_i, of (a) CO_2, (b) CH_4, (c) H_2, and (d) N_2 in different equimolar ($q_1 = q_2$) binary mixtures in MFI zeolite at 300 K, plotted as a function of the adsorption potential, Φ. Also plotted (using open symbols) are the corresponding values of the unary permeabilities. All calculation details and input data are provided in the Supporting Information accompanying this publication.

Typically for separation of gaseous mixtures considered in this article, values of $\Phi \approx 30{-}40$ mol kg^{-1} correspond to pore saturation conditions, $\theta \approx 1$. Equation 17 implies that Φ may also be interpreted as a proxy for the pore occupancy. Consequently, Φ is also the thermodynamically appropriate parameter to describe the loading dependence of diffusivities in microporous materials, as has been established in earlier publications.[27,44] Further background on the wide variety of loading dependences of guest molecules in nanoporous materials is available in the published literature.[45−49] The presence of surface barriers has also been demonstrated to have a significant influence of the guest diffusivities.[50−54]

Armed with these physical insights, let us revisit the set of CBMC and MD data presented in Figure 1.

2.2. Binary Mixture Permeation in Microporous Materials.

In Figure 3a, we plot the data for three different CBMC campaigns for mixture adsorption (as presented in Figure 1a,b), in terms of S_{ads} versus Φ. All data sets fall on a unique curve, confirming that S_{ads} is indeed uniquely determined by Φ.

In Figure 3b, MD simulations of the self-diffusivities, $D_{i,self}$, in equimolar ($q_1 = q_2$) binary CO_2/CH_4 mixtures in CHA are plotted as a function of Φ. These self-diffusivities are nearly equal to the corresponding values for the unary guests, when compared at the same Φ value. This result suggests that Φ also uniquely determines the diffusion selectivities. As verification, Figure 3c demonstrates that the four different MD campaigns (cf. Figure 1c,d) for S_{diff} coincide to yield a unique dependence on Φ. For the same four MD campaigns, the product of S_{diff} with the corresponding values of S_{ads} are plotted in Figure 3d to conclude that S_{perm} is also uniquely related to Φ.

Analogous sets of CBMC and MD data for adsorption and diffusion of CO_2/H_2, CO_2/N_2, CH_4/H_2, CH_4/N_2, and H_2/N_2 mixtures in CHA were gathered (see Figures S23 and S24) and used to examine the permeabilities of CO_2, CH_4, H_2, and N_2 in the presence of different partners with the values of unary permeabilities; see Figure 4. When inspected at the same Φ, the component permeabilities for CO_2, CH_4, and N_2 are found to be independent of the partners in the mixtures and have practically the same values as the values for the corresponding unary permeabilities. This represents an important result of practical consequences in membrane process development. For H_2, that has a very high mobility but extremely poor adsorption strength; the unary permeability is significantly higher than that in the different mixtures. The lowering in the permeabilities of H_2 in the different mixtures is attributable to mixture adsorption that

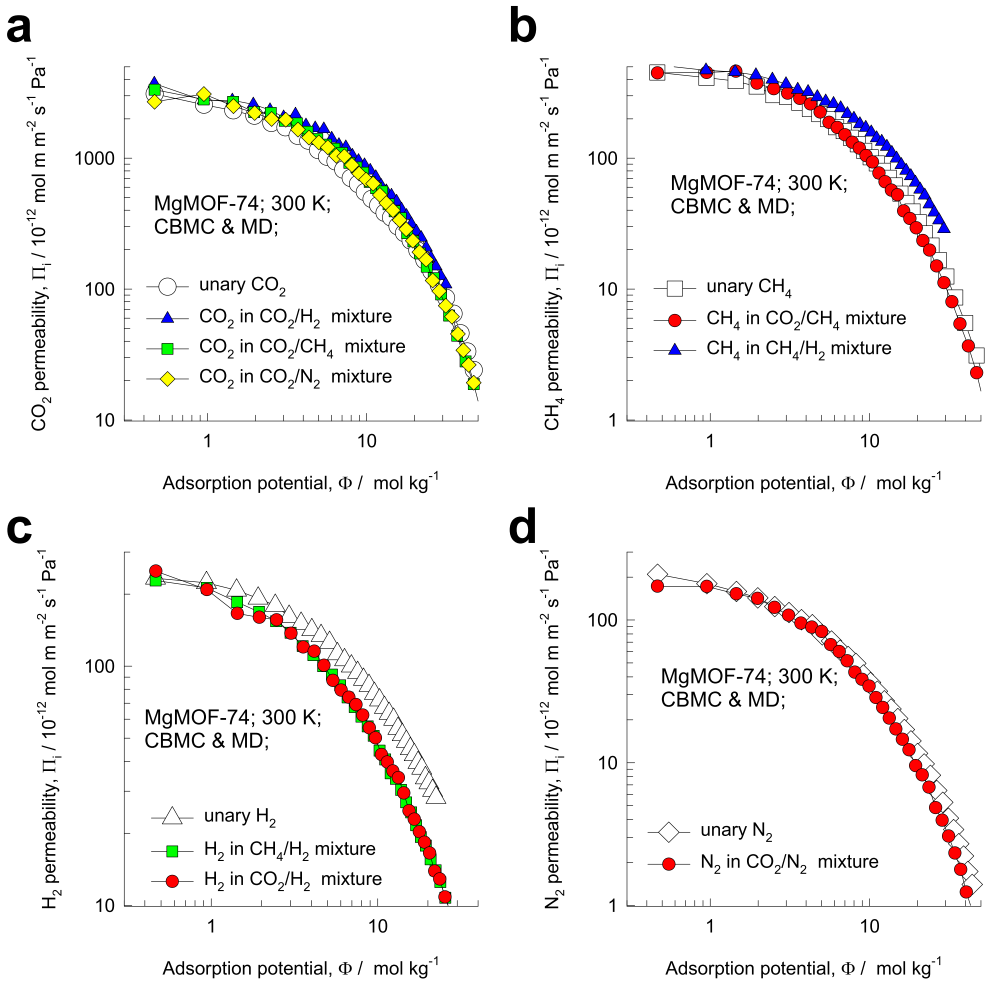

Figure 6. CBMC/MD simulations of the permeabilities, Π_i, of (a) CO_2, (b) CH_4, (c) H_2, and (d) N_2 in different equimolar ($q_1 = q_2$) binary mixtures in MgMOF-74 zeolite at 300 K, plotted as a function of the adsorption potential, Φ. Also plotted (using open symbols) are the corresponding values of the unary permeabilities. All calculation details and input data are provided in the Supporting Information accompanying this publication.

favors the different partners CO_2, CH_4, and N_2 to a significant extent. The more strongly adsorbed partner species also have the effect of retarding the intercage hopping of H_2 molecules.[55]

Results entirely analogous to those presented in Figure 4 are obtained for all other microporous materials investigated with different pore sizes and topologies. As illustration, Figures 5 and 6 present the CBMC/MD data for permeabilities of the four different guests within the intersecting channel structures of MFI and 1D channels of MgMOF-74. The data for other host materials are presented in Figures S26−S55. In all cases, the unary permeabilities for CO_2, CH_4, and N_2 are practically the same as the values in different binary mixtures, when compared at the same Φ. For H_2, the permeabilities in the mixtures are significantly lower than the unary values.

Experimental verification that the data such as these illustrated in Figures 4, 5, and 6 are available for a wide variety of guest/host combinations; see earlier work.[44] For CO_2/H_2 permeation in MFI, for example, a fundamental re-analysis[44] of the experimental data of Sandström et al.[10] provides confirmation that the permeability of H_2 in mixtures with CO_2 is significantly lowered by about an order of magnitude below the value for unary H_2 permeation. For permeation of various mixtures across the SAPO-34 membrane, the same set of experimental data in Figure 2, is plotted in Figure 7 as functions of Φ, determined at the upstream membrane face. With use of Φ as the yardstick, the component permeances of each of the four guests are found to be practically independent of partner species, in consonance with the data in Figure 4. The comparisons between the plots in Figures 2 and 7 accentuate the advantages of the use of Φ as yardsticks for comparison of unary permeances with those in various mixtures.

Published MD data for mixture diffusion have shown that the occurrence of molecular clustering, because of say hydrogen bonding, causes the component diffusivities in mixtures to deviate significantly from the values for the corresponding unaries.[25,26,43,56−62]

2.3. Screening of Microporous Materials in Membrane Applications. Having established the benefits of using Φ, a practical proxy for spreading pressure, as a convenient tool for relating component permeabilities in binary mixtures to unary permeabilities, we turn to the process of screening membrane materials for any specific separation applications. Consider CO_2/CH_4 mixture separations that is of relevance in purification of natural gas, which can contain up to 92% CO_2 impurity at its source.[63,64] Removal of CO_2, which is most

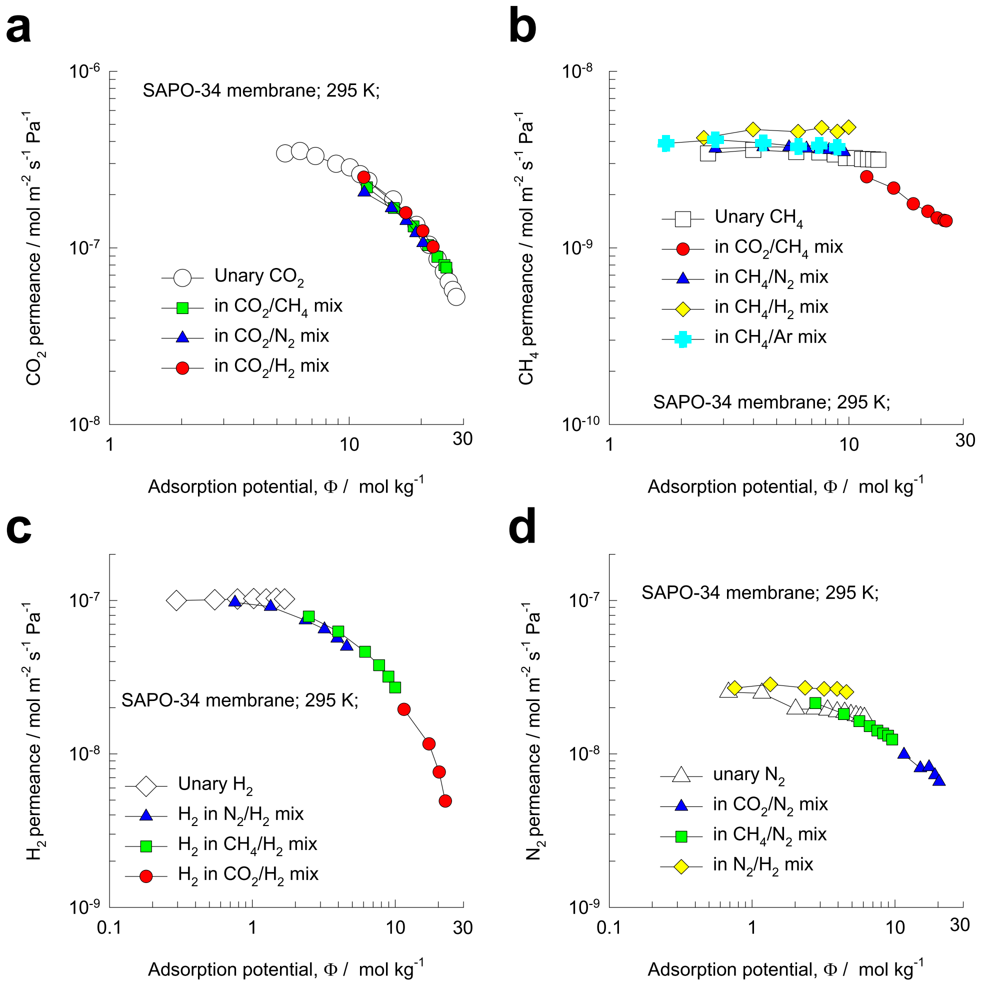

Figure 7. Experimental data[6−8] for permeances of (a) CO_2, (b) CH_4, (c) H_2, and (d) N_2 determined for unary and equimolar binary mixture permeation across the SAPO-34 membrane at 295 K. The permeances are plotted as a function of the adsorption potential Φ, calculated at the upstream face of the membrane. All calculation details and input data are provided in the Supporting Information accompanying this publication.

commonly accomplished using amines, is conducted at pressures ranging to about 2 MPa.[64,65] CBMC simulations were carried out for equimolar $f_1 = f_2$ CO_2/CH_4 mixtures in different host materials. The values of the adsorption selectivities, S_{ads}, are plotted in Figure 8a as function of Φ. The highest values of S_{ads} are realized with cation-exchanged zeolites (NaX and NaY) and MgMOF-74 with exposed Mg^{2+} cation sites, resulting in strong binding of CO_2 molecules to cations.[66,67] Significantly lower S_{ads} values are realized with all-silica zeolites. Remarkably, the hierarchy of diffusion selectivities is essentially the reverse of the hierarchy of S_{ads}; see MD simulation data for S_{diff} versus Φ in Figure 8b. The highest diffusion selectivities are obtained with DDR, CHA, and ZIF-8 that consist of cages separated by narrow (≈3.3−3.8 Å) windows. In such structures, CO_2 jumps length-wise across the windows as evidenced in video animations.[29,68] The smaller cross-sectional dimension (cf. Figure 8c) of CO_2 (3.1 Å) compared to CH_4 (3.7 Å) accounts for the significantly higher S_{diff} in favor of CO_2.

Figure 8b also shows that the diffusion selectivities in host materials with larger characteristic pore dimensions (FAU, NaY, NaX, MFI, MgMOF-74, and BTP-COF) in which the guest molecules are less strongly constrained, the S_{diff} favors CH_4 that has the *larger* kinetic diameter. This apparent paradox is accentuated by the comparison of the data for FAU, NaY, and NaX; these three materials have the same pore size and topology consisting of cavities (≈11 Å) separated by 12-ring windows (≈7.4 Å) but display the S_{diff} hierarchy FAU > NaY > NaX. Clearly, the S_{diff} is determined by factors other than pore size and degree of guest confinement.[26,69,70] The observed hierarchy of S_{diff} values can be rationalized on the basis of the stronger binding strength of CO_2. Figure 8d plots the CBMC simulation data on isosteric heats of adsorption, Q_{st}, a measure of the binding energy of CO_2, as function of Φ. The hierarchy of Q_{st} is NaX > NaY ≈ MgMOF-74 > MFI > FAU ≈ BTP-COF is precisely the reverse of the hierarchy of S_{diff} found in Figure 8b. Stronger binding of CO_2 implies higher degree of "stickiness" and, consequently, lower mobility.[69,70]

Figure 9a,b compares the values of the permeation selectivity $S_{perm} = S_{ads} \times S_{perm}$ and CO_2 permeabilities Π_1 in different materials. The hierarchies of these two important metrics governing membrane separations are not precisely the reverse of each other, suggesting that there is room for optimizing the choice of material. For specific choice of upstream operating conditions, $f_t = f_1 + f_2 = 10^6$ Pa, Figure 9c shows the Robeson plot of S_{perm} versus Π_1. The highest S_{perm} values in excess of 100 are obtained with zeolites with 8-ring windows DDR and CHA, for which S_{ads}, and S_{diff} complement each other. For DDR and CHA, there is experimental

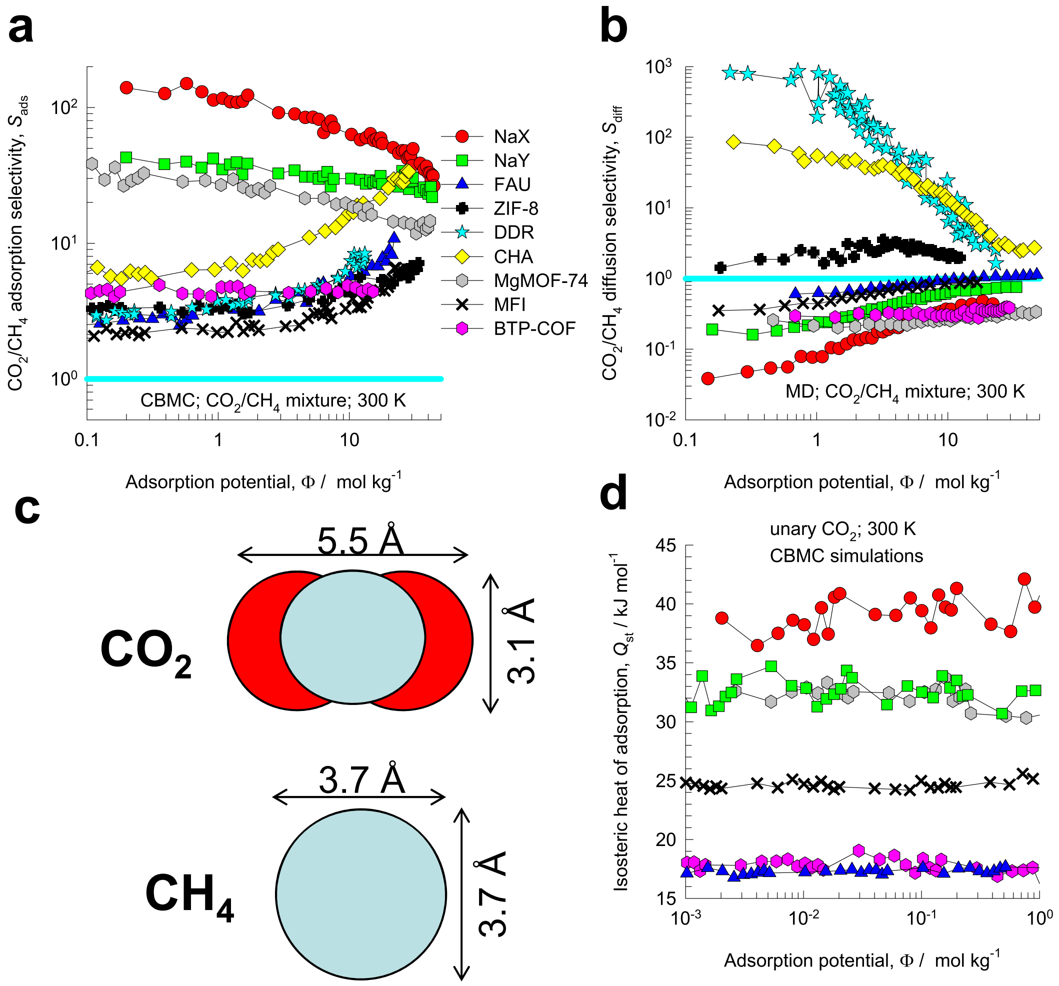

Figure 8. Comparison of (a) adsorption selectivity, S_{ads}, and (b) diffusion selectivity, S_{diff}, for $CO_2(1)/CH_4(2)$ mixtures in microporous materials; the *x*-axis represents the adsorption potential, Φ. (c) Molecular dimensions of CO_2 and CH_4. (d) Isosteric heats of adsorption of CO_2 determined from CBMC simulations. All calculation details and input data are provided in the Supporting Information accompanying this publication.

evidence that such high permeation selectivities can be realized in practice.[6−8,11,55,71−73] For MFI, the S_{perm} value of 2.3 is in agreement with the experiment.[6] The stronger CO_2 binding achievable using NaY, NaX, and MgMOF-74 does not guarantee high permeation selectivities. There is considerable scope for development of novel materials that would lead to a performance at the top right corner of the Robeson plot, using mixed-matrix membranes that attempt to profit from both adsorption and diffusion characteristics of the constituent materials.[4,18]

Analogous Robeson plots constructed by CBMC/MD data for CO_2/N_2 and CO_2/H_2 separations are shown in Figures S57−S58.

3. CONCLUSIONS

The adsorption and diffusion characteristics of a variety of mixtures (CO_2/CH_4, CO_2/N_2, CO_2/H_2, CH_4/H_2, and CH_4/C_2H_6) in a variety of microporous hosts (CHA, DDR, ZIF-8, BTP-COF, MgMOF-74, FAU, NaY, NaX, and MFI) were investigated using CBMC and MD simulations. The following major conclusions emerge from a detailed analysis of the obtained results.

(1) The adsorption potential, Φ, a proxy for the spreading pressure and calculable from the IAST, is a proper yardstick to compare data on adsorption, diffusion, and permeation in microporous materials.

(2) For adsorption of binary mixtures of light gaseous constituents (CO_2, CH_4, N_2, H_2, and C_2H_6), the adsorption selectivity S_{ads} is uniquely determined by the adsorption potential, Φ, irrespective of mixture composition and total fugacity, f_t.

(3) The adsorption potential Φ also serves as the thermodynamically appropriate proxy to represent the pore occupancy. As a consequence, the diffusion selectivity S_{diff} is also uniquely dependent on Φ.

(4) When compared at the same Φ, the component permeabilities, Π_i, for CO_2, CH_4, and N_2, determinable from CBMC/MD data using eq 3, are found to be largely independent of the partners in the various mixtures investigated and have practically the same values as the values for the corresponding unary permeabilities. This simple result, verified in a number of experimental investigations,[44] has important consequences for membrane process development.

(5) In all investigated mixtures, the permeability of H_2 falls significantly below the values of the unary permeabilities.

(6) As exemplified in Figure 8 for CO_2/CH_4 separation, the hierarchy of S_{ads} versus Φ data are found to be precisely

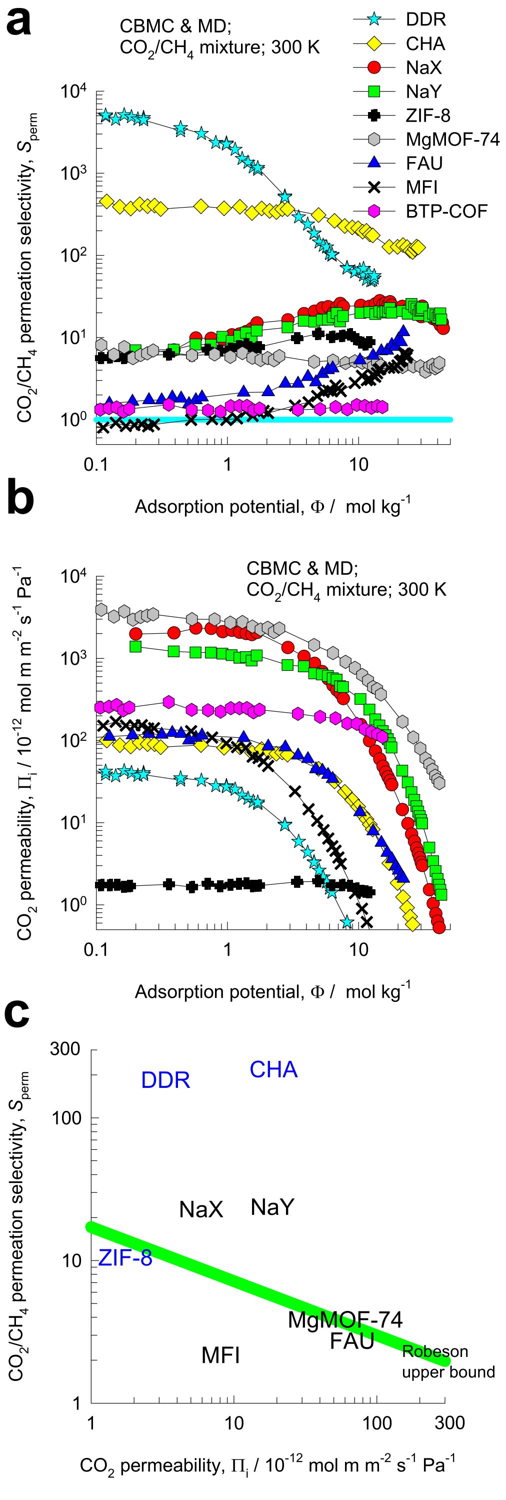

Figure 9. Comparison of (a) permeation selectivity, S_{perm}, and (b) CO_2 permeability, Π_1, for $CO_2(1)/CH_4(2)$ mixtures in different microporous materials; the x-axis represents the adsorption potential, Φ. (c) Robeson plot of S_{perm} versus Π_1 data at $f_t = f_1 + f_2 = 10^6$ Pa and 300 K. All calculation details and input data are provided in the Supporting Information accompanying this publication.

opposite to the hierarchy of S_{diff} versus Φ data. This underscores the fact that adsorption and diffusion do not go hand-in-hand. In host materials wherein the guests are not too strongly confined (FAU, NaY, NaX, MFI, MgMOF-74, BTP-COF), stronger binding of CO_2 results in lower mobility.

(7) The insights gained in this investigation assist in the choice of the appropriate membrane material for a specified separation, appropriately balancing adsorption selectivity with diffusion selectivity.

■ ASSOCIATED CONTENT

Supporting Information

The Supporting Information is available free of charge at https://pubs.acs.org/doi/10.1021/acsomega.0c05269.

Detailed structural information on all host materials, CBMC and MD simulation methodologies, CBMC data on unary isotherms and isotherm fits, CBMC and MD data on adsorption, diffusion, and permeation of variety of mixtures (PDF)

■ AUTHOR INFORMATION

Corresponding Author

Rajamani Krishna − *Van't Hoff Institute for Molecular Sciences, University of Amsterdam, 1098 XH Amsterdam, The Netherlands;* orcid.org/0000-0002-4784-8530; Email: r.krishna@contact.uva.nl

Author

Jasper M. van Baten − *Van't Hoff Institute for Molecular Sciences, University of Amsterdam, 1098 XH Amsterdam, The Netherlands*

Complete contact information is available at: https://pubs.acs.org/10.1021/acsomega.0c05269

Notes

The authors declare no competing financial interest.

■ ACKNOWLEDGMENTS

The authors acknowledge Dr. Richard Baur for helpful discussions.

■ NOMENCLATURE

Latin alphabet

A = surface area per kg of framework, $m^2\ kg^{-1}$
b = dual-Langmuir−Freundlich constant, $Pa^{-\nu}$
$D_{i,self}$ = self-diffusivity of species i, $m^2\ s^{-1}$
f_i = partial fugacity of species i, Pa
f_t = total fugacity of bulk fluid mixture, Pa
N_i = molar flux of species i with respect to framework, mol $m^{-2}\ s^{-1}$
P_i^0 = sorption pressure, Pa
q_i = component molar loading of species i, mol kg^{-1}
$q_{i,sat}$ = molar loading of species i at saturation, mol kg^{-1}
q_t = total molar loading in mixture, mol kg^{-1}
Q_{st} = isosteric heat of adsorption, J mol^{-1}
R = gas constant, 8.314 J $mol^{-1}\ K^{-1}$
S_{ads} = adsorption selectivity, dimensionless
S_{diff} = diffusion selectivity, dimensionless
S_{perm} = permeation selectivity, dimensionless
T = absolute temperature, K
x_i = mole fraction of species i in adsorbed phase, dimensionless
y_i = mole fraction of species i in bulk gas phase, dimensionless

Greek alphabet

δ = thickness of membrane, m
μ_i = molar chemical potential of component i, J mol^{-1}
π = spreading pressure, N m^{-1}
θ = fractional occupancy, dimensionless
ν = exponent in dual-Langmuir−Freundlich isotherm, dimensionless
Π_i = membrane permeability of species i, mol m m^{-2} s^{-1} Pa^{-1}
ρ = framework density, kg m^{-3}
Φ = adsorption potential, mol kg^{-1}

Subscripts

1 = referring to component 1
2 = referring to component 2
i = referring to component i
t = referring to total mixture
sat = referring to saturation conditions

■ REFERENCES

(1) Baker, R. W. *Membrane Technology and Applications*, 3rd ed; John Wiley: New York, 2012.

(2) Wesselingh, J. A.; Krishna, R. *Mass transfer in multicomponent mixtures*; VSSD: Delft, 2000.

(3) Caro, J. Are MOF membranes better in gas separation than those made of zeolites? *Curr. Opin. Chem. Eng.* **2011**, *1*, 77−83.

(4) Rangnekar, N.; Mittal, N.; Elyassi, B.; Caro, J.; Tsapatsis, M. Zeolite Membranes −A Review and Comparison with MOFs. *Chem. Soc. Rev.* **2015**, *44*, 7128−7154.

(5) Pera-Titus, M. Porous Inorganic Membranes for CO2 Capture: Present and Prospects. *Chem. Rev.* **2014**, *114*, 1413−1492.

(6) Krishna, R.; Li, S.; van Baten, J. M.; Falconer, J. L.; Noble, R. D. Investigation of slowing-down and speeding-up effects in binary mixture permeation across SAPO-34 and MFI membranes. *Sep. Purif. Technol.* **2008**, *60*, 230−236.

(7) Li, S.; Falconer, J. L.; Noble, R. D.; Krishna, R. Modeling permeation of CO_2/CH_4, CO_2/N_2, and N_2/CH_4 mixtures across SAPO-34 membrane with the Maxwell-Stefan equations. *Ind. Eng. Chem. Res.* **2007**, *46*, 3904−3911.

(8) Li, S.; Falconer, J. L.; Noble, R. D.; Krishna, R. Interpreting unary, binary and ternary mixture permeation across a SAPO-34 membrane with loading-dependent Maxwell-Stefan diffusivities. *J. Phys. Chem. C* **2007**, *111*, 5075−5082.

(9) Feng, X.; Zong, Z.; Elsaidi, S. K.; Jasinski, J. B.; Krishna, R.; Thallapally, P. K.; Carreon, M. A. Kr/Xe Separation over a Chabazite Zeolite Membrane. *J. Am. Chem. Soc.* **2016**, *138*, 9791−9794.

(10) Sandström, L.; Sjöberg, E.; Hedlund, J. Very high flux MFI membrane for CO_2 separation. *J. Membr. Sci.* **2011**, *380*, 232−240.

(11) van den Bergh, J.; Zhu, W.; Gascon, J.; Moulijn, J. A.; Kapteijn, F. Separation and Permeation Characteristics of a DD3R Zeolite Membrane. *J. Membr. Sci.* **2008**, *316*, 35−45.

(12) van de Graaf, J. M.; Kapteijn, F.; Moulijn, J. A. Modeling permeation of binary mixtures through zeolite membranes. *AIChE J.* **1999**, *45*, 497−511.

(13) Qian, Q.; Asinger, P. A.; Lee, M. J.; Han, G.; Mizrahi Rodriguez, K.; Lin, S.; Benedetti, F. M.; Wu, A. X.; Chi, W. S.; Smith, Z. P. MOF-Based Membranes for Gas Separations. *Chem. Rev.* **2020**, *120*, 8161−8266.

(14) Bux, H.; Chmelik, C.; Krishna, R.; Caro, J. Ethene/Ethane Separation by the MOF Membrane ZIF-8: Molecular Correlation of Permeation, Adsorption, Diffusion. *J. Membr. Sci.* **2011**, *369*, 284−289.

(15) Bux, H.; Chmelik, C.; Van Baten, J. M.; Krishna, R.; Caro, J. Novel MOF-Membrane for Molecular Sieving Predicted by IR-Diffusion Studies and Molecular Modeling. *Adv. Mater.* **2010**, *22*, 4741−4743.

(16) Chmelik, C.; van Baten, J.; Krishna, R. Hindering effects in diffusion of CO_2/CH_4 mixtures in ZIF-8 crystals. *J. Membr. Sci.* **2012**, *397−398*, 87−91.

(17) Robeson, L. M. The upper bound revisited. *J. Membr. Sci.* **2008**, *320*, 390−400.

(18) Liu, G.; Chernikova, V.; Liu, Y.; Zhang, K.; Belmabkhout, Y.; Shekhah, O.; Zhang, C.; Yi, S.; Eddaoudi, M.; Koros, W. J. Mixed Matrix Formulations with MOF Molecular Sieving for Key Energy-intensive Separations. *Nat. Mater.* **2018**, *17*, 283−289.

(19) Krishna, R.; van Baten, J. M. In Silico Screening of Zeolite Membranes for CO_2 Capture. *J. Membr. Sci.* **2010**, *360*, 323−333.

(20) Krishna, R.; van Baten, J. M. In silico screening of metal-organic frameworks in separation applications. *Phys. Chem. Chem. Phys.* **2011**, *13*, 10593−10616.

(21) Krishna, R. Methodologies for Screening and Selection of Crystalline Microporous Materials in Mixture Separations. *Sep. Purif. Technol.* **2018**, *194*, 281−300.

(22) Kärger, J.; Ruthven, D. M.; Theodorou, D. N. *Diffusion in Nanoporous Materials*; Wiley-VCH: Weinheim, 2012.

(23) Krishna, R. The Maxwell-Stefan Description of Mixture Diffusion in Nanoporous Crystalline Materials. *Microporous Mesoporous Mater.* **2014**, *185*, 30−50.

(24) Krishna, R. Describing the Diffusion of Guest Molecules inside Porous Structures. *J. Phys. Chem. C* **2009**, *113*, 19756−19781.

(25) Krishna, R.; van Baten, J. M. Investigating the Influence of Diffusional Coupling on Mixture Permeation across Porous Membranes. *J. Membr. Sci.* **2013**, *430*, 113−128.

(26) Krishna, R. Diffusion in Porous Crystalline Materials. *Chem. Soc. Rev.* **2012**, *41*, 3099−3118.

(27) Krishna, R. Occupancy Dependency of Maxwell−Stefan Diffusivities in Ordered Crystalline Microporous Materials. *ACS Omega* **2018**, *3*, 15743−15753.

(28) Myers, A. L.; Prausnitz, J. M. Thermodynamics of Mixed Gas Adsorption. *AIChE J.* **1965**, *11*, 121−127.

(29) Krishna, R.; van Baten, J. M. A molecular dynamics investigation of the diffusion characteristics of cavity-type zeolites with 8-ring windows. *Microporous Mesoporous Mater.* **2011**, *137*, 83−91.

(30) Krishna, R.; van Baten, J. M. Investigating the Validity of the Knudsen Prescription for Diffusivities in a Mesoporous Covalent Organic Framework. *Ind. Eng. Chem. Res.* **2011**, *50*, 7083−7087.

(31) Ruthven, D. M. *Principles of Adsorption and Adsorption Processes*; John Wiley: New York, 1984.

(32) Krishna, R.; van Baten, J. M.; Baur, R. Highlighting the Origins and Consequences of Thermodynamic Nonidealities in Mixture Separations using Zeolites and Metal-Organic Frameworks. *Microporous Mesoporous Mater.* **2018**, *267*, 274−292.

(33) Krishna, R.; Van Baten, J. M. Investigating the Non-idealities in Adsorption of CO_2-bearing Mixtures in Cation-exchanged Zeolites. *Sep. Purif. Technol.* **2018**, *206*, 208−217.

(34) Polanyi, M. The Potential Theory of Adsorption. *Science* **1963**, *141*, 1010−1013.

(35) Jaroniec, M. Analytical Approximations for Spreading Pressure Corresponding to Different Adsorption Isotherms. *Z. Phys. Chem.* **1977**, *258*, 247−256.

(36) Kumar, K. V.; Gadipelli, S.; Wood, B.; Ramisetty, K. A.; Stewart, A. A.; Howard, C. A.; Brett, D. J. L.; Rodriguez-Reinoso, F. Characterization of the adsorption site energies and heterogeneous surfaces of porous materials. *J. Mater. Chem. A* **2019**, *7*, 10104−10137.

(37) Wang, J.; Guo, X. Adsorption isotherm models: Classification, physical meaning, application and solving method. *Chemosphere* **2020**, *258*, 127279.

(38) Dabrowski, A. Adsorption — from theory to practice. *Adv. Colloid Interface Sci.* **2001**, *93*, 135−224.

(39) Talu, O.; Myers, A. L. Rigorous Thermodynamic Treatment of Gas-Adsorption. *AIChE J.* **1988**, *34*, 1887−1893.

(40) Siperstein, F. R.; Myers, A. L. Mixed-Gas Adsorption. *AIChE J.* **2001**, *47*, 1141−1159.

(41) Krishna, R.; Van Baten, J. M. Elucidation of Selectivity Reversals for Binary Mixture Adsorption in Microporous Adsorbents. *ACS Omega* **2020**, *5*, 9031−9040.

(42) Krishna, R.; Van Baten, J. M. Using Molecular Simulations for Elucidation of Thermodynamic Non-Idealities in Adsorption of CO_2-containing Mixtures in NaX Zeolite. *ACS Omega* **2020**, *5*, 20535−20542.

(43) Krishna, R.; Van Baten, J. M. Water/Alcohol Mixture Adsorption in Hydrophobic Materials: Enhanced Water Ingress caused by Hydrogen Bonding. *ACS Omega* **2020**, *5*, 28393−28402.

(44) Krishna, R. Thermodynamic Insights into the Characteristics of Unary and Mixture Permeances in Microporous Membranes. *ACS Omega* **2019**, *4*, 9512−9521.

(45) Beerdsen, E.; Dubbeldam, D.; Smit, B. Loading Dependence of the Diffusion Coefficient of Methane in Nanoporous Materials. *J. Phys. Chem. B* **2006**, *110*, 22754−22772.

(46) Beerdsen, E.; Dubbeldam, D.; Smit, B. Understanding Diffusion in Nanoporous Materials. *Phys. Rev. Lett.* **2006**, *96*, 044501.

(47) Dubbeldam, D.; Beerdsen, E.; Vlugt, T. J. H.; Smit, B. Molecular simulation of loading-dependent diffusion in nanoporous materials using extended dynamically corrected transition state theory. *J. Chem. Phys.* **2005**, *122*, 224712.

(48) Skoulidas, A. I.; Sholl, D. S. Molecular Dynamics Simulations of Self, Corrected, and Transport Diffusivities of Light Gases in Four Silica Zeolites to Assess Influences of Pore Shape and Connectivity. *J. Phys. Chem. A* **2003**, *107*, 10132−10141.

(49) van den Bergh, J.; Ban, S.; Vlugt, T. J. H.; Kapteijn, F. Modeling the Loading Dependency of Diffusion in Zeolites: The Relevant Site Model. *J. Phys. Chem. C* **2009**, *113*, 17840−17850.

(50) Chmelik, C.; Hibbe, F.; Tzoulaki, D.; Heinke, L.; Caro, J.; Li, J.; Kärger, J. Exploring the nature of surface barriers on MOF Zn(tbip) by applying IR microscopy in high temporal and spatial resolution. *Microporous Mesoporous Mater.* **2010**, *129*, 340−344.

(51) Ruthven, D. M.; Vidoni, A. ZLC diffusion measurements: Combined effect of surface resistance and internal diffusion. *Chem. Eng. Sci.* **2012**, *71*, 1−4.

(52) Fasano, M.; Humplik, T.; Bevilacqua, A.; Tsapatsis, M.; Chiavazzo, E.; Wang, E. N.; Asinari, P. Interplay between hydrophilicity and surface barriers on water transport in zeolite membranes. *Nat. Commun.* **2016**, *7*, 12762.

(53) Combariza, A. F.; Sastre, G. Influence of Zeolite Surface in the Sorption of Methane from Molecular Dynamics. *J. Phys. Chem. C* **2011**, *115*, 13751−13758.

(54) Lauerer, A.; Binder, T.; Chmelik, C.; Miersemann, E.; Haase, J.; Ruthven, D. M.; Kärger, J. Uphill Diffusion and Overshooting in the Adsorption of Binary Mixtures in Nanoporous Solids. *Nat. Commun.* **2015**, *6*, 7697.

(55) Krishna, R.; van Baten, J. M. Segregation effects in adsorption of CO_2 containing mixtures and their consequences for separation selectivities in cage-type zeolites. *Sep. Purif. Technol.* **2008**, *61*, 414−423.

(56) Bendt, S.; Dong, Y.; Keil, F. J. Diffusion of Water and Carbon Dioxide and Mixtures Thereof in Mg-MOF-74. *J. Phys. Chem. C* **2019**, *123*, 8212−8220.

(57) Krishna, R.; van Baten, J. M. Hydrogen Bonding Effects in Adsorption of Water-alcohol Mixtures in Zeolites and the Consequences for the Characteristics of the Maxwell-Stefan Diffusivities. *Langmuir* **2010**, *26*, 10854−10867.

(58) Krishna, R.; van Baten, J. M. Mutual slowing-down effects in mixture diffusion in zeolites. *J. Phys. Chem. C* **2010**, *114*, 13154−13156.

(59) Krishna, R.; van Baten, J. M. Maxwell-Stefan modeling of slowing-down effects in mixed gas permeation across porous membranes. *J. Membr. Sci.* **2011**, *383*, 289−300.

(60) Gómez-Álvarez, P.; Noya, E. G.; Lomba, E.; Valencia, S.; Pires, J. Study of Short-Chain Alcohol and Alcohol−Water Adsorption in MEL and MFI Zeolites. *Langmuir* **2018**, *34*, 12739−12750.

(61) Krishna, R. Thermodynamically Consistent Methodology for Estimation of Diffusivities of Mixtures of Guest Molecules in Microporous Materials. *ACS Omega* **2019**, *4*, 13520−13529.

(62) Krishna, R. Using the Maxwell-Stefan formulation for Highlighting the Influence of Interspecies (1-2) Friction on Binary Mixture Permeation across Microporous and Polymeric Membranes. *J. Membr. Sci.* **2017**, *540*, 261−276.

(63) Herm, Z. R.; Swisher, J. A.; Smit, B.; Krishna, R.; Long, J. R. Metal-Organic Frameworks as Adsorbents for Hydrogen Purification and Pre-Combustion Carbon Dioxide Capture. *J. Am. Chem. Soc.* **2011**, *133*, 5664−5667.

(64) Smit, B.; Reimer, J. A.; Oldenburg, C. M.; Bourg, I. C. *Introduction to Carbon Capture and Sequestration*; Imperial College Press: London, 2014.

(65) Rochelle, G. T. Amine Scrubbing for CO_2 Capture. *Science* **2009**, *325*, 1652−1654.

(66) Shigaki, N.; Mogi, Y.; Haraoka, T.; Furuya, E. Measurements and calculations of the equilibrium adsorption amounts of CO_2-N_2, $CO-N_2$, and CO_2-CO mixed gases on 13X zeolite. *SN Appl. Sci.* **2020**, *2*, 488.

(67) Zimmermann, N. E. R.; Jakobtorweihen, S.; Beerdsen, E.; Smit, B.; Keil, F. J. In-Depth Study of the Influence of Host-Framework Flexibility on the Diffusion of Small Gas Molecules in One-Dimensional Zeolitic Pore Systems. *J. Phys. Chem. C* **2007**, *111*, 17370−17381.

(68) Krishna, R.; van Baten, J. M. Using Molecular Dynamics Simulations for Elucidation of Molecular Traffic in Ordered Crystalline Microporous Materials. *Microporous Mesoporous Mater.* **2018**, *258*, 151−169.

(69) Krishna, R.; van Baten, J. M. Investigating the Relative Influences of Molecular Dimensions and Binding Energies on Diffusivities of Guest Species Inside Nanoporous Crystalline Materials. *J. Phys. Chem. C* **2012**, *116*, 23556−23568.

(70) Krishna, R.; van Baten, J. M. Influence of Adsorption Thermodynamics on Guest Diffusivities in Nanoporous Crystalline Materials. *Phys. Chem. Chem. Phys.* **2013**, *15*, 7994−8016.

(71) Himeno, S.; Tomita, T.; Suzuki, K.; Nakayama, K.; Yajima, K. Synthesis and Permeation Properties of a DDR-type zeolite membrane for Separation of CO_2/CH_4 Gaseous Mixtures. *Ind. Eng. Chem. Res.* **2007**, *46*, 6989−6997.

(72) Krishna, R.; van Baten, J. M.; García-Pérez, E.; Calero, S. Incorporating the loading dependence of the Maxwell-Stefan diffusivity in the modeling of CH_4 and CO_2 permeation across zeolite membranes. *Ind. Eng. Chem. Res.* **2007**, *46*, 2974−2986.

(73) Krishna, R.; van Baten, J. M. Onsager coefficients for binary mixture diffusion in nanopores. *Chem. Eng. Sci.* **2008**, *63*, 3120−3140.

Supporting Information

Using Molecular Simulations to Unravel the Benefits of Characterizing Mixture Permeation in Microporous Membranes in terms of the Spreading Pressure

Rajamani Krishna* and Jasper M. van Baten

Van 't Hoff Institute for Molecular Sciences
University of Amsterdam
Science Park 904
1098 XH Amsterdam, The Netherlands
email: r.krishna@contact.uva.nl

Table of Contents

1 Preamble

The Supporting Information accompanying our article *Using Molecular Simulations to Unravel the Benefits of Characterizing Mixture Permeation in Microporous Membranes in terms of the Spreading Pressure* provides (a) detailed structural information on all host materials, (b) CBMC and MD simulation methodologies, (c) CBMC data on unary isotherms and isotherm fits, (d) CBMC and MD data on adsorption, diffusion, and permeation of variety of mixtures.

For ease of reading, the Supporting Information is written as a stand-alone document; as a consequence, there is some overlap of material with the main manuscript.

2 Structural details of microporous crystalline materials

The investigated host materials fall into four broad classes;

1. One-dimensional (1D) channels (MgMOF-74, BTP-COF); see Figure S1.
2. Intersecting channels (MFI); see Figure S2
3. Cages separated by narrow windows (CHA, DDR, ZIF-8); see Figure S3.
4. Cavities with large windows (FAU (all-silica), NaY, NaX); see Figure S4.

The crystallographic data are available on the zeolite atlas website of the International Zeolite Association (IZA).[1, 2] Further details on the structure, landscape, pore dimensions of a very wide variety of micro-porous materials are available in the published literature.[3-10] Table S1, and Table S2 provide some salient structural information on various zeolites and MOFs of interest.

2.1 List of Tables for Structural details of microporous crystalline materials

Table S1. Salient structural information.

Structure	Topology	Fractional pore volume, ϕ	Pore volume/ cm^3/g	Framework density/ kg/m^3
CHA	316 Å^3 cages separated by 3.77 Å × 4.23 Å size windows	0.382	0.264	1444
DDR	277.8 Å^3 cages separated by 3.65 Å × 4.37 Å size windows	0.245	0.139	1760
MFI	10-ring intersecting channels of 5.4 Å – 5.5 Å and 5.4 Å – 5.6 Å size	0.297	0.165	1796
FAU (all silica)	790 Å^3 cages separated by 7.4 Å size windows	0.439	0.328	1338
NaY	790 Å^3 cages separated by 7.4 Å size windows	0.41	0.303	1347
NaX	790 Å^3 cages separated by 7.4 Å size windows	0.40	0.280	1421
MgMOF-74	1D hexagonal-shaped channels of 11 Å	0.708	0.782	905
BTP-COF	1D hexagonal-shaped channels of 34 Å	0.752	1.79	420
ZIF-8	1168 Å^3 cages separated by 3.26 Å size windows	0.476	0.515	924

Structural details of microporous crystalline materials

Table S2. Pore volumes, surface areas, and characteristic (Delaunay) dimensions

Structure	**Pore volume** / cm^3 g^{-1}	**Surface area** / m^2 g^{-1}	**Delaunay diameter**/ Å
MFI	0.165	487.2	5.16
FAU (all silica)	0.328	1086	7.4
NaY	0.303	950	7.4
NaX	0.280	950	7.4
CHA	0.264	757.5	3.98
DDR	0.139	350	4.02
ZIF-8	0.515	1164.7	3.26
MgMOF-74	0.782	1640.0	10.66
BTP-COF	1.791		34.26

2.2 List of Figures for Structural details of microporous crystalline materials

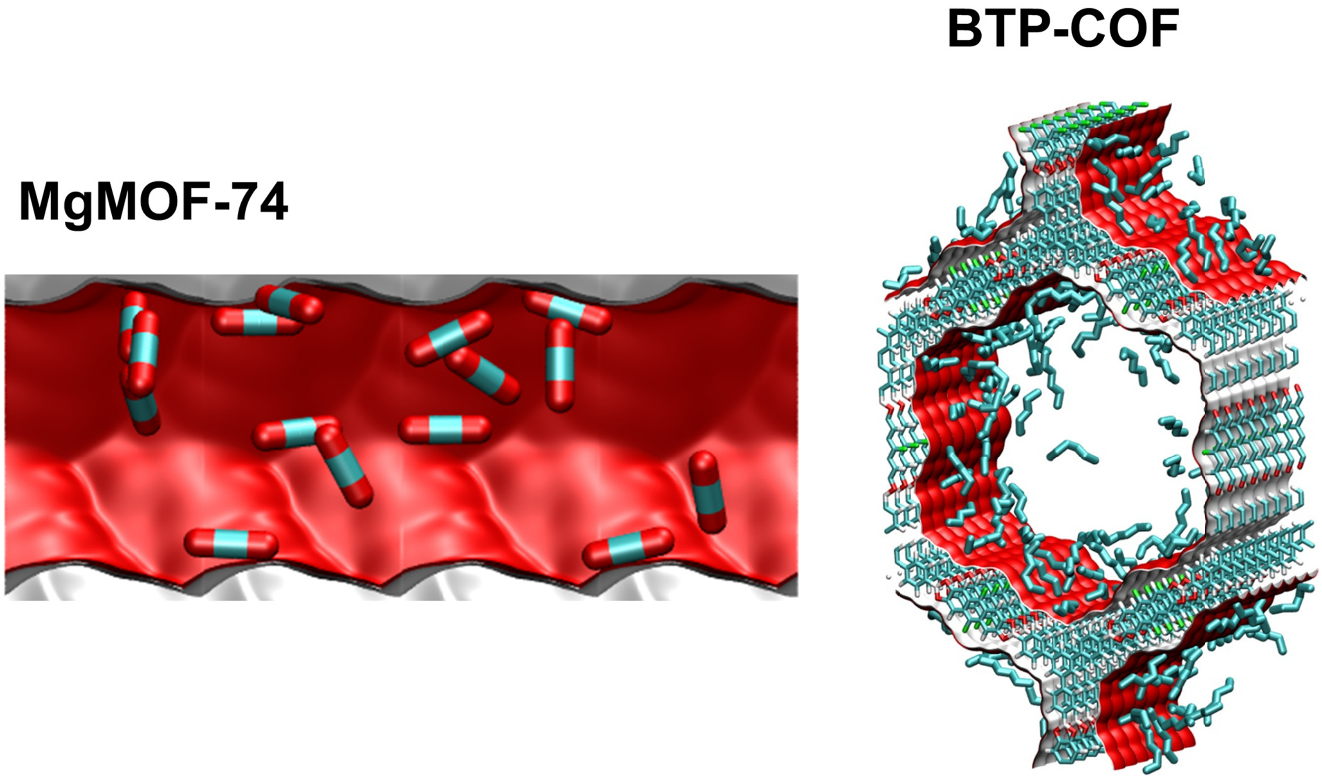

Figure S1. Examples of one-dimensional (1D) channel structures: MgMOF-74, and BTP-COF.

MFI

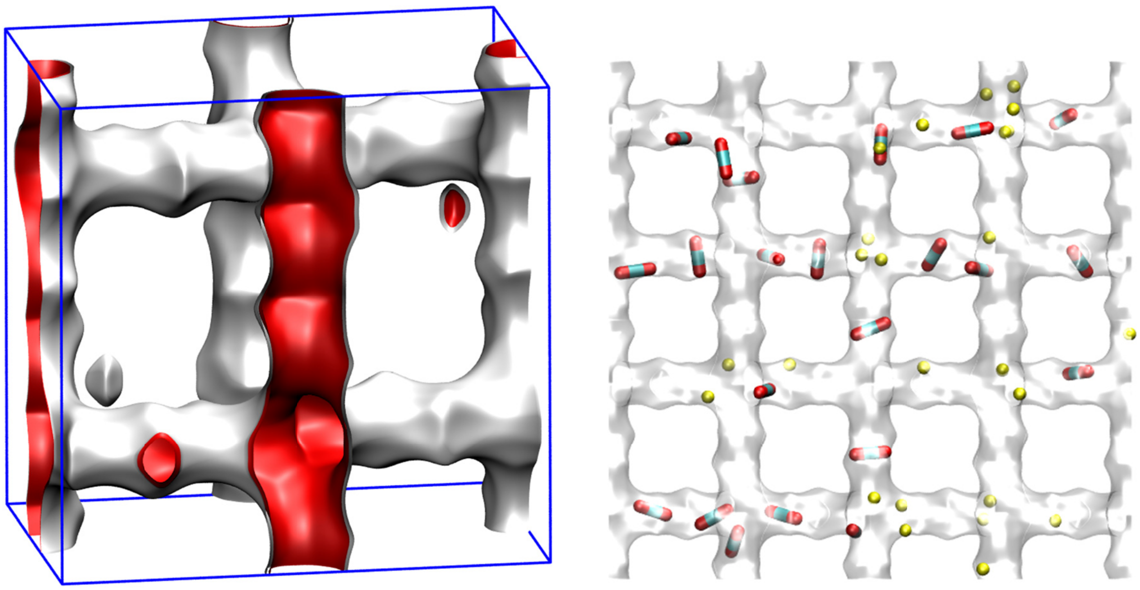

Figure S2. Structure consisting of intersecting channels: MFI.

Structural details of microporous crystalline materials

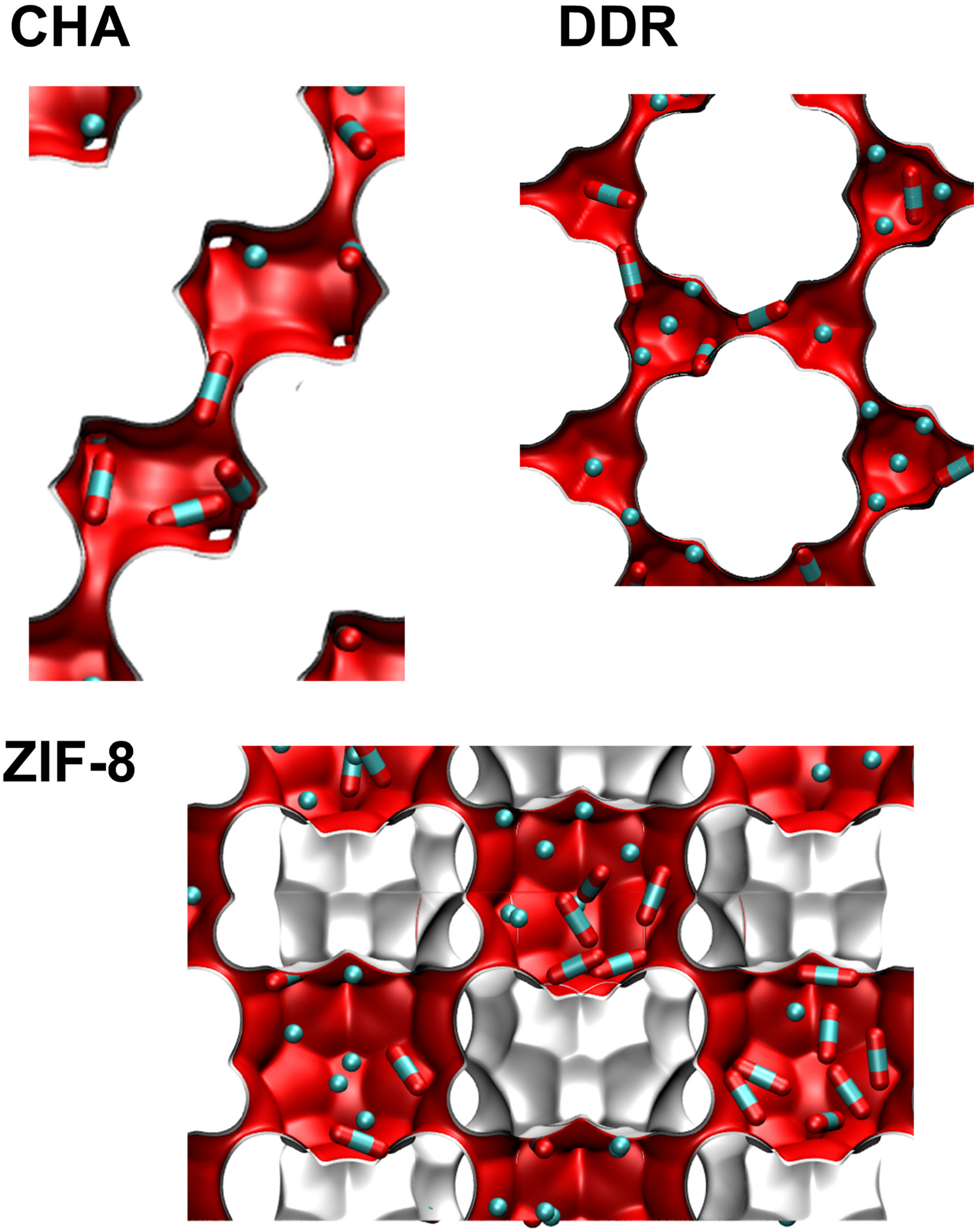

Figure S3. Structures consisting of cages separated by narrow windows: CHA, DDR, and ZIF-8.

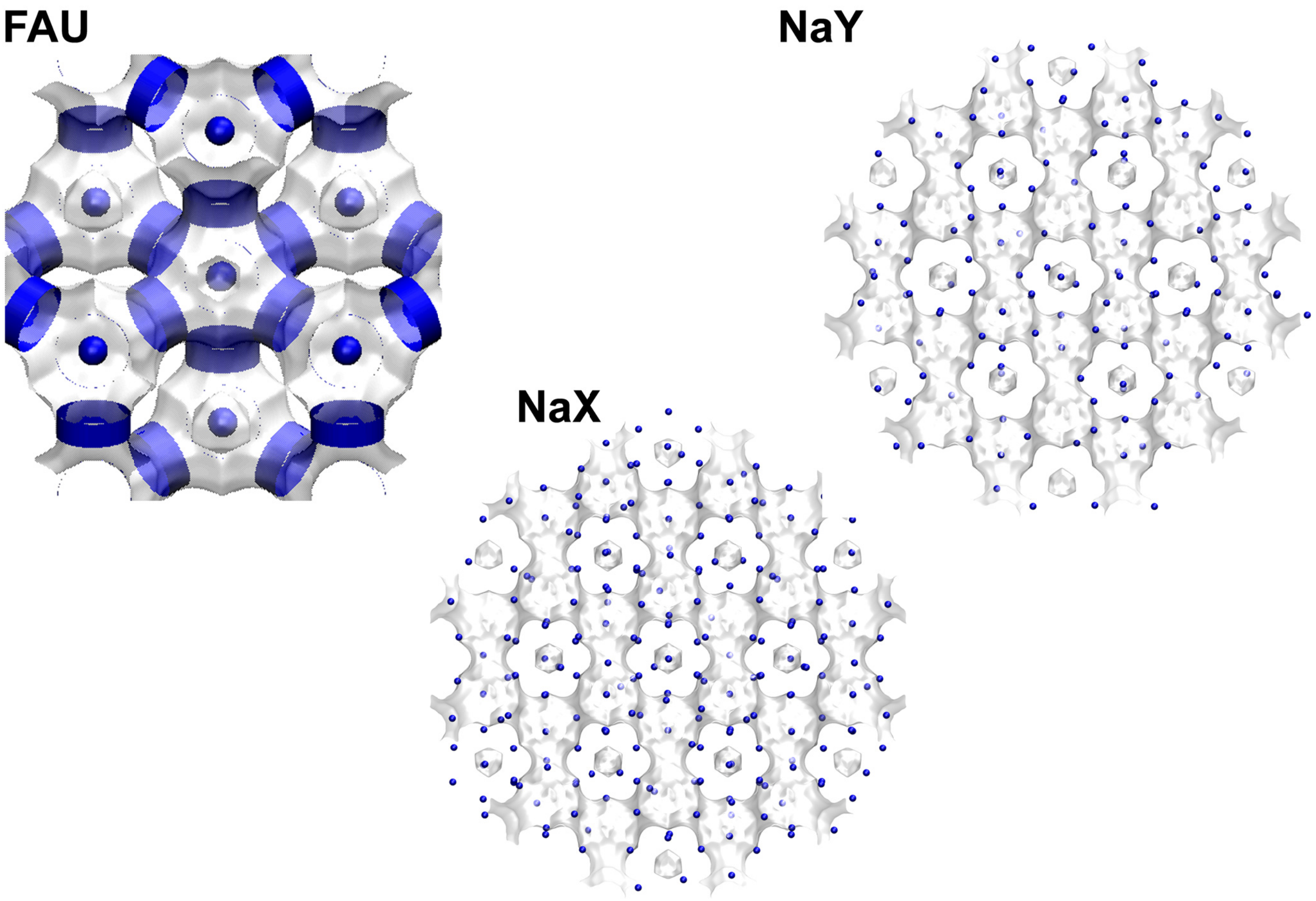

Figure S4. “Open” structures that consist of cages separated by large windows: FAU, NaY, NaX

3 Configurational-Bias Monte Carlo Simulation Methodology

The simulation methodologies and the force field information used are the same as detailed in the Supplementary Materials accompanying our earlier publications.[3, 5, 9, 11-14] A short summary is provided hereunder.

3.1 Zeolites (all silica)

CH_4 molecules are described with a united atom model, in which each molecule is treated as a single interaction center.[15] The interaction between adsorbed molecules is described with Lennard-Jones terms; see Figure S5. The Lennard-Jones parameters for CH_4-zeolite interactions are taken from Dubbeldam et al.[16]. The force field for H_2 corresponds to that given by Kumar et al.[17] In implementing this force field, quantum effects for H_2 have been ignored because the work of Kumar et al.[17] has shown that quantum effects are of negligible importance for temperatures above 200 K; all our simulations were performed at 300 K. The Lennard-Jones parameters for CO_2-zeolite and N_2-zeolite are essentially those of Makrodimitris et al.[18]; see also García-Pérez et al.[19]. For simulations with linear alkanes with two or more C atoms, the beads in the chain are connected by harmonic bonding potentials. A harmonic cosine bending potential models the bond bending between three neighboring beads, a Ryckaert-Bellemans potential controls the torsion angle. The beads in a chain separated by more than three bonds interact with each other through a Lennard-Jones potential; see schematic in Figure S5. The force fields of Dubbeldam et al.[16] was used for the variety of potentials. The Lennard-Jones potentials are shifted and cut at 12 Å.

The zeolite frameworks were considered to be rigid in all the simulation results reported in the article.

3.2 Cation-exchanged zeolites

The following two cation-exchanged structures were investigated

NaX (106 Si, 86 Al, 86 Na^+, Si/Al=1.23)

NaY (144 Si, 48 Al, 48 Na^+, Si/Al=3)

The presence of cations reduces the accessible pore volume. The location of the cations are pictured in Figure S6, and Figure S7.

The force field information for the simulations with cations are taken from García-Sanchez et al.[20] In the MC simulations, the cations were allowed to move within the framework and both Lennard-Jones and Coulombic interactions are taken into consideration.

In the CBMC simulations both Lennard-Jones and Coulombic interactions are taken into consideration; see schematic sketch in Figure S8.

3.3 MOFs and ZIFs

The ZIF-8 = Zn(methylimidazole)$_2$ structure was constructed on the basis of the structural data from Banerjee et al.[21] The original structural data files (cif file) contain solvent molecules; these were removed and the solvent-free structures were considered.

The structural information on MgMOF-74 (= Mg_2(dobdc) = Mg\(dobdc) with dobdc = (dobdc^{4-} = 1,4-dioxido-2,5-benzenedicarboxylate)) was obtained from a variety of references.[22-27]

The metal organic framework structures were considered to be rigid in the simulations. For the atoms in the host metal organic framework, the generic UFF[28] and DREIDING[29] force fields were used. The Lorentz-Berthelot mixing rules were applied for calculating σ and ε/k_B for guest-host interactions.

For CO_2 and N_2 adsorption in MOFs, the charges of the host framework need to be accounted for.

For ZIF-8, the Lennard-Jones potentials for the framework atoms of ZIF-8 were taken from the combined works of Mayo et al.,[29] Yang and Zhong,[30] and Jorgensen et al.[31] as was reported in the computational study of Zhou et al.[32] The framework charges of ZIF-8 were estimated using the group-contribution procedure based on quantum mechanical calculations described in the paper by Xu and Zhong. [33]

The simulations for MgMOF-74 were carried out with the force field information provided by Yazaydin et al.[27]

3.4 Pore volume

The pore volume is determined using a simulation of a single helium molecule at the reference temperature T [34-36]

$$V_{pore} = \frac{1}{m}\int_{0}^{V_{pore}} \exp\left(-\frac{U(\mathbf{r})}{k_B T}\right) d\mathbf{r} \tag{S1}$$

where U is the interaction energy between a single helium atom and the framework, and m is the mass of the framework. The pore volume can be readily computed from Monte Carlo sampling using Widom particle insertion.[37] Basically, the average Boltzmann factor associated with the random insertion of a probe molecule is computed. This value is averaged over all generated trial positions. In equation (S1) the integration is over the entire mass of the sample and yields the value of the accessible pore volume per unit mass of the framework; the units of V_{pore} are m^3/kg, or in more commonly used units mL/(g framework). The volume fraction, ϕ, is then given by $V_{\text{pore}}/V_{\text{total}}$ where V_{total} is the total volume of the unit cell. Usually, a reference temperature of 298.15 K is chosen in experiment for determination of the helium void volume; this value is also used in the simulations.

The force field for He-He interactions are taken from Table 1 of Talu and Myers.[38] For zeolites the He-O interaction parameters were also taken from this Table 1. We should mention here that the force field for He of Talu and Myers [38] is not the same as that in Skoulidas and Sholl;[39] in particular there are significant differences in the energy parameter ε/k_{B}. We had earlier used the Skoulidas force field to simulate diffusion of He in a variety of zeolites.[9] For determination of the pore volume fraction we have switched to the Talu and Myers force field parameters that has been tuned to represent experimental data on pore volumes in MFI.

For MOFs, the interaction between He and the atoms of the MOF structures were then determined using the Lorentz-Berthelot mixing rules. For determination of the pore volumes the Lennard-Jones parameters for interactions of the He probe atoms with cations are also considered

For determination of the accessible pore volumes of FAU, NaX, and NaY, the sodalite cages were blocked and no He probe atoms could enter these cages. Only the supercage volumes are determined for these structures.

3.5 Surface areas

The surface area of various structures were determined using the method described by Düren et al.[40].

3.6 Isosteric heats of adsorption

We determined the isosteric heats of adsorption, ΔQ_{st}, from CBMC simulations using the fluctuation formula

$$Q_{st} = RT - \frac{< U_i n_i > - < U_i >< n_i >}{\left\langle n_i^2 \right\rangle - \left\langle n_i \right\rangle^2} \tag{S2}$$

where n_{i} represents the number of molecules in the simulation box and $\left\langle \ldots \right\rangle$ denotes ensemble averaging.

3.7 Characteristic dimensions (Delaunay diameters)

In many cases, the characteristic size of the channels or windows of microporous structures are referred to in the article. These data are obtained following the method of Delaunay triangulation, described in the work by Foster et al.[41] These values represent the maximum hard-sphere diameter that can pass through the structure. The values quoted are obtained by substracting the Lennard-Jones sigma parameter of the framework atom.

3.8 CBMC code

All simulations reported in this work were carried out using an in-house BIGMAC code, originally developed by T.J.H. Vlugt. This code was modified to handle rigid molecular structures and charges. The calculation of the accessible pore volume using the Widom insertion of He probe atoms is implemented within the BIGMAC code.All CBMC simulations reported in this work were conducted at a temperature $T = 300$ K.

Configurational-Bias Monte Carlo Simulation Methodology

3.9 List of Figures for Configurational-Bias Monte Carlo Simulation Methodology

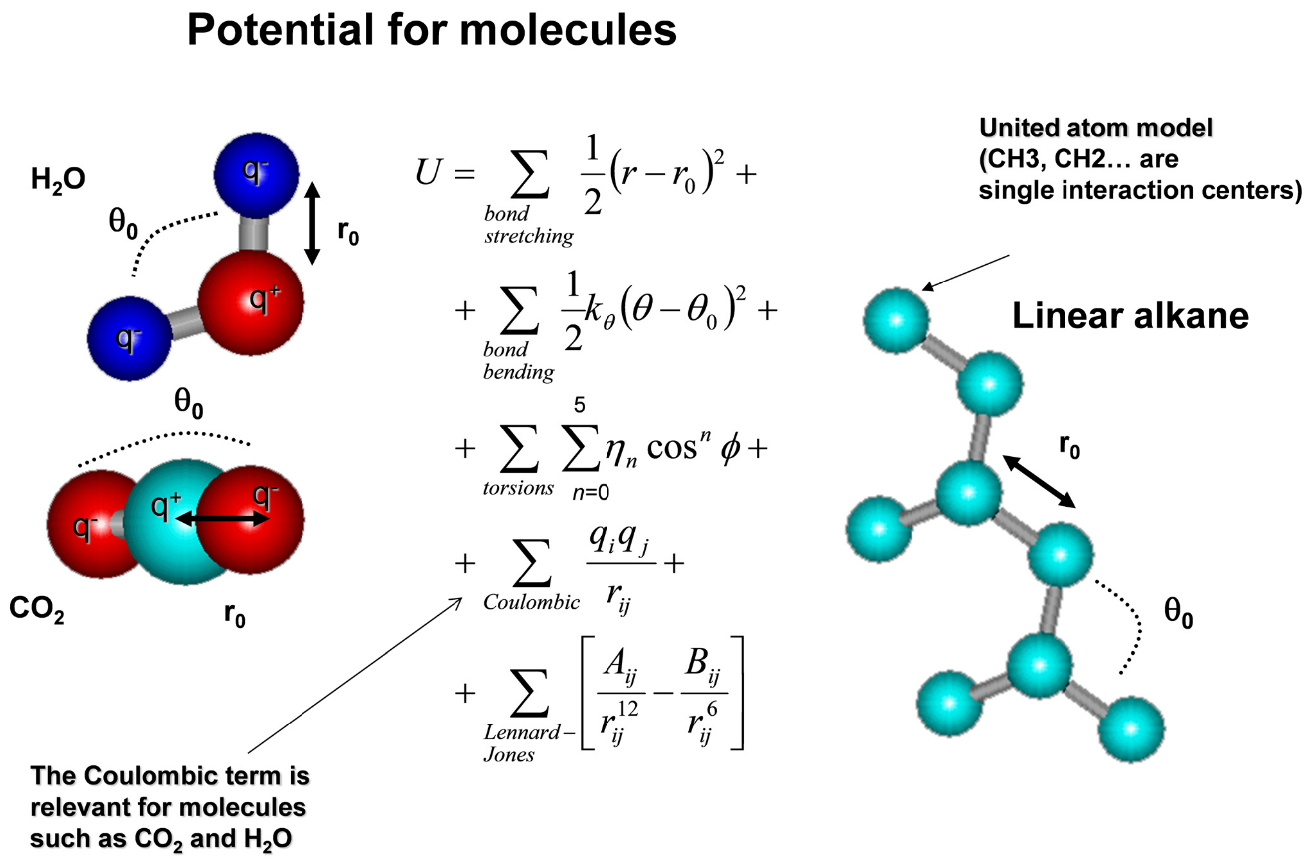

Potential for molecules

$$U = \sum_{\substack{bond\\stretching}} \frac{1}{2}(r-r_0)^2 + \sum_{\substack{bond\\bending}} \frac{1}{2}k_\theta(\theta-\theta_0)^2 + \sum_{torsions}\sum_{n=0}^{5}\eta_n \cos^n\phi + \sum_{Coulombic}\frac{q_i q_j}{r_{ij}} + \sum_{Lennard-Jones}\left[\frac{A_{ij}}{r_{ij}^{12}} - \frac{B_{ij}}{r_{ij}^{6}}\right]$$

United atom model (CH3, CH2… are single interaction centers)

The Coulombic term is relevant for molecules such as CO_2 and H_2O

Figure S5. Potential for molecules.

NaX (106 Si, 86 Al, 86 Na+, Si/Al=1.23)

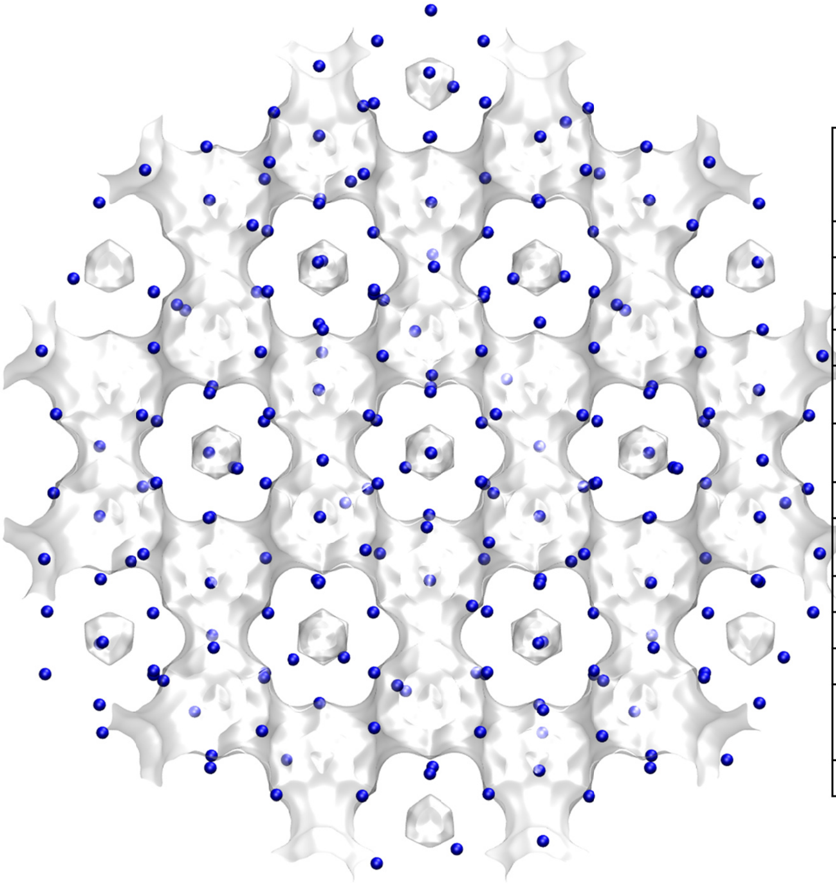

	FAU 86 Na/uc
a /Å	25.028
b /Å	25.028
c /Å	25.028
Cell volume / Å^3	15677.56
conversion factor for [molec/uc] to [mol per kg Framework]	0.0745
conversion factor for [molec/uc] to [kmol/m^3]	0.2658
ρ [kg/m3] (with cations)	1421.277
MW unit cell [g/mol(framework+cations)]	13418.42
ϕ, fractional pore volume	0.399
open space / Å^3/uc	6248.0
Pore volume / cm^3/g	0.280
Surface area /m^2/g	
DeLaunay diameter /Å	7.37

Figure S6. Location of cations for NaX zeolite (106 Si, 86 Al, 86 Na$^+$, Si/Al=1.23)

NaY (144 Si, 48 Al, 48 Na+, Si/Al=3)

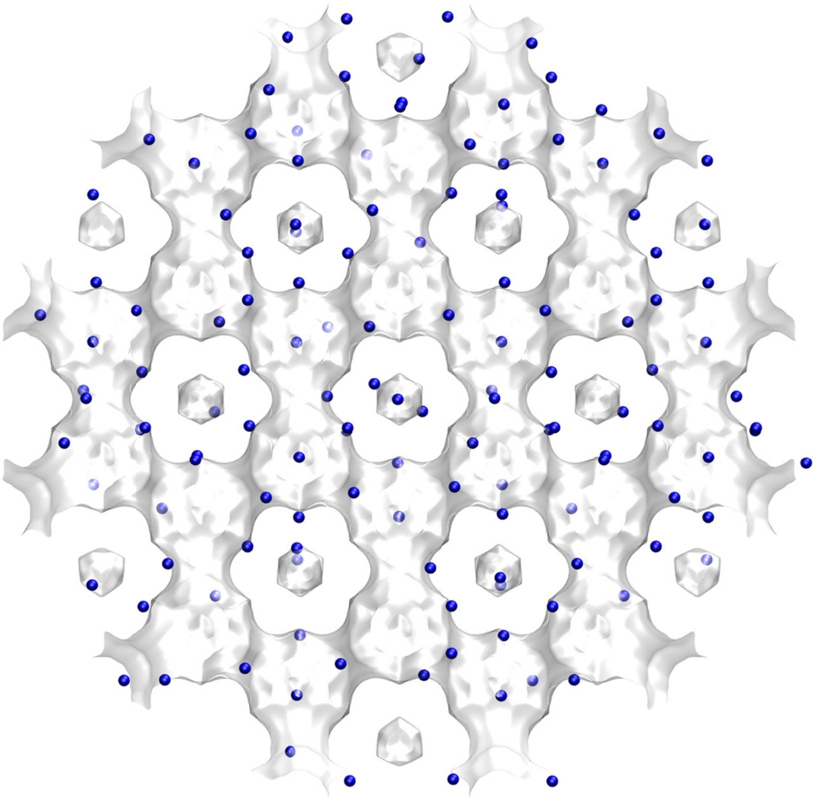

	FAU 48 Na/ucl
a /Å	25.028
b /Å	25.028
c /Å	25.028
Cell volume / Å^3	15677.56
conversion factor for [molec/uc] to [mol per kg Framework]	0.0794
conversion factor for [molec/uc] to [kmol/m^3]	0.2596
ρ [kg/m3] (with cations)	1333.19
MW unit cell [g/mol(framework+cations)]	12586.78
ϕ, fractional pore volume	0.408
open space / Å^3/uc	6396.6
Pore volume / cm^3/g	0.306
Surface area /m^2/g	
DeLaunay diameter /Å	7.37

Figure S7. Location of cations for NaY zeolite (144 Si, 48 Al, 48 Na^+, Si/Al=3)

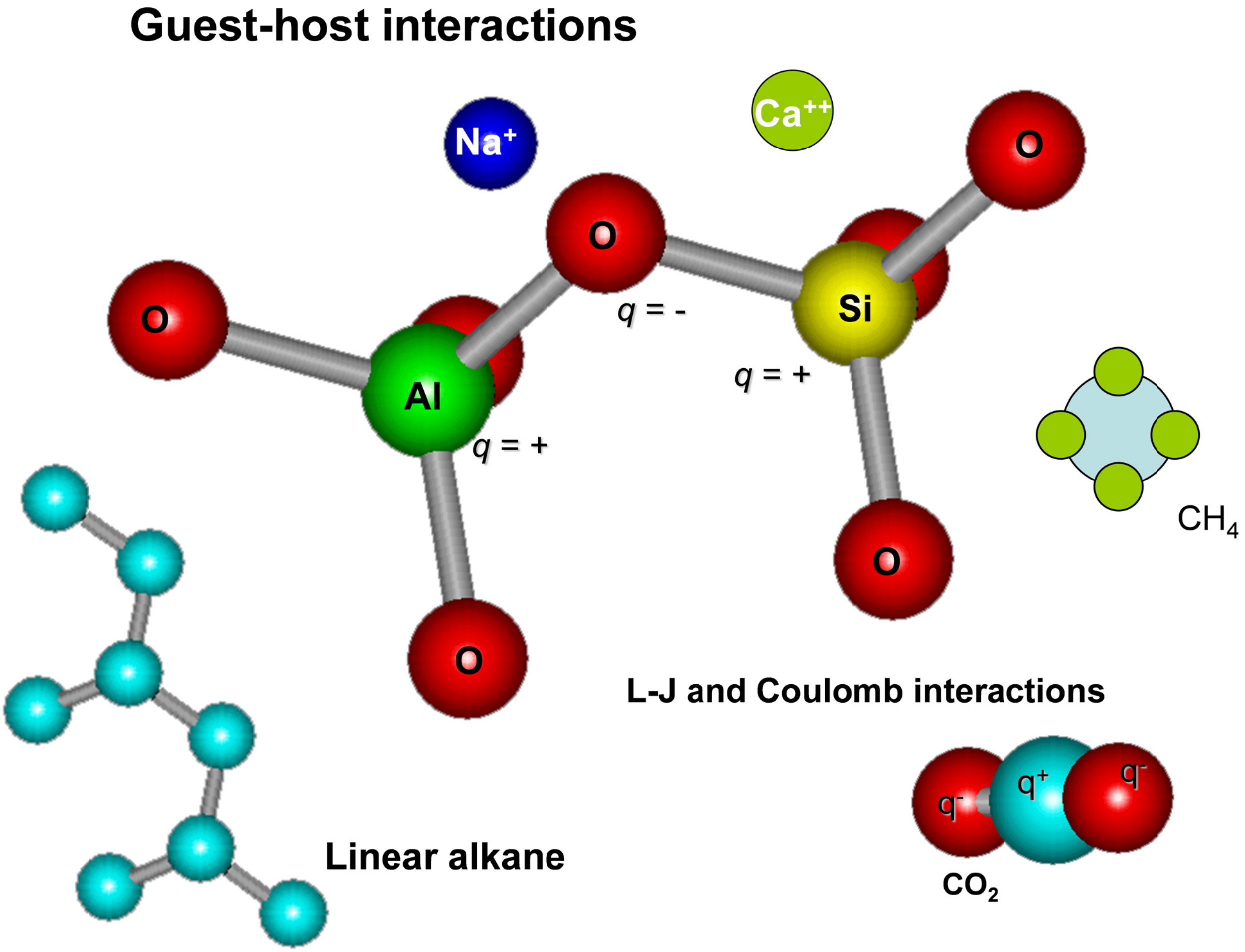

Figure S8. Guest-host interactions.

4 Molecular Dynamics (MD) Simulation Methodology

Diffusion is simulated using Newton's equations of motion until the system properties, on average, no longer change in time. The Verlet algorithm is used for time integration. A time step of 1 fs was used in all simulations. For each simulation, *initializing* CBMC moves are used to place the molecules in the domain, minimizing the energy. Next, follows an *equilibration* stage. These are essentially the same as the production cycles, only the statistics are not yet taken into account. This removes any initial large disturbances in the system that do not affect statistics on molecular displacements. After a fixed number of initialization and equilibrium steps, the MD simulation *production* cycles start. For every cycle, the statistics for determining the mean square displacements (MSDs) are updated. The MSDs are determined for time intervals ranging from 2 fs to 1 ns. In order to do this, an order-*N* algorithm, as detailed in Chapter 4 of Frenkel and Smit[37] is implemented. The Nosé-Hoover thermostat is applied to all the diffusing particles. In the MD simulations the cations were allowed to move within the framework and both Lennard-Jones and Coulombic interactions are taken into consideration; see schematic sketch in Figure S8.

For all the MD simulation results presented in this article, the DLPOLY code[42] was used along with the force field implementation as described in the previous section. DL_POLY is a molecular dynamics simulation package written by W. Smith, T.R. Forester and I.T. Todorov and has been obtained from CCLRCs Daresbury Laboratory via the website.[42]

The MD simulations were carried out for a variety of loadings within the various structures. All simulations were carried out on the LISA clusters of PCs equipped with Intel Xeon processors running at 3.4 GHz on the Linux operating system.[43] Each MD simulation, for a specified loading, was run for a time duration that is sufficiently long to obtain reliable statistics for determination of the diffusivities. In several cases the campaigns were replicated and the results averaged.

The self-diffusivities $D_{\mathrm{i,self}}$ are computed from MD simulations by analyzing the mean square displacement of each species *i* for each coordinate direction

$$D_{i,self} = \frac{1}{2n_i} \lim_{\Delta t \to \infty} \frac{1}{\Delta t} \left\langle \left(\sum_{l=1}^{n_i} \left(\mathbf{r}_{l,i}(t+\Delta t) - \mathbf{r}_{l,i}(t) \right)^2 \right) \right\rangle \tag{S3}$$

In this expression n_{i} represents the number of molecules of species *i*, and $\mathbf{r}_{\mathrm{l,i}}(t)$ is the position of molecule *l* of species *i* at any time *t*.

For three-dimensional pore networks (e.g. MFI, FAU, NaX, NaY, CHA, ZIF-8) the arithmetic average of the diffusivities in the three coordinate directions were used in further analysis and reported. For one-dimensional pore structures (MgMOF-74, BTP-COF) the diffusivities along the direction of diffusion are reported and analyzed. For DDR the reported diffusivities are the averages in *x*- and *y*-directions.

All MD simulations reported in this work were conducted at a temperature $T = 300$ K.

5 Thermodynamics of Mixture Adsorption in Micro-porous Materials

Within microporous crystalline materials, the guest molecules exist in the adsorbed phase, and the thermodynamics of mixture adsorption has an important bearing on the diffusion characteristics of guest molecules. For that reason, we provide below a brief summary of the Ideal Adsorbed Solution Theory (IAST) theory of Myers and Prausnitz.[44]

5.1 Brief outline of theory

The Gibbs adsorption equation[45] in differential form is

$$A d\pi = \sum_{i=1}^{n} q_i d\mu_i \tag{S4}$$

The quantity A is the surface area per kg of framework, with units of m^2 per kg of the framework of the crystalline material; q_i is the molar loading of component i in the adsorbed phase with units moles per kg of framework; μ_i is the molar chemical potential of component i. The spreading pressure π has the same units as surface tension, i.e. N m^{-1}.

The chemical potential of any component in the adsorbed phase, μ_i, equals that in the bulk fluid phase. If the partial fugacities in the bulk fluid phase are f_i, we have

$$d\mu_i = RTd \ln f_i \tag{S5}$$

where R is the gas constant (= 8.314 J mol^{-1} K^{-1}).

Briefly, the basic equation of Ideal Adsorbed Solution Theory (IAST) theory of Myers and Prausnitz[44] is the analogue of Raoult's law for vapor-liquid equilibrium, i.e.

$$f_i = P_i^0 x_i; \quad i = 1,2,...n \tag{S6}$$

where x_i is the mole fraction in the adsorbed phase

$$x_i = \frac{q_i}{q_1 + q_2 + ... q_n} \tag{S7}$$

and P_i^0 is the pressure for sorption of every component *i*, which yields the same spreading pressure, π for each of the pure components, as that for the mixture:

$$\frac{\pi A}{RT} = \int_0^{P_1^0} \frac{q_1^0(f)}{f} df = \int_0^{P_2^0} \frac{q_2^0(f)}{f} df = \int_0^{P_3^0} \frac{q_3^0(f)}{f} df = ... \tag{S8}$$

where $q_i^0(f)$ is the *pure* component adsorption isotherm. The units of $\Phi \equiv \frac{\pi A}{RT}$, also called the adsorption potential, [46-50] are mol kg^{-1}.

The unary isotherm may be described by say the 1-site Langmuir isotherm

$$q^0(f) = q_{sat} \frac{bf}{1+bf}; \quad \theta = \frac{bf}{1+bf} \tag{S9}$$

where we define the fractional *occupancy* of the adsorbate molecules, $\theta = q^0(f)/q_{sat}$. The superscript 0 is used to emphasize that $q^0(f)$ relates the *pure component* loading to the bulk fluid fugacity. For all of the guest/host combinations considered in this article, the unary isotherms need to be described by the dual-Langmuir-Freundlich model

$$q^0(f) = q_{A,sat} \frac{b_A f^{\nu A}}{1+b_A f^{\nu A}} + q_{B,sat} \frac{b_B f^{\nu B}}{1+b_B f^{\nu B}} \tag{S10}$$

Each of the integrals in Equation (S8) can be evaluated analytically. For the dual-site Langmuir-Freundlich isotherm, for example, the integration yields for component *i*,

$$\begin{aligned} \Phi &\equiv \frac{\pi A}{RT} = \int_{f=0}^{P_i^0} \frac{q_i^0(f)}{f} df = \frac{q_{A,sat}}{\nu_A} \ln\left(1 + b_A \left(P_i^0\right)^{\nu_A}\right) + \frac{q_{B,sat}}{\nu_B} \ln\left(1 + b_B \left(P_i^0\right)^{\nu_B}\right); \\ \Phi &\equiv \frac{\pi A}{RT} = \int_{f=0}^{P_i^0} \frac{q_i^0(f)}{f} df = \frac{q_{A,sat}}{\nu_A} \ln\left(1 + b_A \left(\frac{f_i}{x_i}\right)^{\nu_A}\right) + \frac{q_{B,sat}}{\nu_B} \ln\left(1 + b_B \left(\frac{f_i}{x_i}\right)^{\nu_B}\right) \end{aligned} \tag{S11}$$

The right hand side of equation (S11) is a function of P_i^0 . For multicomponent mixture adsorption, each of the equalities on the right hand side of Equation (S8) must be satisfied. These constraints may be solved using a suitable equation solver, to yield the set of values of P_1^0 , P_2^0 , P_3^0 ,.. P_n^0 , all of which satisfy Equation (S8). The corresponding values of the integrals using these as upper limits of integration must yield the same value of $\frac{\pi A}{RT}$ for each component; this ensures that the obtained solution is the correct one.

The adsorbed phase mole fractions x_i are then determined from

$$x_i = \frac{f_i}{P_i^0}; \quad i = 1,2,...n \tag{S12}$$

The applicability of eqs (S6) and (S12) mandates that all of the adsorption sites within the microporous material are equally accessible to each of the guest molecules, implying a homogeneous distribution of guest adsorbates within the pore landscape, with no preferential locations of any guest species. The circumstances in which this mandate is not fulfilled are highlighted in recent works.[48, 49, 51]

A key assumption of the IAST is that the enthalpies and surface areas of the adsorbed molecules do not change upon mixing. If the total mixture loading is q_t, the area covered by the adsorbed mixture is $\frac{A}{q_t}$ with units of m^2 (mol mixture)$^{-1}$. Therefore, the assumption of no surface area change due to mixture adsorption translates as $\frac{A}{q_t} = \frac{Ax_1}{q_1^0(P_1^0)} + \frac{Ax_2}{q_2^0(P_2^0)} + \cdots \frac{Ax_n}{q_n^0(P_n^0)}$; the total mixture loading is q_t is calculated from

$$q_t = q_1 + q_2 ... + q_n = \frac{1}{\frac{x_1}{q_1^0(P_1^0)} + \frac{x_2}{q_2^0(P_2^0)} + ... + \frac{x_n}{q_n^0(P_n^0)}} \tag{S13}$$

in which $q_1^0(P_1^0)$, $q_2^0(P_2^0)$,... $q_n^0(P_n^0)$ are determined from the unary isotherm fits, using the sorption pressures for each component P_1^0, P_2^0, P_3^0,.. P_n^0 that are available from the solutions to equations Equations (S8), and (S11).

The occurrence of molecular clustering and hydrogen bonding should be expected to applicability of eq (S13) because the surface area occupied by a molecular cluster is different from that of each of the un-clustered guest molecules in the adsorbed phase.

The entire set of eqs (S6) to (S13) need to be solved numerically to obtain the loadings, q_i of the individual components in the mixture.

For the interpretation and analysis of the MD simulations for binary mixture diffusion in microporous host materials, the IAST calculation procedure has to be performed differently because in the MD simulations, the molar loadings q_1, and q_2 in the mixture are specified, and the partial fugacities in the bulk fluid mixture are not known *a priori*. Also in this case, the equalities in equation (S11) must be satisfied in conjunction with equation (S13). The entire set of equations (S6) to (S13) need to be solved numerically to obtain the partial fugacities, f_i of the individual components in the mixture, that yield the same loadings as chosen in the MD simulations. In all of the calculations presented in this article, the set of equations were solved using an Excel macro that was developed for this specific purpose.

5.2 Selectivity for binary mixture adsorption

For binary mixtures consisting of components 1, and 2, the adsorption selectivity, S_{ads}, is defined by

$$S_{ads} = \frac{q_1/q_2}{f_1/f_2} = \frac{q_1/q_2}{y_1/y_2} \tag{S14}$$

where q_1 and q_2 are the molar loadings of the components 1, and 2 in the adsorbed phase in equilibrium with a bulk gas phase mixture with mole fractions $y_1 = \frac{f_1}{f_1 + f_2}; y_2 = \frac{f_2}{f_1 + f_2}$. In view of eqs (S12), and (S13), we may re-write eq (S14) as the ratio of the sorption pressures

$$S_{ads} = \frac{q_1/q_2}{f_1/f_2} = \frac{x_1/f_1}{x_2/f_2} = \frac{P_2^0}{P_1^0} \tag{S15}$$

Applying the restriction specified by eq (S8), it follows that S_{ads} is uniquely determined by the adsorption potential $\Phi \equiv \frac{\pi A}{RT}$.

5.3 IAST model: 1-site Langmuir isotherms

The IAST procedure will be applied for binary mixture adsorption in which the unary isotherms are described by the 1-site Langmuir model in which the saturation capacities of components 1 and 2 are identical to each other, i.e. $q_{1,sat} = q_{2,sat} = q_{sat}$:

$$q_i^0\left(f\right) = q_{sat}\frac{b_i f}{1+b_i f} \tag{S16}$$

where

For unary adsorption, the adsorption potential for a 1-site Langmuir isotherm can be calculated analytically

$$\Phi \equiv \frac{\pi A}{RT} = q_{sat}\ln\left(1+bP^0\right) \tag{S17}$$

The objective is to determine the molar loadings, q_1, and q_2, in the adsorbed phase.

Performing the integration of eq (S8) results in an expression relating the sorption pressures P_i^0 of the two species

$$\begin{aligned} &\Phi \equiv \frac{\pi A}{RT} = q_{sat}\ln\left(1+b_1P_1^0\right) = q_{sat}\ln\left(1+b_2P_2^0\right) \\ &b_1P_1^0 = b_2P_2^0 = \exp\left(\frac{\pi A}{q_{sat}RT}\right)-1 \end{aligned} \tag{S18}$$

The adsorbed phase mole fractions of component 1, and component 2 are given by equation (S12)

$$x_1 = \frac{f_1}{P_1^0};\quad x_2 = 1-x_1 = \frac{f_2}{P_2^0} \tag{S19}$$

Combining equations (S18), and (S19):

$$\exp\left(\frac{\pi A}{q_{sat}RT}\right)-1 = b_1\frac{f_1}{x_1} = b_2\frac{f_2}{1-x_1} \tag{S20}$$

The adsorbed phase mole fractions can be determined

$$\frac{x_1}{x_2} = \frac{q_1}{q_2} = \frac{b_1f_1}{b_2f_2};\quad x_1 = \frac{q_1}{q_t} = \frac{b_1f_1}{b_1f_1+b_2f_2};\quad x_2 = \frac{q_2}{q_t} = \frac{b_2f_2}{b_1f_1+b_2f_2} \tag{S21}$$

Once x_1, and $x_2 = 1 - x_1$ are determined, the sorption pressures can be calculated:

$$P_1^0 = \frac{f_1}{x_1}; \quad P_2^0 = \frac{f_2}{x_2} = \frac{f_2}{1-x_1} \tag{S22}$$

From equations (S18), and (S22) we get

$$\begin{aligned} b_i P_1^0 &= \frac{b_1 f_1}{x_1} = b_2 P_2^0 = \frac{b_2 f_2}{x_2} = b_1 f_1 + b_2 f_2 \\ 1 + b_i P_1^0 &= 1 + b_2 P_2^0 = 1 + b_1 f_1 + b_2 f_2 \end{aligned} \tag{S23}$$

Combining eqs (S18), and (S23) we obtain the following explicit expression for the adsorption potential

$$\Phi = q_{sat} \ln\left(1 + b_1 f_1 + b_2 f_2\right) \tag{S24}$$

The total amount adsorbed, $q_t = q_1 + q_2$ can be calculated from Equation (S13)

$$q_t = q_1 + q_2 = q_{sat} \frac{b_1 P_1^0}{1 + b_1 P_1^0} = q_{sat} \frac{b_2 P_2^0}{1 + b_2 P_2^0} = q_{sat} \frac{b_1 f_1 + b_2 f_2}{1 + b_1 f_1 + b_2 f_2} \tag{S25}$$

Combining equations (S21), and (S25) we obtain the following explicit expressions for the component loadings, and fractional occupancies

$$\theta_1 = \frac{q_1}{q_{sat}} = \frac{b_1 f_1}{1 + b_1 f_1 + b_2 f_2}; \quad \theta_2 = \frac{q_2}{q_{sat}} = \frac{b_2 f_2}{1 + b_1 f_1 + b_2 f_2} \tag{S26}$$

Equation (S26) is commonly referred to as the mixed-gas Langmuir model.

From equations (S18), (S25), and (S26) we derive the following expression for the total occupancy of the mixture

$$\theta = \theta_1 + \theta_2 = \frac{q_t}{q_{sat}} = 1 - \exp\left(-\frac{\Phi}{q_{sat}}\right) = \frac{b_1 f_1 + b_2 f_2}{1 + b_1 f_1 + b_2 f_2} \tag{S27}$$

For *unary* adsorption of component *i*, say, $f_i = P_i^0$, the occupancy of component 1 is

$$\theta_i = 1-\exp\left(-\frac{\Phi}{q_{i,sat}}\right) = \frac{b_i f_i}{1+b_i f_i}; \quad \text{unary adsorption of species i} \tag{S28}$$

From equations (S27), and (S28) we may also conclude the *occupancy* may be considered to be the appropriate *proxy* for the spreading pressure. The conclusion that we draw from the foregoing analysis is that the equalities of spreading pressures for unary adsorption of component 1, unary adsorption of component 2, and binary 1-2 mixture adsorption also implies the corresponding equalities of the corresponding *occupancies* for unary adsorption of component 1, unary adsorption of component 2, and binary 1-2 mixture adsorption.

5.4 Generalized expression for fractional occupancy

From knowledge of the adsorption potential, $\Phi \equiv \frac{\pi A}{RT}$, the fractional occupancy for binary mixture adsorption is then calculated using

$$\theta = 1-\exp\left(-\frac{\pi A}{q_{sat,mix} RT}\right) = 1-\exp\left(-\frac{\Phi}{q_{sat,mix}}\right) \tag{S29}$$

For a binary mixture, the saturation capacity $q_{sat,mix}$ is calculated from the saturation capacities of the constituent guests

$$q_{sat,mix} = \frac{1}{\frac{x_1}{q_{1,sat}} + \frac{x_2}{q_{2,sat}}}; \quad q_{1,sat} = q_{1,A,sat} + q_{1,B,sat}; \quad q_{2,sat} = q_{2,A,sat} + q_{2,B,sat} \tag{S30}$$

where

$$x_1 = \frac{q_1}{q_1+q_2}; \quad x_2 = \frac{q_2}{q_1+q_2} \tag{S31}$$

are the mole fractions in the adsorbed mixture. For equimolar mixtures, $x_1 = x_2 = 0.5$, equation (S31) simplifies to yield $q_{sat,mix} = \frac{2}{\frac{1}{q_{1,sat}} + \frac{1}{q_{2,sat}}}$.

The fundamental justification of Equation (S30) is provided by applying equation (S13) to pore saturation conditions.

Equations (S29) is the appropriate generalization of Equation (S27), derived in the following section for the mixed-gas Langmuir model. It is also to be noted that equation (15) of our earlier publication[52] has a typographical error in the calculation of $q_{sat,mix}$; the correct form is given by equation (S30).

6 The Real Adsorbed Solution Theory (RAST)

To account for non-ideality effects in mixture adsorption, we introduce activity coefficients γ_i into Equation (S6) [44]

$$f_i = P_i^0 x_i \gamma_i \tag{S32}$$

With the introduction of activity coefficients, the expression for the adsorption selectivity for binary mixtures is

$$S_{ads} = \frac{q_2/q_1}{y_2/y_1} = \frac{q_2/y_2}{q_1/y_1} = \frac{x_2/f_2}{x_1/f_1} = \frac{P_1^0 \gamma_1}{P_2^0 \gamma_2} \tag{S33}$$

The implementation of the activity coefficients is termed as the Real Adsorbed Solution Theory (RAST). Following the approaches of Myers, Talu, and Sieperstein[46, 47, 53] we model the excess Gibbs free energy for binary mixture adsorption as follows

$$\frac{G^{excess}}{RT} = x_1 \ln(\gamma_1) + x_2 \ln(\gamma_2) \tag{S34}$$

6.1 Margules model for activity coefficients

The Margules model for activity coefficients is

$$\begin{aligned} \ln(\gamma_1) &= x_2^2 \left(A_{12} + 2\left(A_{21} - A_{12} \right) x_1 \right) \left(1 - \exp\left(-C \frac{\pi A}{RT} \right) \right) \\ \ln(\gamma_2) &= x_1^2 \left(A_{21} + 2\left(A_{12} - A_{21} \right) x_2 \right) \left(1 - \exp\left(-C \frac{\pi A}{RT} \right) \right) \end{aligned} \tag{S35}$$

In eq (S35) C is a constant with the units kg mol^{-1}. The introduction of $\left(1 - \exp\left(-C \frac{\pi A}{RT} \right) \right)$ imparts the correct limiting behaviors $\gamma_i \to 1; \quad \frac{\pi A}{RT} \to 0$ for the activity coefficients in the Henry regime, $f_t \to 0; \quad \frac{\pi A}{RT} \to 0$. As pore saturation conditions are approached, this correction factor tends to unity

$\left(1-\exp\left(-C\frac{\pi A}{RT}\right)\right)\rightarrow 1$. The choice of $A_{12} = A_{21} = 0$ in eq (S35), yields unity values for the activity coefficients.

The excess reciprocal loading for the mixture can be defined as

$$\left(\frac{1}{q_t}\right)^{excess} = \frac{1}{q_t} - \left(\frac{x_1}{q_1^0(P_1^0)} + \frac{x_2}{q_2^0(P_2^0)}\right) \tag{S36}$$

The excess reciprocal loading for the mixture can be related to the partial derivative of the Gibbs free energy with respect to the adsorption potential at constant composition

$$\left(\frac{1}{q_t}\right)^{excess} = \left.\frac{\partial\left(\frac{G^{excess}}{RT}\right)}{\partial\left(\frac{\pi A}{RT}\right)}\right|_{T,x} = x_1x_2\left[A_{12}x_2 + A_{21}x_1\right]C\exp\left(-C\frac{\pi A}{RT}\right) \tag{S37}$$

For calculation of the total mixture loading $q_t = q_1 + q_2$ we need to replace eq (S13) by

$$\frac{1}{q_t} = \frac{x_1}{q_1^0(P_1^0)} + \frac{x_2}{q_2^0(P_2^0)} + x_1x_2\left[A_{12}x_2 + A_{21}x_1\right]C\exp\left(-C\frac{\pi A}{RT}\right) \tag{S38}$$

The parameters A_{12}, A_{21}, C can be fitted to match the CBMC data on mixture adsorption.

6.2 Wilson model for activity coefficients

The Wilson model for activity coefficients are given for binary mixtures by

$$\begin{aligned}
\ln(\gamma_1) &= \left(1-\ln(x_1\Lambda_{11}+x_2\Lambda_{12}) - \frac{x_1\Lambda_{11}}{x_1\Lambda_{11}+x_2\Lambda_{12}} - \frac{x_2\Lambda_{21}}{x_2+x_1\Lambda_{21}}\right)\left(1-\exp\left(-C\frac{\pi A}{RT}\right)\right) \\
\ln(\gamma_2) &= \left(1-\ln(x_1\Lambda_{21}+x_2\Lambda_{22}) - \frac{x_1\Lambda_{12}}{x_1\Lambda_{11}+x_2\Lambda_{12}} - \frac{x_2\Lambda_{22}}{x_1\Lambda_{21}+x_2\Lambda_{22}}\right)\left(1-\exp\left(-C\frac{\pi A}{RT}\right)\right)
\end{aligned} \tag{S39}$$

In Equation (S39), $\Lambda_{11} \equiv 1; \quad \Lambda_{22} \equiv 1$, and C is a constant with the units kg mol^{-1}. The introduction of $\left(1-\exp\left(-C\frac{\pi A}{RT}\right)\right)$ imparts the correct limiting behaviors $\gamma_i \rightarrow 1; \quad \frac{\pi A}{RT}\rightarrow 0$ for the activity coefficients in the Henry regime, $f_t \to 0; \quad \frac{\pi A}{RT} \to 0$. As pore saturation conditions are approached, this correction factor tends to unity $\left(1-\exp\left(-C\frac{\pi A}{RT}\right)\right) \to 1$. The choice of $\Lambda_{12} = \Lambda_{21} = 1$ in Equation (S39), yields unity values for the activity coefficients.

The excess reciprocal loading for the mixture can be defined as

$$\left(\frac{1}{q_t}\right)^{excess} = \frac{1}{q_t} - \left(\frac{x_1}{q_1^0(P_1^0)} + \frac{x_2}{q_2^0(P_2^0)}\right) \tag{S40}$$

The excess reciprocal loading for the mixture can be related to the partial derivative of the Gibbs free energy with respect to the adsorption potential at constant composition

$$\left(\frac{1}{q_t}\right)^{excess} = \left.\frac{\partial\left(\frac{G^{excess}}{RT}\right)}{\partial\left(\frac{\pi A}{RT}\right)}\right|_{T,x} = \left[-x_1 \ln(x_1 + x_2\Lambda_{12}) - x_2 \ln(x_2 + x_1\Lambda_{21})\right] C \exp\left(-C\frac{\pi A}{RT}\right) \tag{S41}$$

For calculation of the total mixture loading we need to replace Equation (S13) by

$$q_t \equiv q_1 + q_2 = \frac{1}{\frac{x_1}{q_1^0(P_1^0)} + \frac{x_2}{q_2^0(P_2^0)} + \left[-x_1 \ln(x_1 + x_2\Lambda_{12}) - x_2 \ln(x_2 + x_1\Lambda_{21})\right] C \exp\left(-C\frac{\pi A}{RT}\right)} \tag{S42}$$

The parameters Λ_{12}, Λ_{21}, and *C* can be fitted to match the CBMC data on mixture adsorption.

7 Unary Adsorption and Diffusion in Microporous Materials

The self-diffusivities $D_{i,self}$ are computed from MD simulations by analyzing the mean square displacement of each species i for each coordinate direction

$$D_{i,self} = \frac{1}{2n_i} \lim_{\Delta t \to \infty} \frac{1}{\Delta t} \left\langle \left(\sum_{l=1}^{n_i} \left(\mathbf{r}_{l,i}(t+\Delta t) - \mathbf{r}_{l,i}(t) \right)^2 \right) \right\rangle \tag{S43}$$

In this expression n_i represents the number of molecules of species i, and $\mathbf{r}_{l,i}(t)$ is the position of molecule l of species i at any time t.

MD simulations of the unary self-diffusivities, $D_{i,self}$, in a variety of guest molecules in a variety of host structures at 300 K were performed; these are reported in our earlier publications.[3, 5, 6, 9, 10, 13, 14, 54-60] The data are presented in the following set of Figures:

Figure S9: MFI zeolite

Figure S10: all-silica FAU zeolite

Figure S11: NaY zeolite

Figure S12: NaX zeolite

Figure S13: all-silica CHA zeolite

Figure S14: DDR

Figure S15: ZIF-8

Figure S16: MgMOF-74

Figure S17: BTP-COF

Broadly speaking, for all guest/host combinations, the self-diffusivities, $D_{i,self}$, are strongly dependent on the molar loadings. The diffusivities tend to decrease as the saturation loadings are approached. The loading dependence is often strongly influenced by the adsorption isotherms, and the spreading pressures. Configurational-Bias Monte Carlo (CBMC) simulations of the unary adsorption isotherms were also determined, and are plotted in the afore-listed Figures. These CBMC simulated isotherms were fitted with the dual-site Langmuir-Freundlich model, equation (S10); the fit parameters for each guest molecule (with sites A, and B) are tabulated for each host material as follows:

Table S3: MFI zeolite

Table S4: FAU all-silica zeolite

Table S5: NaY zeolite

Table S6: NaX zeolite

Table S7: CHA all-silica zeolite

Table S8: DDR all-silica zeolite

Table S9: DDR all-silica zeolite

Table S10: MgMOF-74

Table S11: BTP-COF

The adsorption potential, and fractional occupancy, can be determined from

$$\Phi \equiv \frac{\pi A}{RT} = \frac{q_{A,sat}}{\nu_A} \ln\left(1 + b_A \left(f_i\right)^{\nu_A}\right) + \frac{q_{B,sat}}{\nu_B} \ln\left(1 + b_B \left(f_i\right)^{\nu_B}\right); \quad q_{i,sat} = q_{A,sat} + q_{B,sat}$$

$$\theta_i = 1 - \exp\left(-\frac{\pi A}{q_{i,sat} RT}\right); \quad \text{unary adsorption of species i} \tag{S44}$$

7.1 List of Tables for Unary Adsorption and Diffusion in Microporous Materials

Table S3. Dual-site Langmuir-Freundlich parameters for guest molecules in MFI at 300 K. To convert from molecules uc^{-1} to mol kg^{-1}, multiply by 0.173367.

	Site A			Site B		
	$\Theta_{A,sat}$ molecules uc^{-1}	b_A $\mathrm{Pa}^{-\nu A}$	ν_A dimensionless	$\Theta_{B,sat}$ molecules uc^{-1}	b_B $\mathrm{Pa}^{-\nu B}$	ν_B dimensionless
Ar	19	2.61E-07	1	15	6.75E-08	0.8
H2	30	3.57E-08	1	42	1.39E-09	1
N2	16	6.37E-07	1	16	3.82E-07	0.7
CO2	19	6.12E-06	1	11	1.73E-08	1
CH4	7	5.00E-09	1	16	3.10E-06	1
C2H6	3.3	4.08E-07	1	13	7.74E-05	1
C3H8	1.4	3.35E-04	0.67	10.7	6.34E-04	1.06

Table S4. Dual-site Langmuir-Freundlich parameters for guest molecules in FAU (all-silica) at 300 K. To convert from molecules uc^{-1} to mol kg^{-1}, multiply by 0.086683044.

	Site A			Site B		
	$\Theta_{A,sat}$ molecules uc^{-1}	b_A $\mathrm{Pa}^{-\nu A}$	ν_A dimensionless	$\Theta_{B,sat}$ molecules uc^{-1}	b_B $\mathrm{Pa}^{-\nu B}$	ν_B dimensionless
H2	85	2.75E-08	1	67	1.03E-08	1
N2	60	1.53E-09	1	75	1.32E-07	1
CO2	32	2.55E-13	2.2	70	6.86E-07	1
CH4	56	2.78E-08	0.8	60	2.90E-07	1

Table S5. Dual-site Langmuir-Freundlich parameters for guest molecules in NaY zeolite at 300 K. Per unit cell of NaY zeolite we have 144 Si, 48 Al, 48 Na+, with Si/Al=3.

	Site A			Site B		
	$q_{A,sat}$ mol kg^{-1}	b_A $\mathrm{Pa}^{-\nu A}$	ν_A dimensionless	$q_{B,sat}$ mol kg^{-1}	b_B $\mathrm{Pa}^{-\nu B}$	ν_B dimensionless
CO2	1.8	2.002E-05	0.7	5.9	4.158E-05	1
CH4	3.4	6.529E-09	1	5.9	1.134E-06	1
H2	10.5	8.382E-09	1	2.2	3.149E-08	1

Table S6. Dual-site Langmuir-Freundlich parameters for guest molecules in NaX zeolite at 300 K. Per unit cell of NaX zeolite we have 106 Si, 86 Al, 86 Na^+ with Si/Al=1.23.

	Site A			Site B		
	$q_{A,sat}$ mol kg^{-1}	b_A $Pa^{-\nu A}$	ν_A dimensionless	$q_{B,sat}$ mol kg^{-1}	b_B $Pa^{-\nu B}$	ν_B dimensionless
CO2	1.7	1.390E-05	1	4.2	4.782E-04	1
CH4	2.3	1.240E-08	1	5.5	2.170E-06	1
H2	10.5	8.382E-09	1	2.2	3.149E-08	1
N2	18.4	3.644E-10	1	4.5	1.080E-07	1

Fitted Margules non-ideality parameters for binary mixture adsorption in NaX at 300 K.

	C / kg mol^{-1}	A_{12}	A_{21}
CO_2/CH_4 in NaX	1.021	-0.632	-0.693

Table S7. Dual-site Langmuir-Freundlich parameters for guest molecules in CHA (all-silica) at 300 K. To convert from molecules uc^{-1} to mol kg^{-1}, multiply by 0.231154783.

	Site A			Site B		
	$\Theta_{A,sat}$ molecules uc^{-1}	b_A $\mathrm{Pa}^{-\nu A}$	ν_A dimensionless	$\Theta_{B,sat}$ molecules uc^{-1}	b_B $\mathrm{Pa}^{-\nu B}$	ν_B dimensionless
Ar	26	1.22E-07	1	14	4.62E-09	1
H2	63	2.58E-08	0.73	68	1.57E-08	1
N2	28	8.71E-08	0.6	32	4.87E-07	0.88
CO2	28	1.71E-06	1.1	12	8.74E-06	0.7
CH4	12	1.36E-06	1	24	4.59E-07	0.8

Table S8. Dual-site Langmuir-Freundlich parameters for guest molecules in DDR (all-silica) at 300 K.

	Site A			Site B		
	$q_{A,sat}$ mol kg^{-1}	b_A $\mathrm{Pa}^{-\nu A}$	ν_A dimensionless	$q_{B,sat}$ mol kg^{-1}	b_B $\mathrm{Pa}^{-\nu B}$	ν_B dimensionless
CO2	1.5	2.318E-06	0.74	3	5.890E-06	1
CH4	1.6	3.461E-06	1	2.4	3.405E-06	0.65
N2	1.2	1.024E-06	1	1.6	5.887E-08	1
H2	5	5.028E-08	1	12	2.442E-09	1

Fitted Margules non-ideality parameters for binary CO_2/CH_4 mixture adsorption in DDR at 300 K.

	C / kg mol^{-1}	A_{12}	A_{21}
CO_2/CH_4 in DDR	0.01	-12.62	-4.71

Table S9. Dual-site Langmuir-Freundlich parameters for guest molecules in ZIF-8 at 300 K.

	Site A			Site B		
	$q_{A,sat}$ mol kg^{-1}	b_A $\text{Pa}^{-\nu A}$	ν_A dimensionless	$q_{B,sat}$ mol kg^{-1}	b_B $\text{Pa}^{-\nu B}$	ν_B dimensionless
CO2	1.4	2.852E-15	2.7	9.8	1.433E-06	1
CH4	9.5	4.377E-07	1	3.7	6.702E-09	1
H2	19	2.372E-09	0.87	20	1.608E-08	1

Table S10. Dual-site Langmuir-Freundlich parameters for guest molecules in MgMOF-74 at 300 K. To convert from molecules uc^{-1} to mol kg^{-1}, multiply by 0.457959224.

	Site A			Site B		
	$\Theta_{A,sat}$ molecules uc^{-1}	b_A $\mathrm{Pa}^{-\nu A}$	ν_A dimensionless	$\Theta_{B,sat}$ molecules uc^{-1}	b_B $\mathrm{Pa}^{-\nu B}$	ν_B dimensionless
H2	31	7.73E-09	1	31	3.05E-08	1
CO2	28	2.05E-05	1	12	3.03E-07	1
N2	25	2.93E-07	1	20	6.06E-09	1
CH4	32	6.24E-07	1	8	2.71E-17	2

Table S11. Dual-site Langmuir-Freundlich parameters for guest molecules in BTP-COF at 300 K. To convert from molecules uc^{-1} to mol kg^{-1}, multiply by 0.34029.

	Site A			Site B		
	$\Theta_{A,sat}$ molecules uc^{-1}	b_A $Pa^{-\nu A}$	ν_A dimensionless	$\Theta_{B,sat}$ molecules uc^{-1}	b_B $Pa^{-\nu B}$	ν_B dimensionless
CO2	73	2.965E-07	1	73	2.965E-07	1
CH4	63	7.361E-08	1	63	7.361E-08	1
H2	100	1.234E-08	1	100	1.234E-08	1
Ar	79	3.469E-08	1	79	3.469E-08	1
C2H6	23	2.943E-21	3.3	69	5.497E-07	1

7.2 List of Figures for Unary Adsorption and Diffusion in Microporous Materials

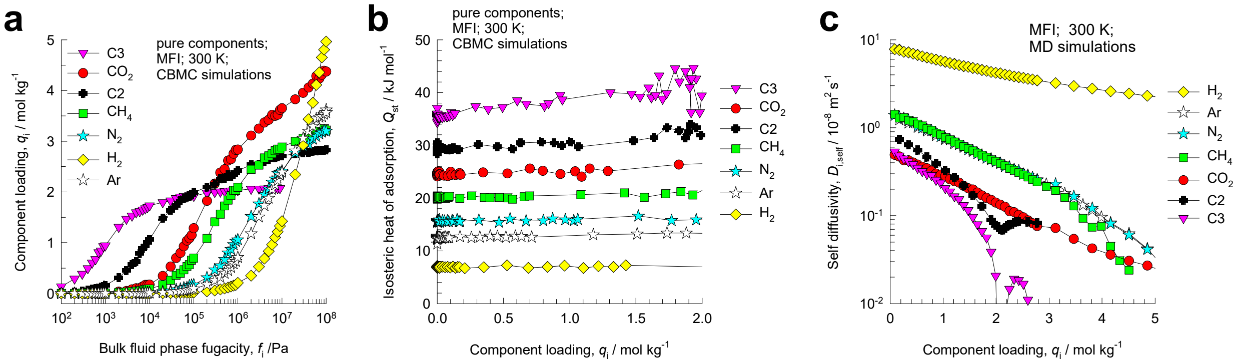

Figure S9. (a) CBMC simulations of unary adsorption isotherms, (b) CBMC simulations of isosteric heats of adsorption, and (c) MD simulations of unary self-diffusivities, $D_{\mathrm{i,self}}$, for a variety of guest molecules in MFI zeolite at 300 K.

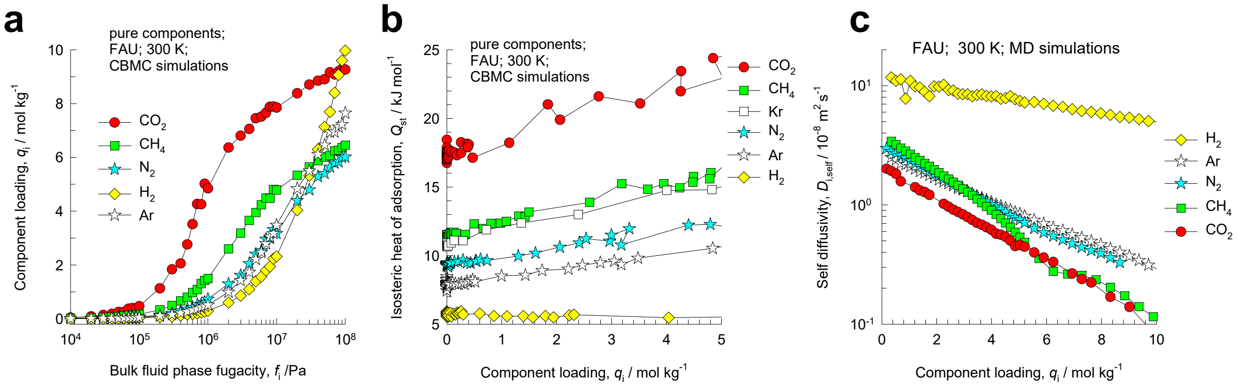

Figure S10. (a) CBMC simulations of unary adsorption isotherms, (b) CBMC simulations of isosteric heats of adsorption, and (c) MD simulations of unary self-diffusivities, $D_{i,self}$, for a variety of guest molecules in FAU all-silica zeolite at 300 K.

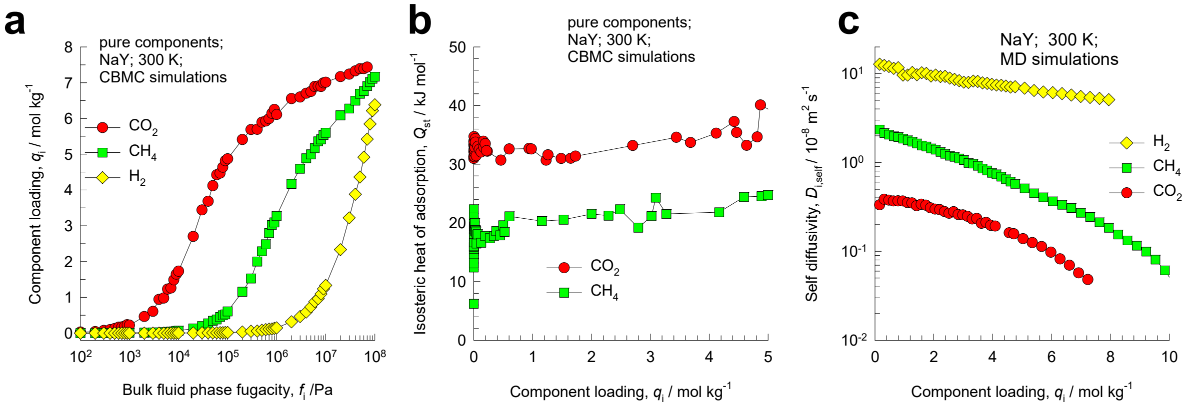

Figure S11. (a) CBMC simulations of unary adsorption isotherms, (b) CBMC simulations of isosteric heats of adsorption, and (c) MD simulations of unary self-diffusivities, $D_{i,self}$, for a variety of guest molecules in NaY zeolite.

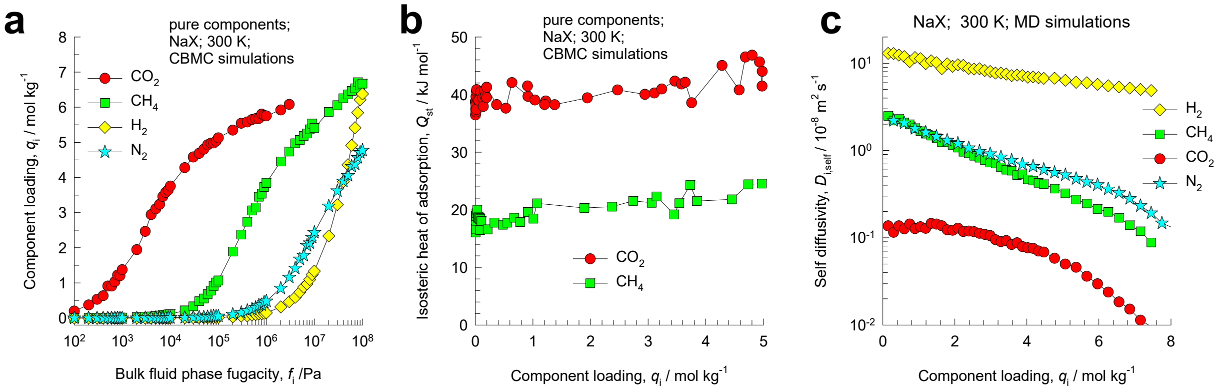

Figure S12. (a) CBMC simulations of unary adsorption isotherms, (b) CBMC simulations of isosteric heats of adsorption, and (c) MD simulations of unary self-diffusivities, $D_{i,self}$, for a variety of guest molecules in NaX zeolite.

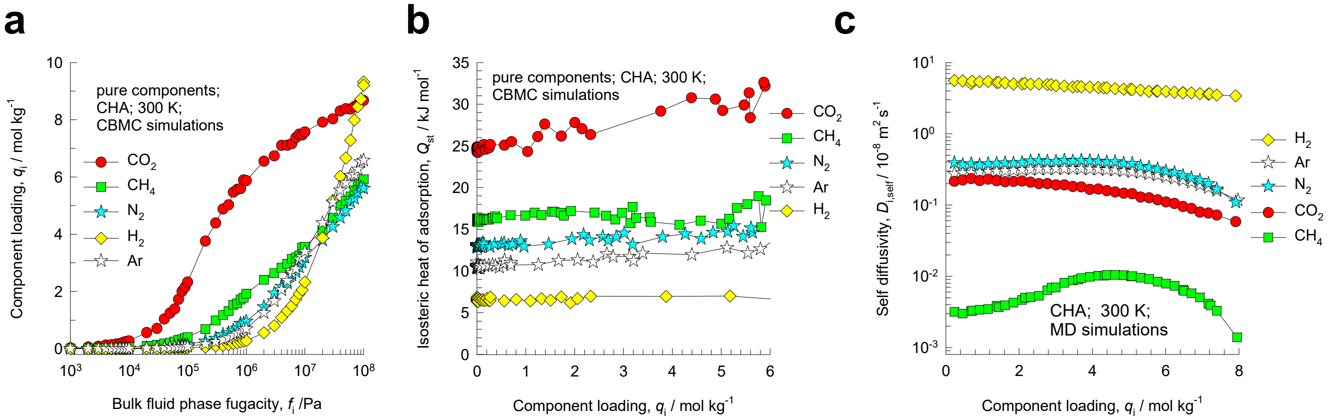

Figure S13. (a) CBMC simulations of unary adsorption isotherms, (b) CBMC simulations of isosteric heats of adsorption, and (c) MD simulations of unary self-diffusivities, $D_{i,self}$, for a variety of guest molecules in CHA all-silica zeolite at 300 K.

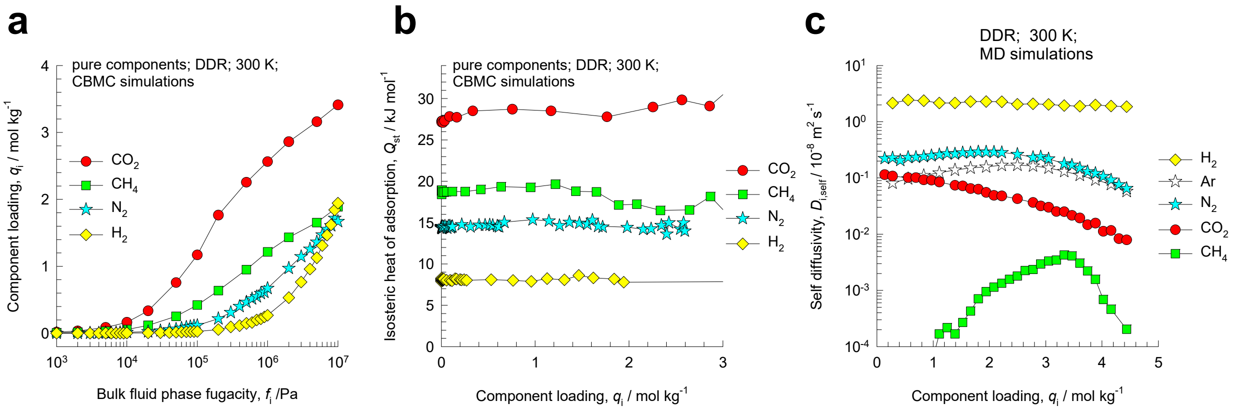

Figure S14. (a) CBMC simulations of unary adsorption isotherms, (b) CBMC simulations of isosteric heats of adsorption, and (c) MD simulations of unary self-diffusivities, $D_{i,self}$, for a variety of guest molecules in DDR all-silica zeolite at 300 K.

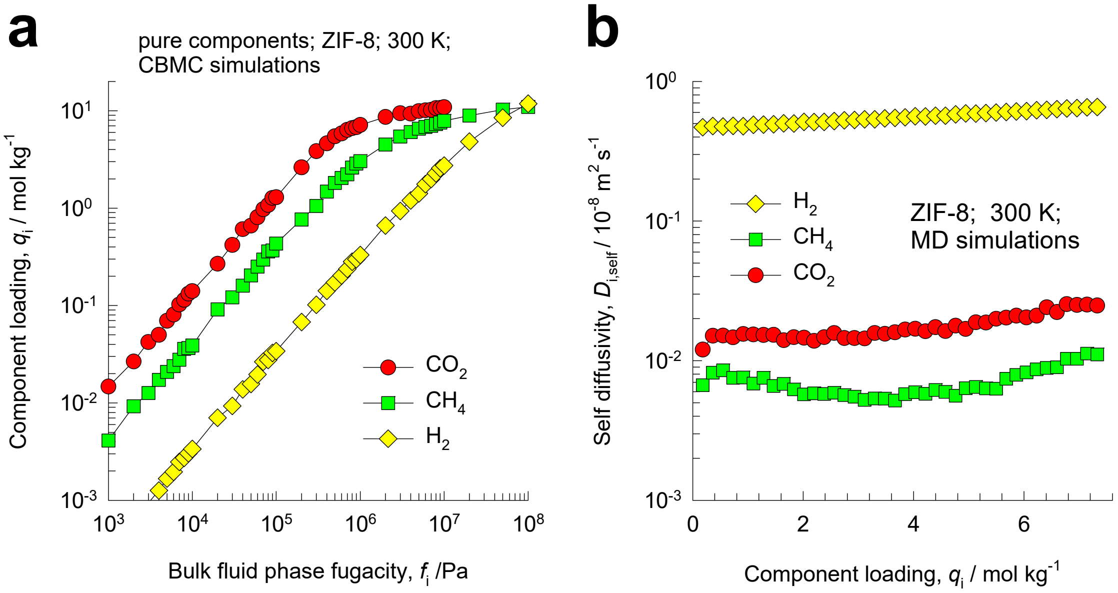

Figure S15. (a) CBMC simulations of unary adsorption isotherms, and (b) MD simulations of unary self-diffusivities, $D_{i,self}$, for a variety of guest molecules in ZIF-8 at 300 K.

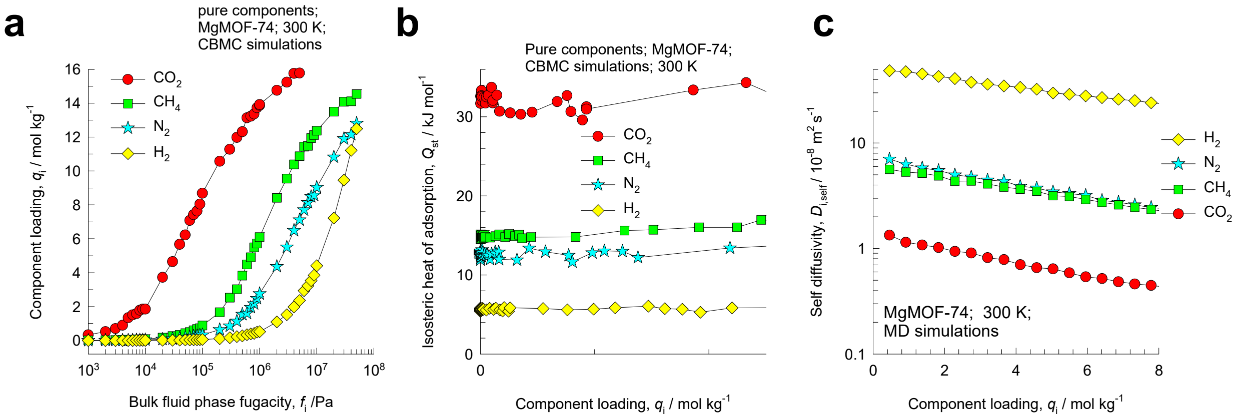

Figure S16. (a) CBMC simulations of unary adsorption isotherms, (b) CBMC simulations of isosteric heats of adsorption, and (c) MD simulations of unary self-diffusivities, $D_{i,self}$, for a variety of guest molecules in MgMOF-74 at 300 K.

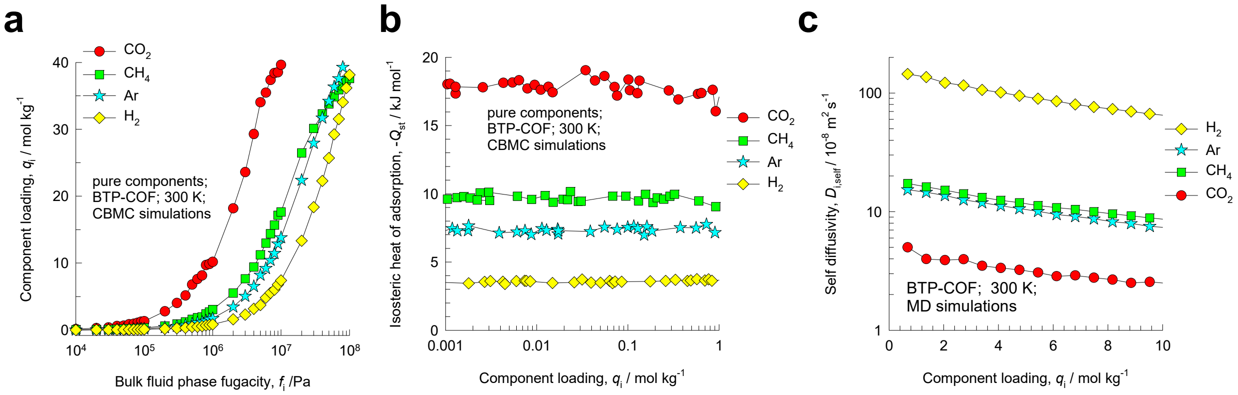

Figure S17. (a) CBMC simulations of unary adsorption isotherms, (b) CBMC simulations of isosteric heats of adsorption, and (c) MD simulations of unary self-diffusivities, $D_{i,self}$, for a variety of guest molecules in BTP-COF at 300 K.

8 Thermodynamic Non-Idealities in Investigated Systems

In our previous works[48-51, 61] we had investigated the influence of thermodynamic non-idealities on mixture adsorption. In this Chapter 8 we examine the accuracy of IAST calculations for the guest/host combinations investigated in this article.

8.1 CO_2/CH_4 mixture adsorption in all-silica CHA and DDR zeolites

A key assumption of the IAST is that the composition of the adsorbed phase is homogeneously and uniformly distributed within zeolite or metal-organic frameworks. Preferential location of molecules at certain locations within the crystalline, causes segregated adsorption and deviations from the assumption of homogeneous distribution. For separation of CO_2 from gaseous mixtures with CH_4, cage-type zeolites such as CHA, and DDR, CBMC simulations[62] show that the window regions of cage-type zeolites has a significantly higher proportion of CO_2 than within the cages. Due to preferential location of CO_2 in the window regions the CH_4 molecules experience a less severe competition from CO_2.

Figure S18a shows CBMC simulation data[62] of the adsorption selectivity, S_{ads}, for CO_2(1)/CH_4(2) mixtures in CHA zeolite at 300 K; the bulk gas phase mole fractions are maintained at $y_1 = y_2 = 0.5$, or $y_1 = y_2 = 0.15$ and S_{ads} is plotted as a function of the bulk gas mixture fugacity, $f_t = f_1 + f_2$. The dashed lines in Figure S18a are the IAST calculations using the unary isotherm fits as specified in Table S7. For $f_t = f_1 + f_2 > 1$ MPa, the IAST slightly overestimates the selectivity values because the competition faced by CH_4 is less severe because of the preferential location of CO_2 in the window regions, as evidenced by the snapshot in Figure S18.

Figure S18b shows CBMC simulation data[62] of adsorption selectivity, S_{ads}, for CO_2(1)/CH_4(2) mixtures in CHA zeolite at 300 K; the total bulk gas mixture fugacity is held constant, $f_t = f_1 + f_2 = 10^6$ Pa, and S_{ads} is plotted as a function of the bulk gas mixture of CO_2(1), y_1. The IAST calculations slightly overestimate the values of S_{ads} because the competitive adsorption is less severe due to the segregated nature of adsorption. In Figure S18c, the three different sets of data are plotted as function of the adsorption potential $\Phi \equiv \pi A/RT$. It is noteworthy, that the CBMC simulated data for S_{ads} is uniquely determined by $\Phi \equiv \pi A/RT$; this is because the deviations from IAST are not severe.

For all of the calculations for CHA as host we do not include the influence of thermodynamic non-idealities.

Segregation effects are stronger in DDR zeolite, and the IAST estimations are poorer at high values of the adsorption potential $\pi A/RT$. Figure S19a shows CBMC simulation data of the adsorption selectivity, S_{ads}, for CO_2(1)/CH_4(2) mixtures in DDR zeolite at 300 K; the bulk gas phase mole fractions are maintained at $y_1 = y_2 = 0.5$, and S_{ads} is plotted as a function of the bulk gas mixture fugacity, $f_t = f_1 + f_2$. The dashed lines in Figure S19a are the IAST calculations using the unary isotherm fits as specified in Table S8. For $f_t = f_1 + f_2 > 1$ MPa, the IAST overestimates the selectivity values because the competition faced by CH_4 is less severe because of the preferential location of CO_2 in the window regions, as evidenced by the snapshot in Figure S19.

Figure S19b shows CBMC simulation data of adsorption selectivity, S_{ads}, for CO_2(1)/CH_4(2) mixtures in DDR zeolite at 300 K; the total bulk gas mixture fugacity is held constant, $f_t = f_1 + f_2 = 10^6$ Pa, and S_{ads} is plotted as a function of the bulk gas mixture of CO_2(1), y_1. The IAST calculations are not in perfect agreement with CBMC data. In Figure S19c, both sets of data plotted as function of the adsorption potential $\Phi \equiv \pi A/RT$. It is noteworthy, that the CBMC simulated data are not uniquely determined by the adsorption potential, $\pi A/RT$, because the thermodynamic non-ideality effects are present to some degree.

For CO_2(1)/CH_4(2) mixtures in DDR zeolite at 300 K, we use the set of fitted Margules parameters $A_{12} = -12.6; \quad A_{21} = -4.7; \quad C = 0.01 \text{ mol kg}^{-1}$. For the adsorption of CO_2/H_2, and CO_2/N_2 mixtures in DDR zeolites, the IAST is used to describe mixture adsorption equilibrium.

8.2 CO_2/CH_4 and CO_2/N_2 mixture adsorption in NaX zeolite

Due to congregation of CO_2 around the Na+ cations of NaX zeolite, there is an inhomogeneous distribution of adsorbates within the pore landscape; this causes departures from the IAST as has been elucidated in our previous works. [48-51, 61]

Figure S20a shows CBMC simulation data of the adsorption selectivity, S_{ads}, for CO_2(1)/CH_4(2) mixtures in NaX zeolite at 300 K; the bulk gas phase mole fractions are maintained at $y_1 = y_2 = 0.5$, and S_{ads} is plotted as a function of the bulk gas mixture fugacity, $f_t = f_1 + f_2$. The dashed lines in Figure S20a are the IAST calculations using the unary isotherm fits. For $f_t = f_1 + f_2 > 1$ MPa, the IAST overestimates the selectivity values because the competition faced by CH_4 is less severe because of the preferential congregation of CO_2 around cations.[49]

Figure S20b shows CBMC simulation data of adsorption selectivity, S_{ads}, for CO_2(1)/CH_4(2) mixtures in NaX zeolite at 300 K; the total bulk gas mixture fugacity is held constant, $f_t = f_1 + f_2 = 10^5$ Pa, and S_{ads} is plotted as a function of the bulk gas mixture of CO_2(1), y_1. The IAST calculations overestimate the selectivties. In Figure S20c, both sets of data plotted as function of the adsorption potential $\Phi \equiv \pi A/RT$. It is noteworthy, that despite the non-idealities, the two sets of CBMC data are uniquely determined by $\Phi \equiv \pi A/RT$. For CO_2(1)/CH_4(2) mixtures in NaX zeolite at 300 K, we use the set of fitted Margules parameters $A_{12} = -0.632; \quad A_{21} = -0.693; \quad C = 1.021$ mol kg^{-1}.

The corresponding CBMC data for CO_2(1)/N_2(2) mixtures in NaX zeolite at 300 K are shown in Figure S21. Also for this mixture, we note that despite the non-idealities, the two sets of CBMC data are uniquely determined by $\Phi \equiv \pi A/RT$.

For the adsorption of CO_2/H_2, and CO_2/N_2 mixtures in NaX, the IAST is used to describe mixture adsorption equilibrium.

8.3 List of Figures for Thermodynamic Non-Idealities in Investigated Systems

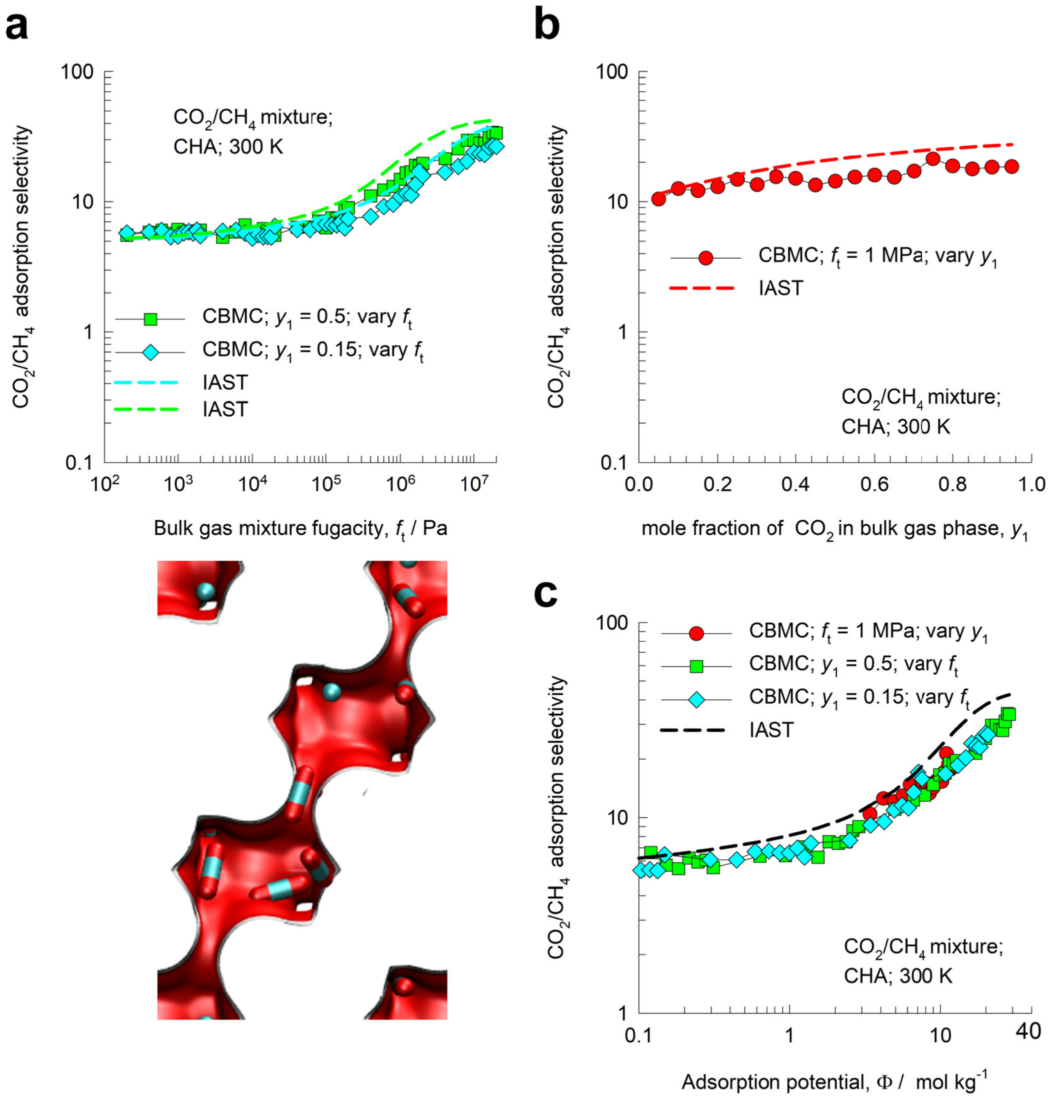

Figure S18. (a, b, c) CBMC simulations of the adsorption selectivity, S_{ads}, for CO$_2$(1)/CH$_4$(2) mixtures in CHA zeolite at 300 K. In (a) the bulk gas phase mole fractions are maintained at $y_1 = y_2 = 0.5$, and S_{ads} is plotted as a function of the bulk gas mixture fugacity, $f_t = f_1 + f_2$. In (b) the total bulk gas mixture fugacity is held constant, $f_t = f_1 + f_2 = 10^6$ Pa, and S_{ads} is plotted as a function of the bulk gas mole fraction of CO$_2$(1), y_1. In (c) both sets of data are plotted as function of the adsorption potential $\Phi \equiv \pi A/RT$. The dashed lines are the IAST calculations; the unary isotherm fit parameters are provided in Table S7.

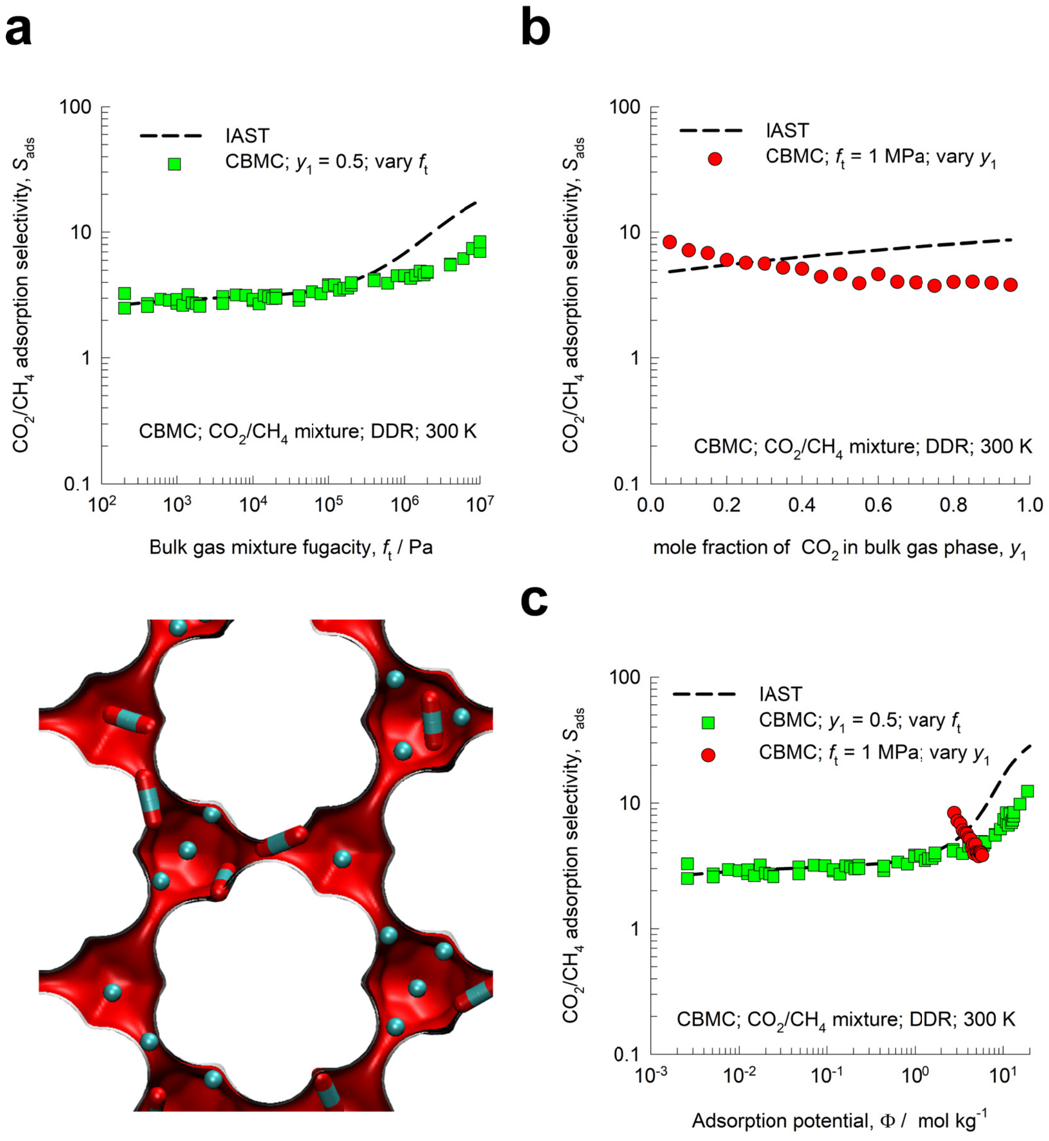

Figure S19. (a, b, c) CBMC simulations of the adsorption selectivity, S_{ads}, for CO_2(1)/CH_4(2) mixtures in DDR zeolite at 300 K. In (a) the bulk gas phase mole fractions are maintained at $y_1 = y_2 = 0.5$, and S_{ads} is plotted as a function of the bulk gas mixture fugacity, $f_t = f_1 + f_2$. In (b) the total bulk gas mixture fugacity is held constant, $f_t = f_1 + f_2 = 10^6$ Pa, and S_{ads} is plotted as a function of the bulk gas mole fraction of CO_2(1), y_1. In (c) both sets of data are plotted as function of the adsorption potential $\Phi \equiv \pi A / RT$. The dashed lines are the IAST calculations. The unary isotherm fit parameters are provided in Table S8.

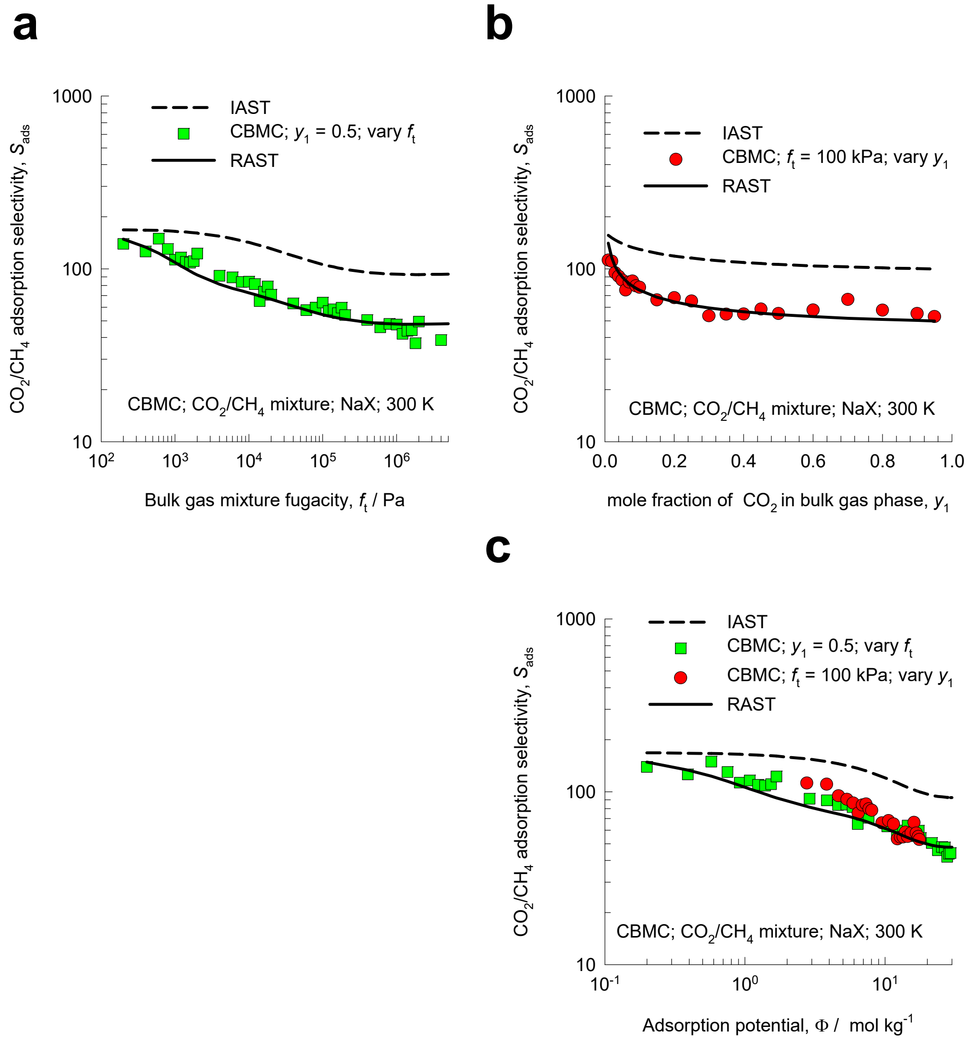

Figure S20. (a, b, c) CBMC simulations of the adsorption selectivity, S_{ads}, for $CO_2(1)/CH_4(2)$ mixtures in NaX zeolite at 300 K. In (a) the bulk gas phase mole fractions are maintained at $y_1 = y_2 = 0.5$, and S_{ads} is plotted as a function of the bulk gas mixture fugacity, $f_t = f_1 + f_2$. In (b) the total bulk gas mixture fugacity is held constant, $f_t = f_1 + f_2 = 10^5$ Pa, and S_{ads} is plotted as a function of the bulk gas mole fraction of $CO_2(1)$, y_1. In (c) both sets of data are plotted as function of the adsorption potential $\Phi \equiv \pi A/RT$. The dashed lines are the IAST calculations. The unary isotherm fit parameters are provided in Table S6.

Thermodynamic Non-Idealities in Investigated Systems

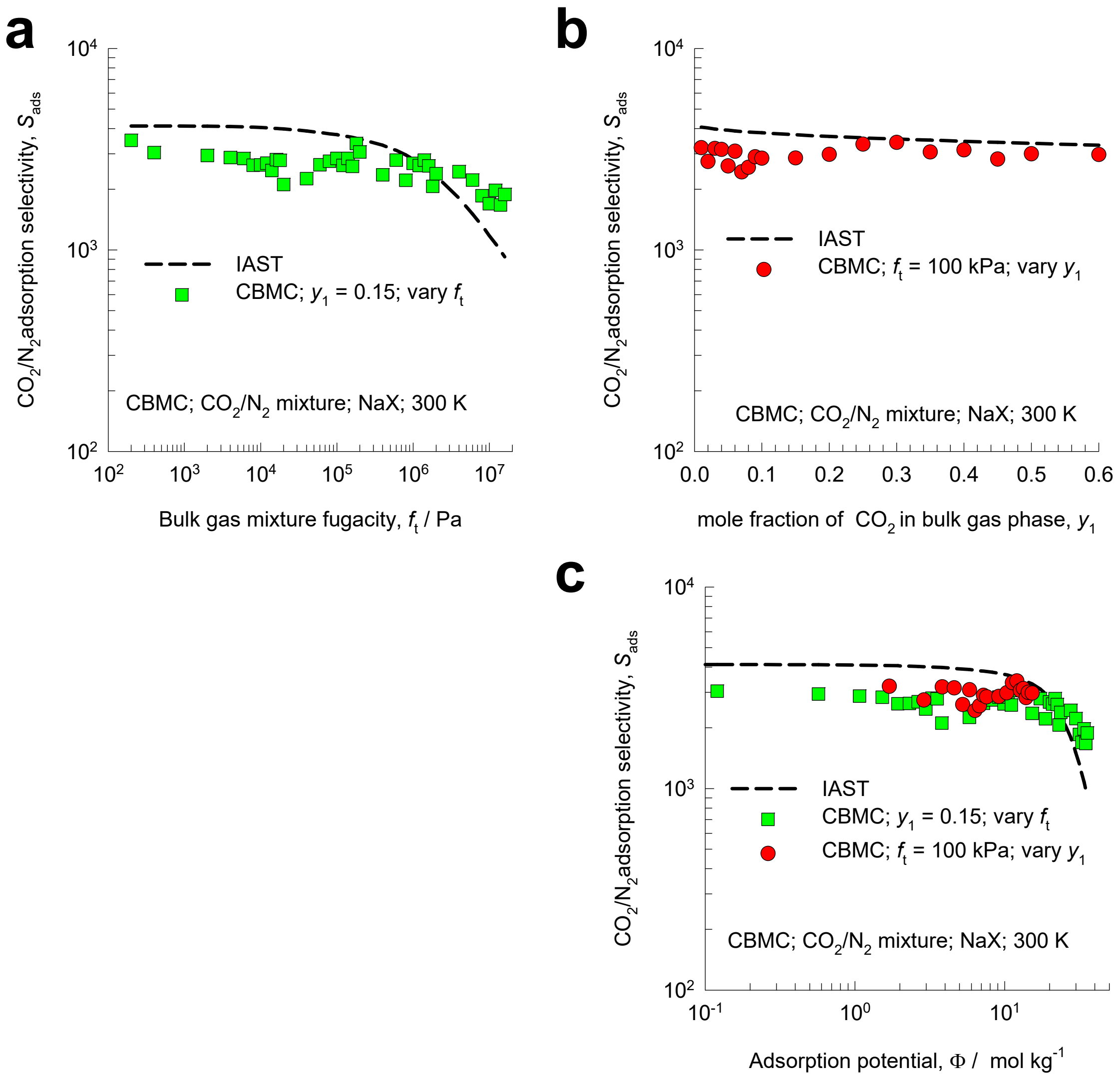

Figure S21. (a, b, c) CBMC simulations of the adsorption selectivity, S_{ads}, for CO$_2$(1)/N$_2$(2) mixtures in NaX zeolite at 300 K. In (a) the bulk gas phase mole fractions are maintained at $y_1 \;=\; y_2 \;= 0.15$, and S_{ads} is plotted as a function of the bulk gas mixture fugacity, $f_t \;= f_1 + f_2$. In (b) the total bulk gas mixture fugacity is held constant, $f_t \;= f_1 + f_2 = 10^5$ Pa, and S_{ads} is plotted as a function of the bulk gas mole fraction of CO$_2$(1), y_1. In (c) both sets of data are plotted as function of the adsorption potential $\Phi \equiv \pi A / RT$. The dashed lines are the IAST calculations. The unary isotherm fit parameters are provided in Table S6.

9 Permeation of Binary Mixtures in Microporous Materials

MD simulations were performed to determine the self-diffusivities $D_{i,self}$ in a variety of equimolar ($q_1 = q_2$) binary mixtures. In a few cases, the MD simulations were performed for mixtures in which the total loading $q_t = q_1 + q_2$ was held constant and the mole fraction of the adsorbed phase mixture, $x_1 = \frac{q_1}{q_1 + q_2}$ was varied from 0 to 1. All MD simulations reported in this work were conducted at a temperature $T = 300$ K.

For the interpretation and analysis of the MD simulations for binary mixture diffusion in microporous host materials, the IAST calculation procedure has to be performed differently because in the MD simulations, the molar loadings q_1, and q_2 in the mixture are specified, and the partial fugacities in the bulk fluid mixture are not known *a priori*. Also in this case, the equalities in equation (S11) must be satisfied in conjunction with equation (S13). The entire set of equations (S6) to (S13) need to be solved numerically to obtain the partial fugacities, f_i of the individual components in the mixture, that yield the same loadings as chosen in the MD simulations. The IAST calculations (note that RAST is used in the case of CO_2/CH_4/NaX, CO_2/CH_4/DDR) also determine the adsorption potential, $\Phi \equiv \frac{\pi A}{RT}$. In all of the calculations presented in this article, the set of equations were solved using an Excel macro that was developed for this specific purpose.

For use of the materials in membrane constructs, the permeability of the membrane, Π_i, is defined by

$$\Pi_i = \frac{N_i}{\Delta f_i / \delta} \tag{S45}$$

where N_i is the permeation flux, δ is the thickness of the crystalline layer on the membrane, and $\Delta f_i = f_{i0} - f_{i\delta}$ is the difference in the partial fugacities in the bulk fluid mixtures in the upstream ($z = 0$) and downstream ($z = \delta$) compartments. If the downstream conditions are such that the loadings are negligibly small, the permeability can be determined from MD simulations by using the following expression[12]

$$\Pi_i = \frac{\rho D_{i,self} q_i}{f_i} \tag{S46}$$

where ρ is the crystal framework density. In SI units, the permeability has the units mol m m^{-2} s^{-1} Pa^{-1}. The more commonly used engineering unit for permeability is the Barrer expressed in cm^3 (STP) cm cm^{-2} s^{-1} $(cm\ Hg)^{-1}$. To convert to the commonly used engineering units of Barrers we divide the value in mol m m^{-2} s^{-1} Pa^{-1} by 3.348×10^{-16}.

Often in experimental investigations of membrane permeation, the precise thickness of the membrane is not easily determinable and, therefore, the experimental data are presented in terms of the permeances calculated from

$$\frac{N_i}{\Delta f_i} \equiv \frac{\Pi_i}{\delta} \tag{S47}$$

In SI units, the permeance has the units mol m^{-2} s^{-1} Pa^{-1}.

The obtained data for the self-diffusivities $D_{i,self}$ and permeabilities Π_i for each guest/host combination are plotted as function of the adsorption potential, $\Phi \equiv \frac{\pi A}{RT}$ in the set of Figures as specified hereunder. Also plotted in the same set of Figures are the values of $D_{i,self}$ and permeabilities Π_i for the corresponding guest/host combination for each unary guest, plotted as function of the adsorption potential, $\Phi \equiv \frac{\pi A}{RT}$ for the corresponding unary guests.

Figure S22, Figure S23, Figure S24, Figure S25: various mixtures in CHA zeolite

Figure S26, Figure S27,Figure S28: various mixtures in DDR zeolite

Figure S29, Figure S30: various mixtures in ZIF-8

Figure S32, Figure S33, Figure S34: various mixtures in BTP-COF mesoporous host

Figure S35, Figure S36, Figure S37, Figure S38, Figure S39: various mixtures in MgMOF-74

Figure S40, Figure S41, Figure S42: various mixtures in all-silica FAU zeolite

Figure S43, Figure S44,Figure S45: various mixtures in NaY zeolite

Figure S46, Figure S47, Figure S48: various mixtures in NaX zeolite

Figure S49, Figure S50, Figure S51, Figure S52, Figure S53, Figure S53: various mixtures in all-silica MFI zeolite.

In order to underscore the advantages of using adsorption potential, $\Phi \equiv \frac{\pi A}{RT}$ as *x*-axes for plotting the data on self-diffusivities and permeabilities, let us consider MD simulation data on self-diffusivities for binary CO_2/CH_4 mixtures in CHA zeolite at 300 K. For this mixture, four different MD simulation campaigns were conducted as follows:

(i) equimolar ($q_1 = q_2; \quad x_1 = 1 - x_2 = 0.5$) mixtures with varying total load, $q_t = q_1 + q_2$; indicated by green squares

(ii) mixtures at constant load $q_t = 5.78$ mol kg^{-1} (= 25 molecules uc^{-1}) and varying mole fraction of CO_2 in the adsorbed phase, $x_1 = q_1/q_t$; indicate by red circles,

(iii) mixtures at constant load $q_t = 2.89$ mol kg^{-1} (= 12.5 molecules uc^{-1}) and varying mole fraction of CO_2 in the adsorbed phase, $x_1 = q_1/q_t$; indicated by inverted pink triangles, and

(iv) mixtures in which the CH_4 load $q_2 = 0.693$ mol kg^{-1} (= 3 molecules uc^{-1}) and loadings of CO_2, q_1 are varied; indicated by blue triangles.

In Figure S22a the $S_{diff}=\frac{D_{1,self}}{D_{2,self}}$ data for campaign (i) are plotted as function of $q_t=q_1+q_2$. The diffusion selectivities decrease strongly with increasing total loading. In Figure S22b the $S_{diff}=\frac{D_{1,self}}{D_{2,self}}$ data for campaigns (ii), (iii), and (iv) are plotted as function of the mole fraction of CO_2 in the adsorbed phase, $x_1=q_1/q_t$. The diffusion selectivities are also influenced by the mixture composition. The four sets of data on diffusion selectivities are plotted in Figure S22c as function of the adsorption potential, $\Phi\equiv\frac{\pi A}{RT}$, indicating that the adsorption potential uniquely determines the diffusion selectivity.

In view of the fact that IAST also shows that the adsorption selectivity S_{ads} is also uniquely dependent on $\Phi\equiv\frac{\pi A}{RT}$, we should expect the permeation selectivity $S_{perm}=\frac{D_{1,self}q_1/f_1}{D_{2,self}q_2/f_2}=S_{ads}\times S_{diff}$ to be also uniquely dependent on $\Phi\equiv\frac{\pi A}{RT}$. The plot of S_{perm} vs Φ for the four data sets also lie on a unique curve; see Figure S22d.

9.1 List of Figures for Permeation of Binary Mixtures in Microporous Materials

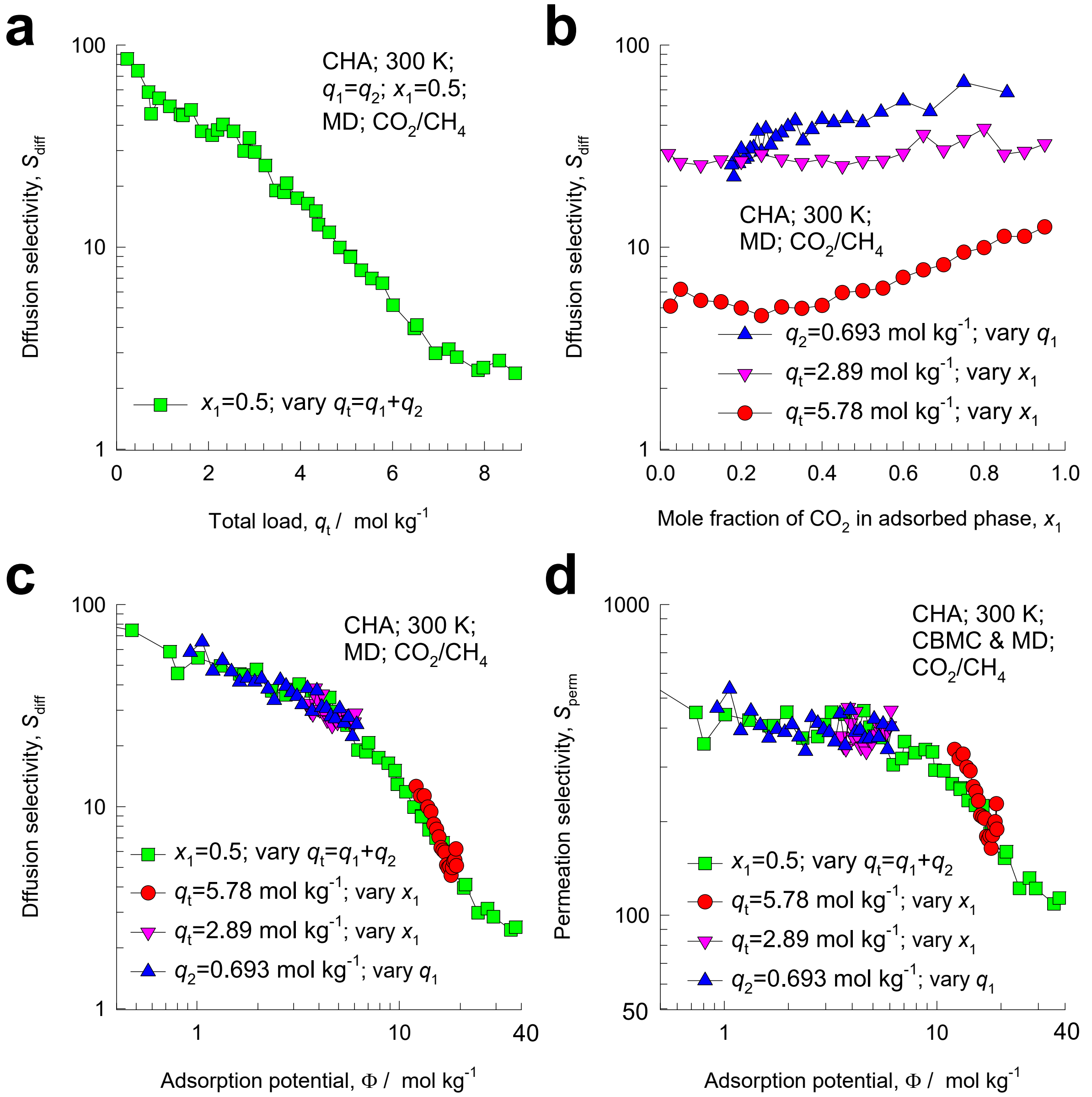

Figure S22. (a, b, c) MD simulations of the diffusion selectivities, S_{diff} for CO$_2$/CH$_4$ mixtures in CHA zeolite at 300 K, obtained from four different campaigns, plotted as a function of the (a) total load, q_t, (b) the mole fraction of CO$_2$ in the adsorbed phase, x_1, (c) the adsorption potential Φ. (d) The four sets of data for permeation selectivities S_{perm} are plotted as function of Φ.

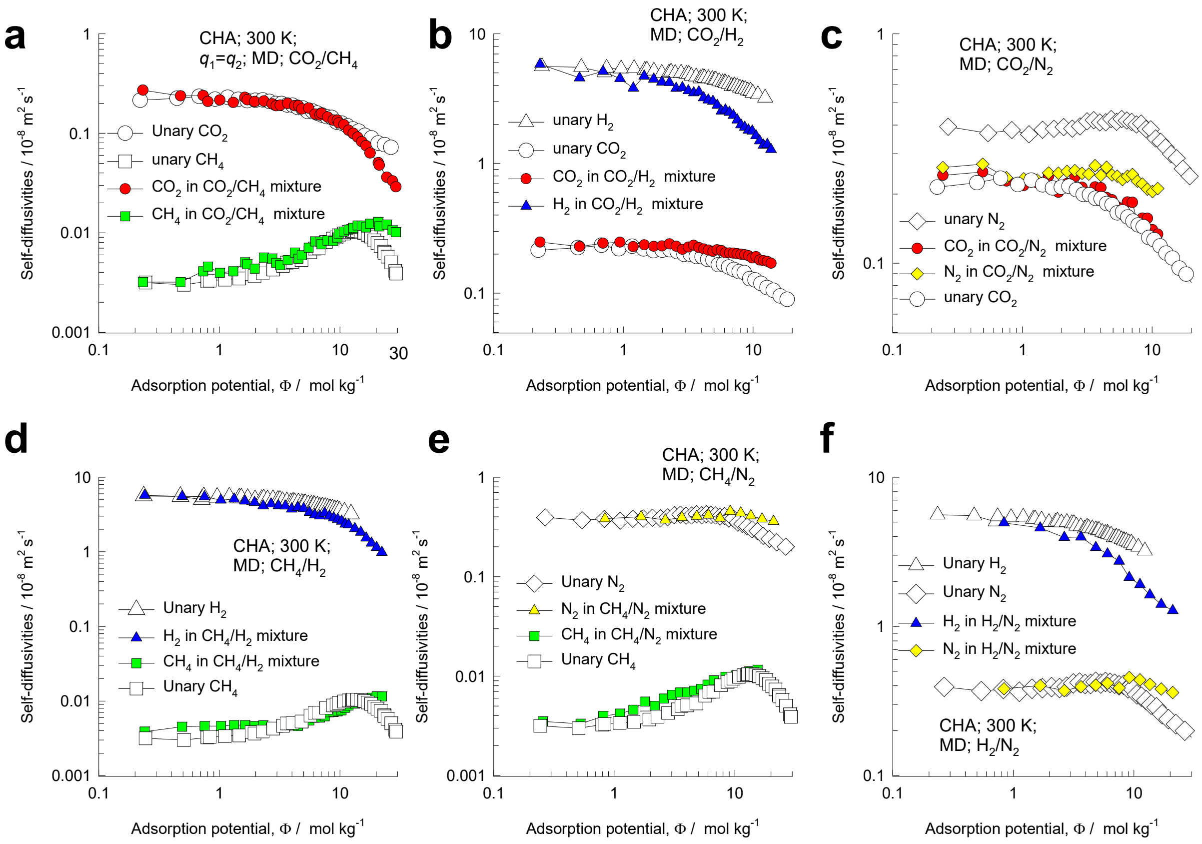

Figure S23. MD simulations of the self-diffusivities, $D_{i,self}$, of components in equimolar (q_1=q_2) binary (a) CO_2/CH_4, (b) CO_2/H_2, (c) CO_2/N_2, (d) CH_4/H_2, (e) CH_4/N_2, and (f) H_2/N_2 mixtures in CHA zeolite at 300 K, plotted as a function of the adsorption potential, $\Phi \equiv \pi A / RT$. Also plotted (using open symbols) are the corresponding values of the unary self-diffusivities.

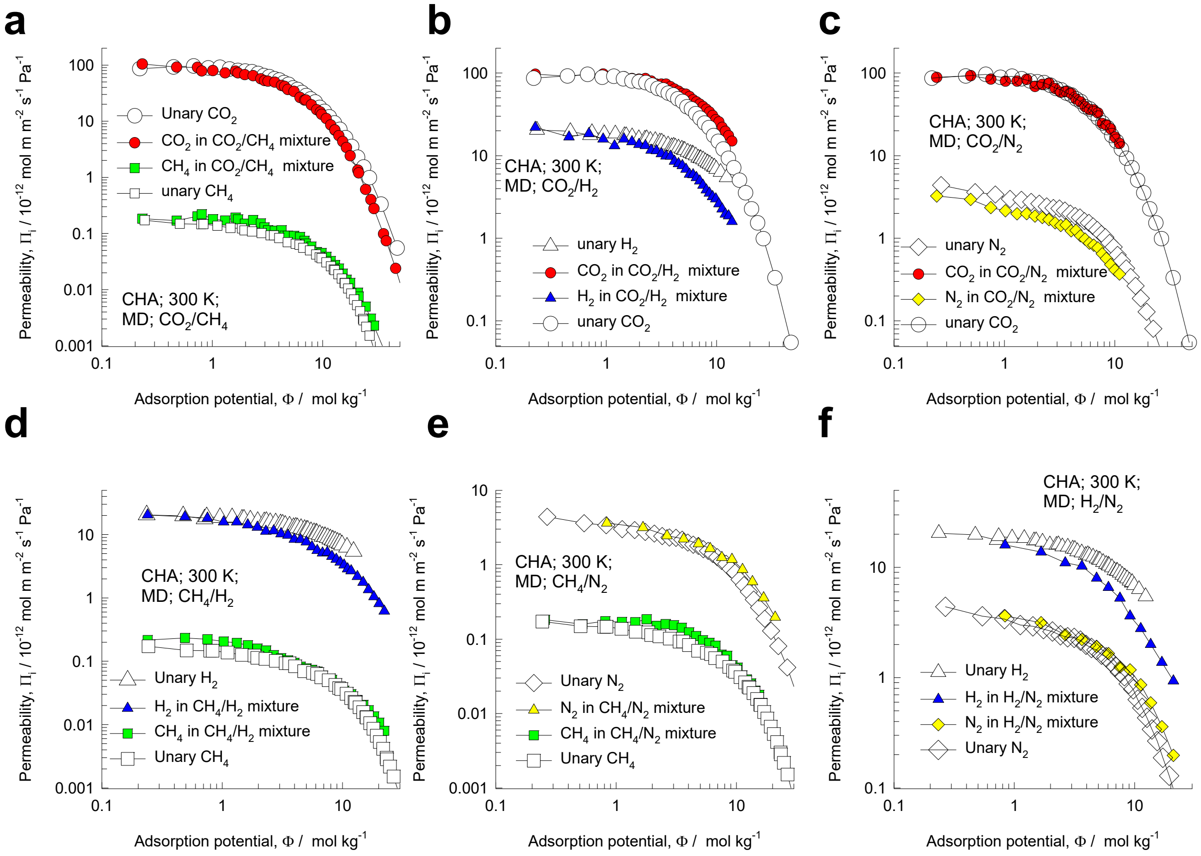

Figure S24. CBMC/MD simulations of the permeabilities, Π_i, of components in equimolar (q_1=q_2) binary (a) CO$_2$/CH$_4$, (b) CO$_2$/H$_2$, (c) CO$_2$/N$_2$, (d) CH$_4$/H$_2$, (e) CH$_4$/N$_2$, and (f) H$_2$/N$_2$ mixtures in CHA zeolite at 300 K, plotted as a function of the adsorption potential, $\Phi \equiv \pi A / RT$. Also plotted (using open symbols) are the corresponding values of the unary permeabilities.

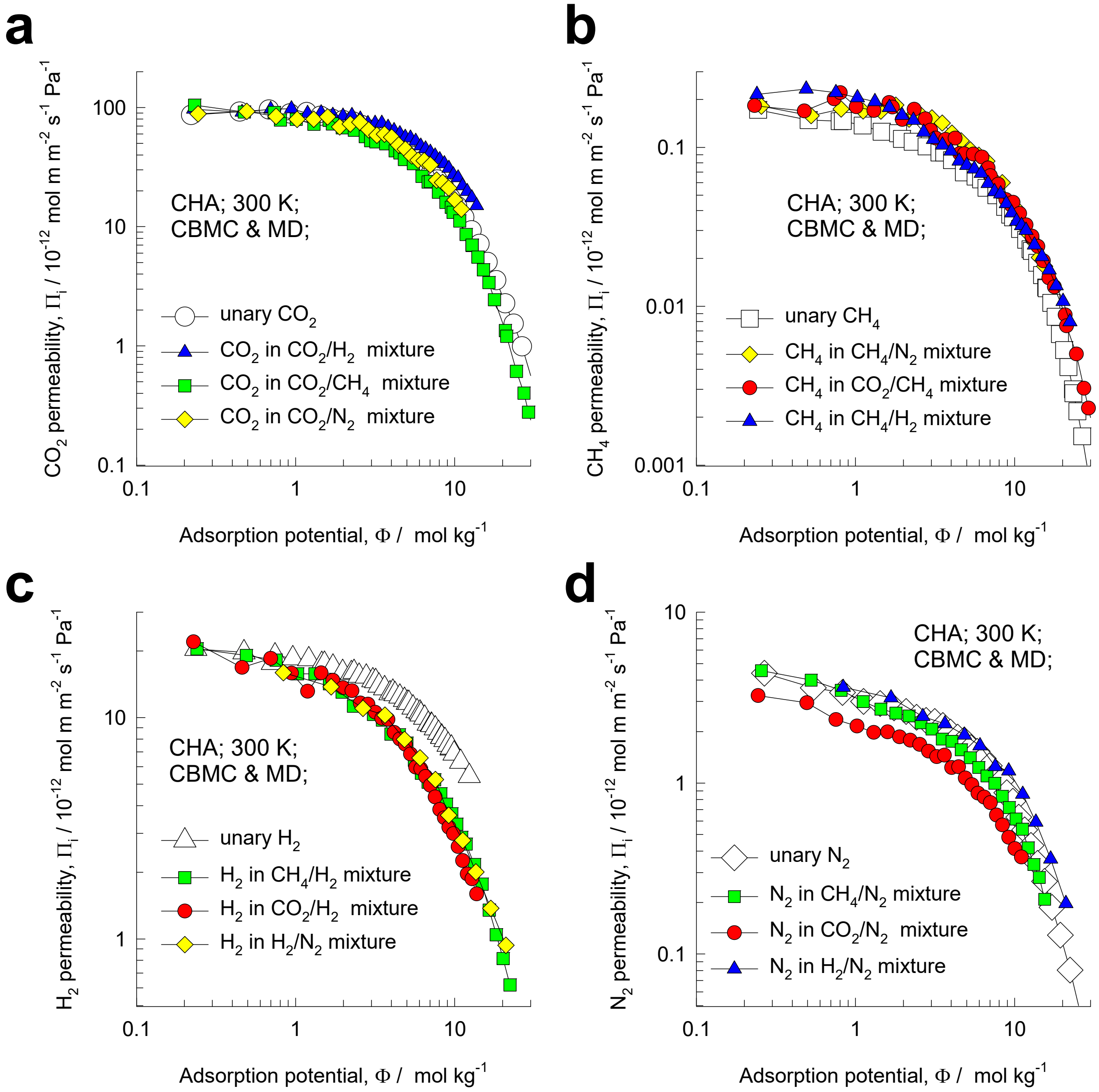

Figure S25. CBMC/MD simulations of the permeabilities, Π_i, of (a) CO_2, (b) CH_4, (c) H_2, and (d) N_2 in different equimolar (q_1=q_2) binary mixtures in CHA zeolite at 300 K, plotted as a function of the adsorption potential, $\Phi \equiv \pi A / RT$. Also plotted (using open symbols) are the corresponding values of the unary permeabilities.

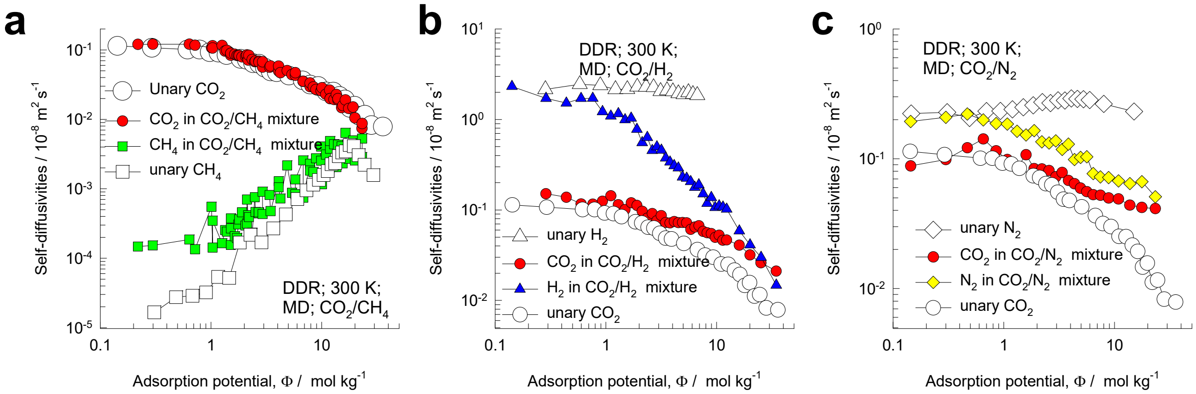

Figure S26. MD simulations of the self-diffusivities, $D_{i,self}$, of components in equimolar (q_1=q_2) binary (a) CO_2/CH_4, (b) CO_2/H_2, and (c) CO_2/N_2 mixtures in DDR zeolite at 300 K, plotted as a function of the adsorption potential, $\Phi \equiv \pi A / RT$. Also plotted (using open symbols) are the corresponding values of the unary self-diffusivities.

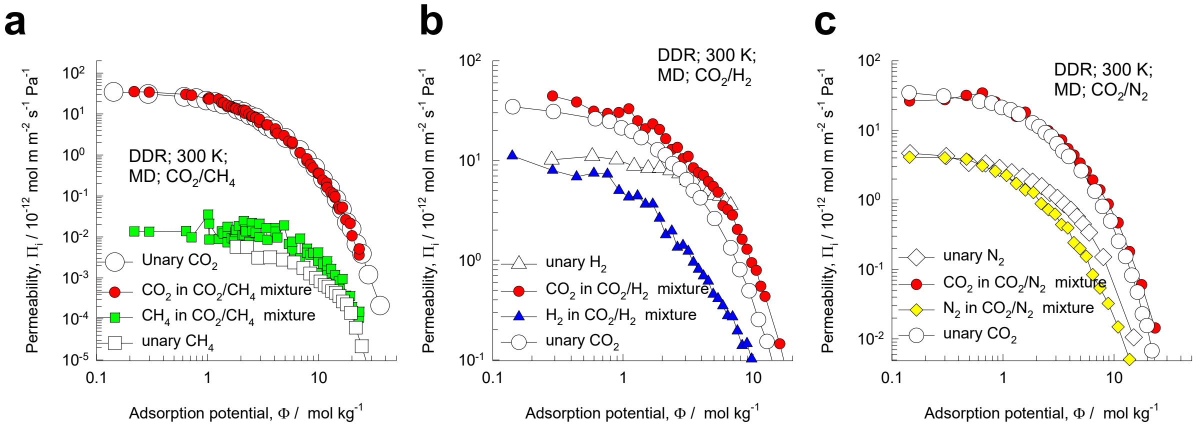

Figure S27. CBMC/MD simulations of the permeabilities, Π_i, of components in equimolar (q_1=q_2) binary (a) CO_2/CH_4, (b) CO_2/H_2, and (c) CO_2/N_2 mixtures in DDR zeolite at 300 K, plotted as a function of the adsorption potential, $\Phi \equiv \pi A / RT$. Also plotted (using open symbols) are the corresponding values of the unary permeabilities.

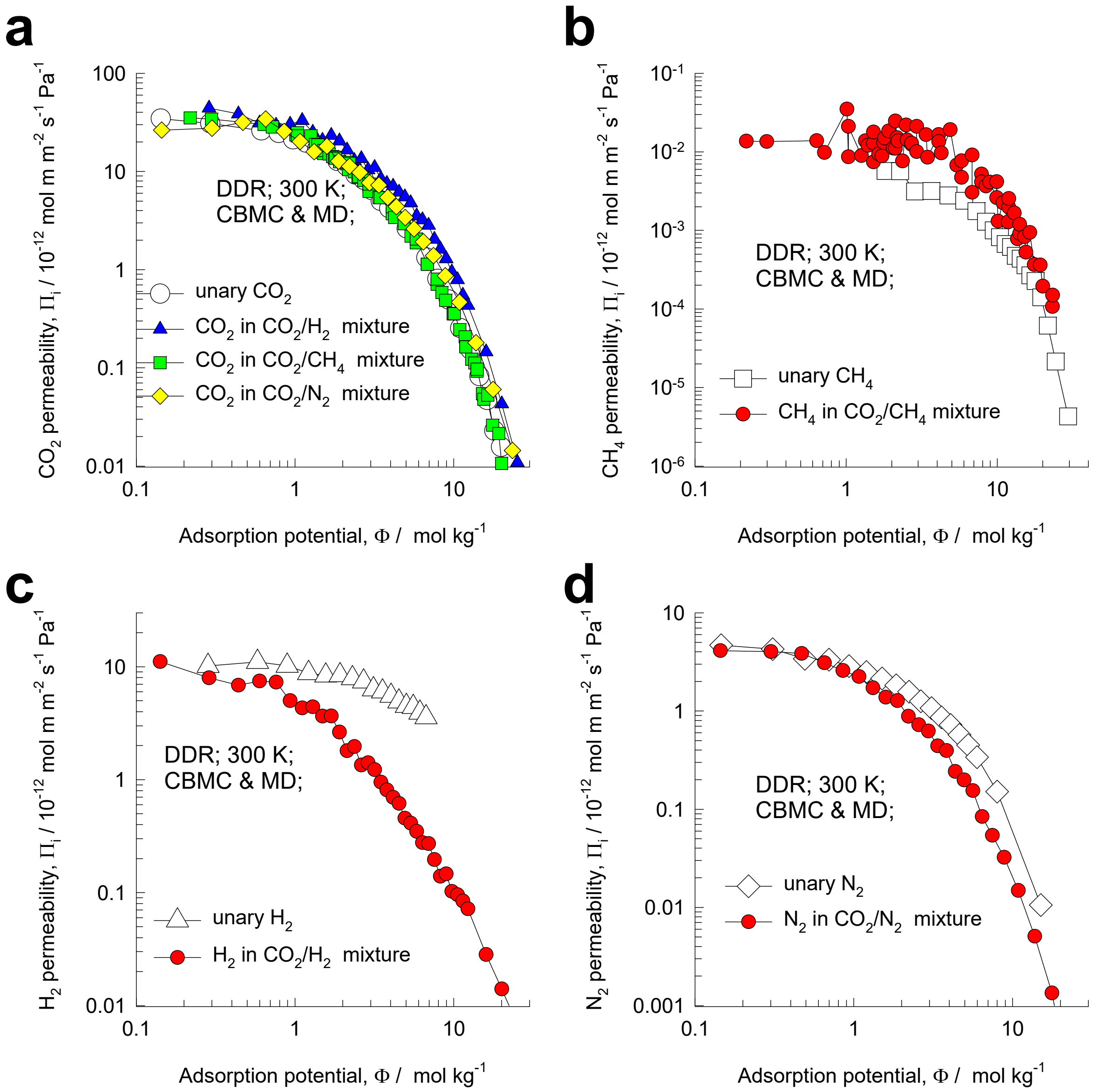

Figure S28. CBMC/MD simulations of the permeabilities, Π_i, of (a) CO_2, (b) CH_4, (c) H_2, and (d) N_2 in different equimolar (q_1=q_2) binary mixtures in DDR zeolite at 300 K, plotted as a function of the adsorption potential, $\Phi \equiv \pi A / RT$. Also plotted (using open symbols) are the corresponding values of the unary permeabilities.

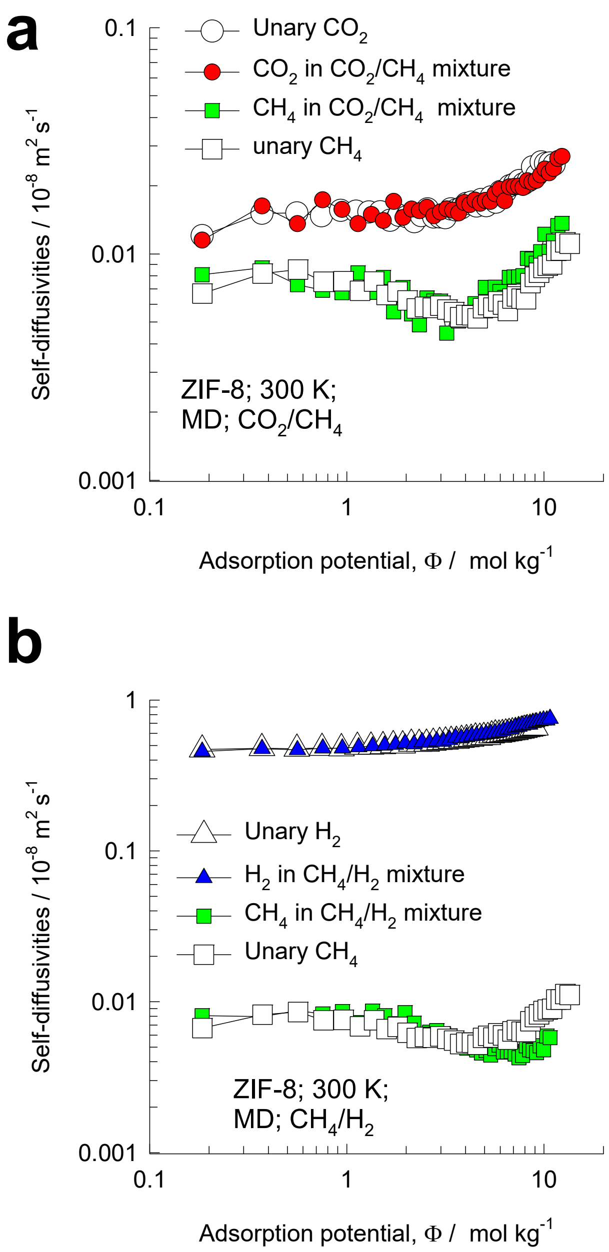

Figure S29. MD simulations of the self-diffusivities, $D_{i,self}$, of components in equimolar (q_1=q_2) binary (a) CO_2/CH_4, and (b) CH_4/H_2 mixtures in ZIF-8 at 300 K, plotted as a function of the adsorption potential, $\Phi \equiv \pi A / RT$. Also plotted (using open symbols) are the corresponding values of the unary self-diffusivities.

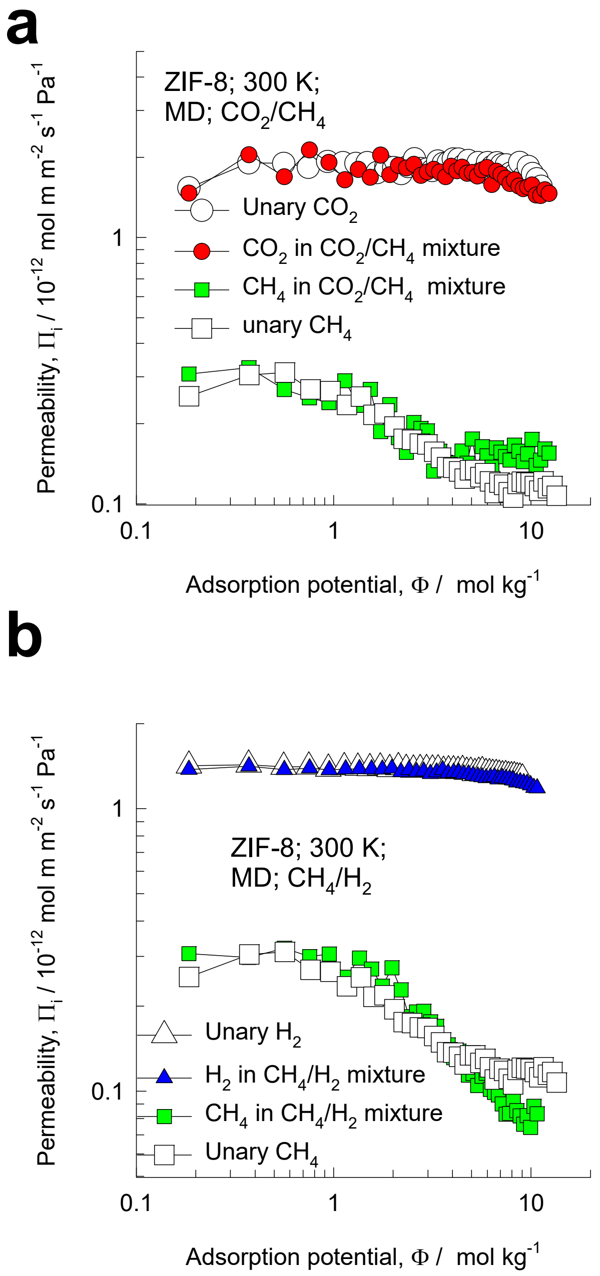

Figure S30. CBMC/MD simulations of the permeabilities, Π_i, of components in equimolar (q_1=q_2) binary (a) CO_2/CH_4, and (b) CH_4/H_2 mixtures in ZIF-8 at 300 K, plotted as a function of the adsorption potential, $\Phi \equiv \pi A / RT$. Also plotted (using open symbols) are the corresponding values of the unary permeabilities.

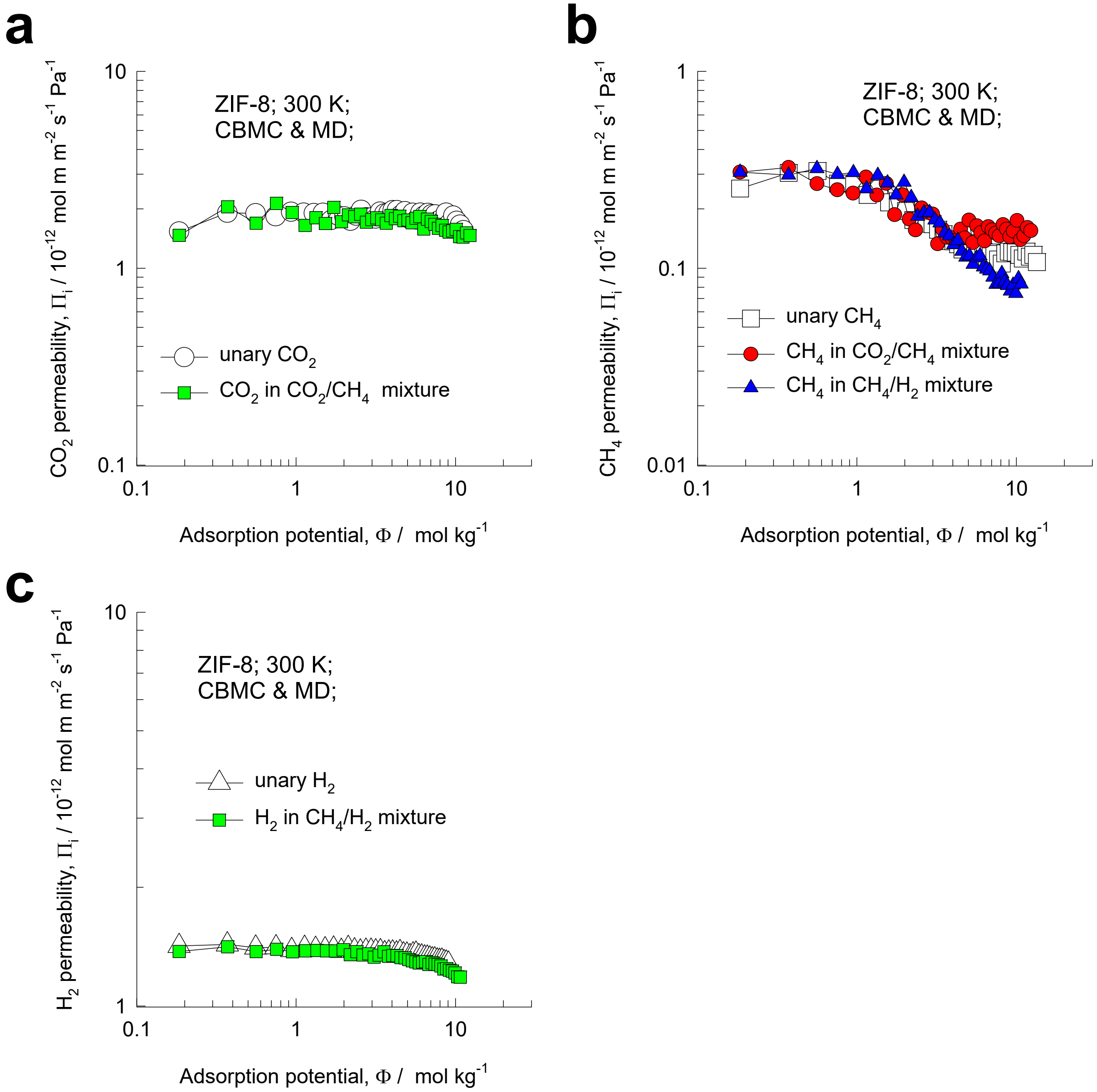

Figure S31. CBMC/MD simulations of the permeabilities, Π_i, of (a) CO_2, (b) CH_4, and (c) H_2 in different equimolar (q_1=q_2) binary mixtures in ZIF-8 at 300 K, plotted as a function of the adsorption potential, $\Phi \equiv \pi A / RT$. Also plotted (using open symbols) are the corresponding values of the unary permeabilities.

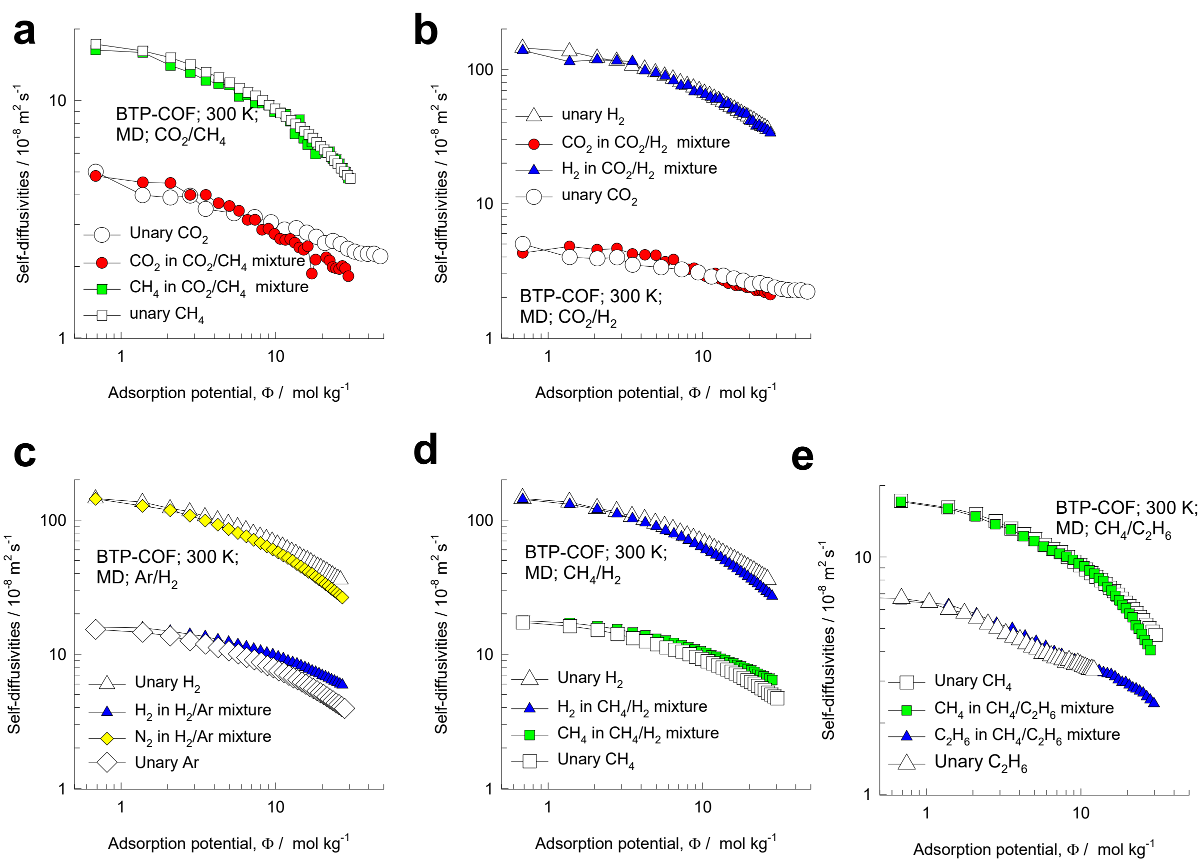

Figure S32. MD simulations of the self-diffusivities, $D_{i,self}$, of components in equimolar (q_1=q_2) binary (a) CO_2/CH_4, (b) CO_2/H_2, (c) Ar/H_2, (d) CH_4/H_2, and (e) CH_4/C_2H_6 mixtures in BTP-COF at 300 K, plotted as a function of the adsorption potential, $\Phi \equiv \pi A / RT$. Also plotted (using open symbols) are the corresponding values of the unary self-diffusivities.

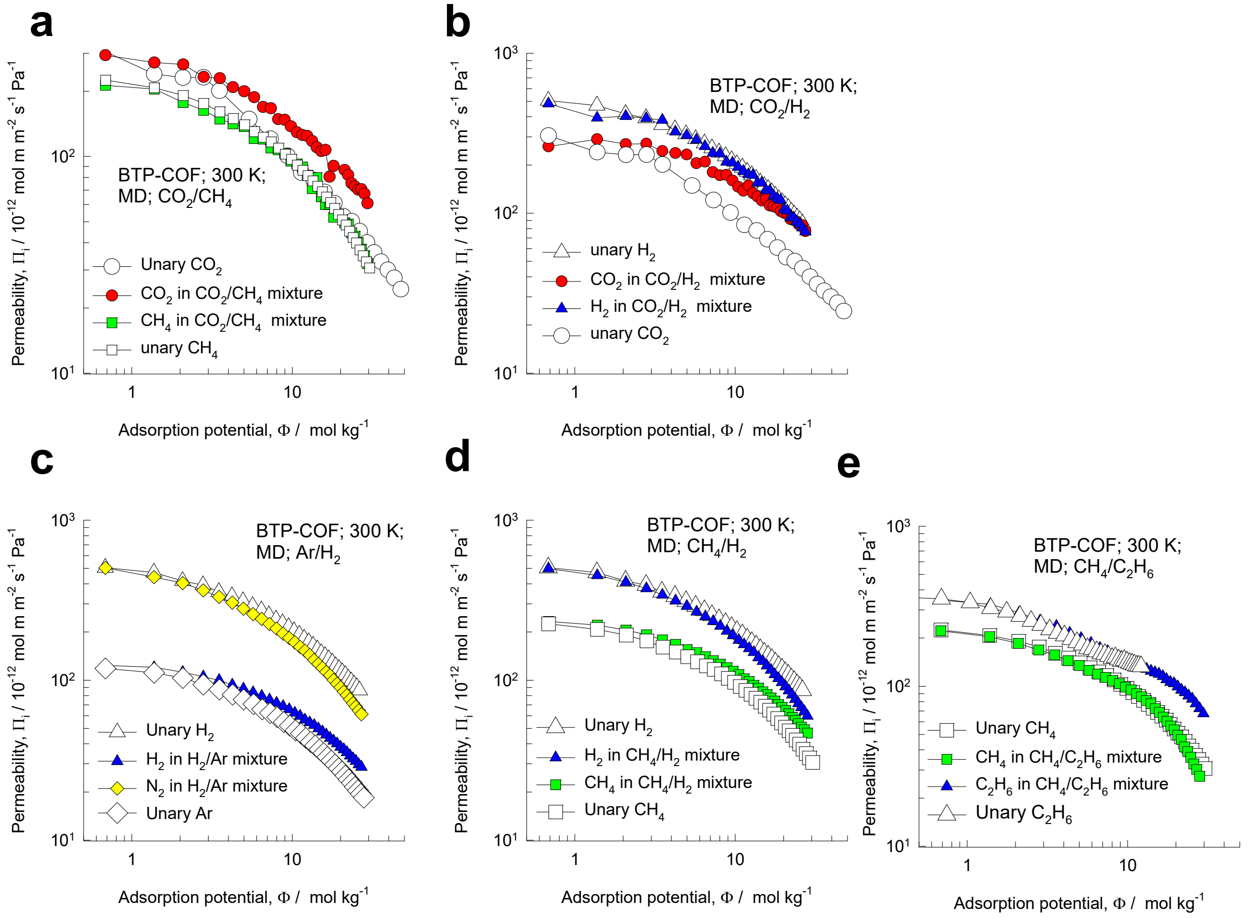

Figure S33. CBMC/MD simulations of the permeabilities, Π_i, of components in equimolar (q_1=q_2) binary (a) CO_2/CH_4, (b) CO_2/H_2, (c) Ar/H_2, (d) CH_4/H_2, and (e) CH_4/C_2H_6 mixtures in BTP-COF at 300 K, plotted as a function of the adsorption potential, $\Phi \equiv \pi A / RT$. Also plotted (using open symbols) are the corresponding values of the unary permeabilities.

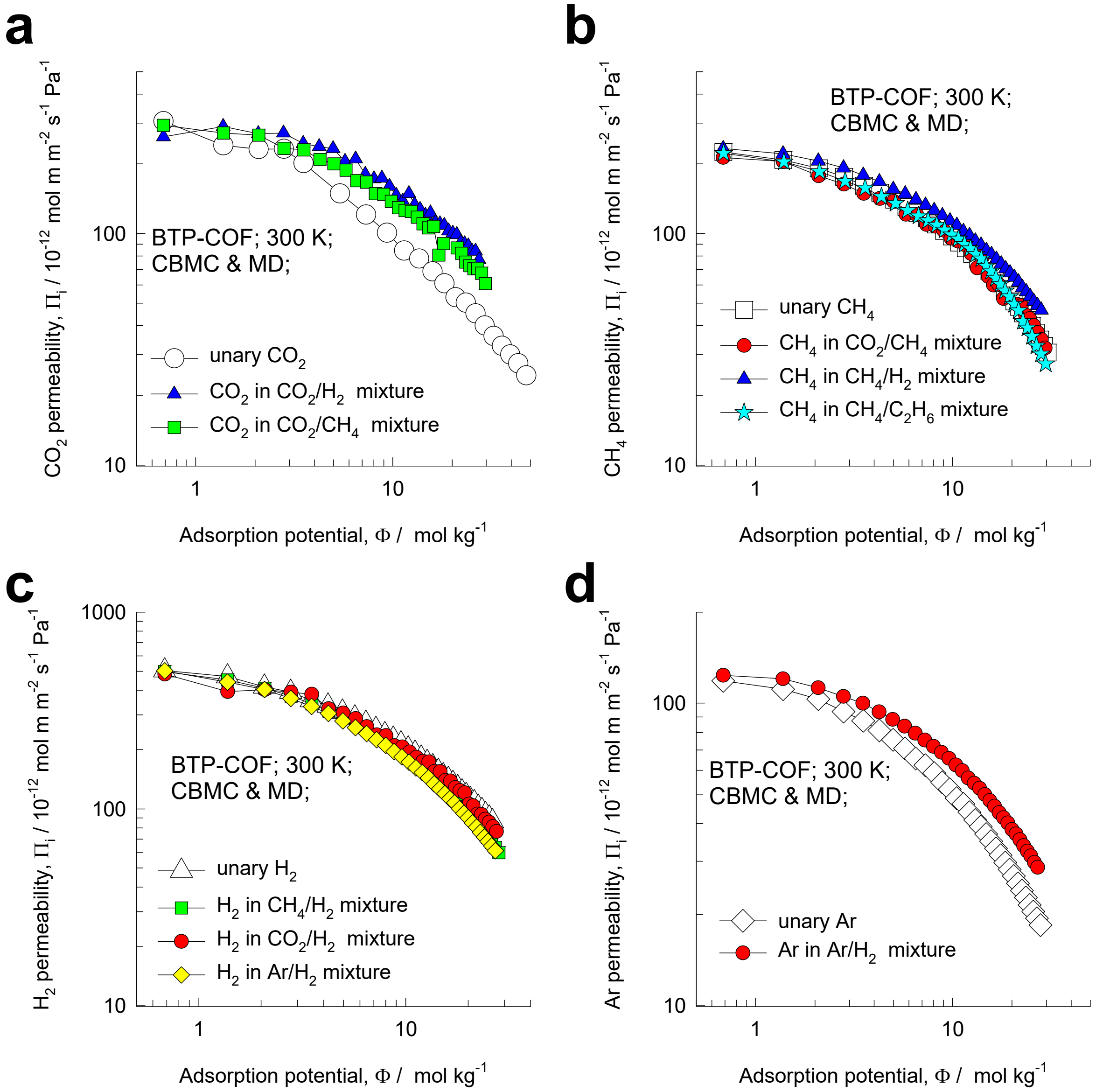

Figure S34. CBMC/MD simulations of the permeabilities, Π_i, of (a) CO$_2$, (b) CH$_4$, (c) H$_2$, and (d) Ar in different equimolar (q_1=q_2) binary mixtures in BTP-COF at 300 K, plotted as a function of the adsorption potential, $\Phi \equiv \pi A / RT$. Also plotted (using open symbols) are the corresponding values of the unary permeabilities.

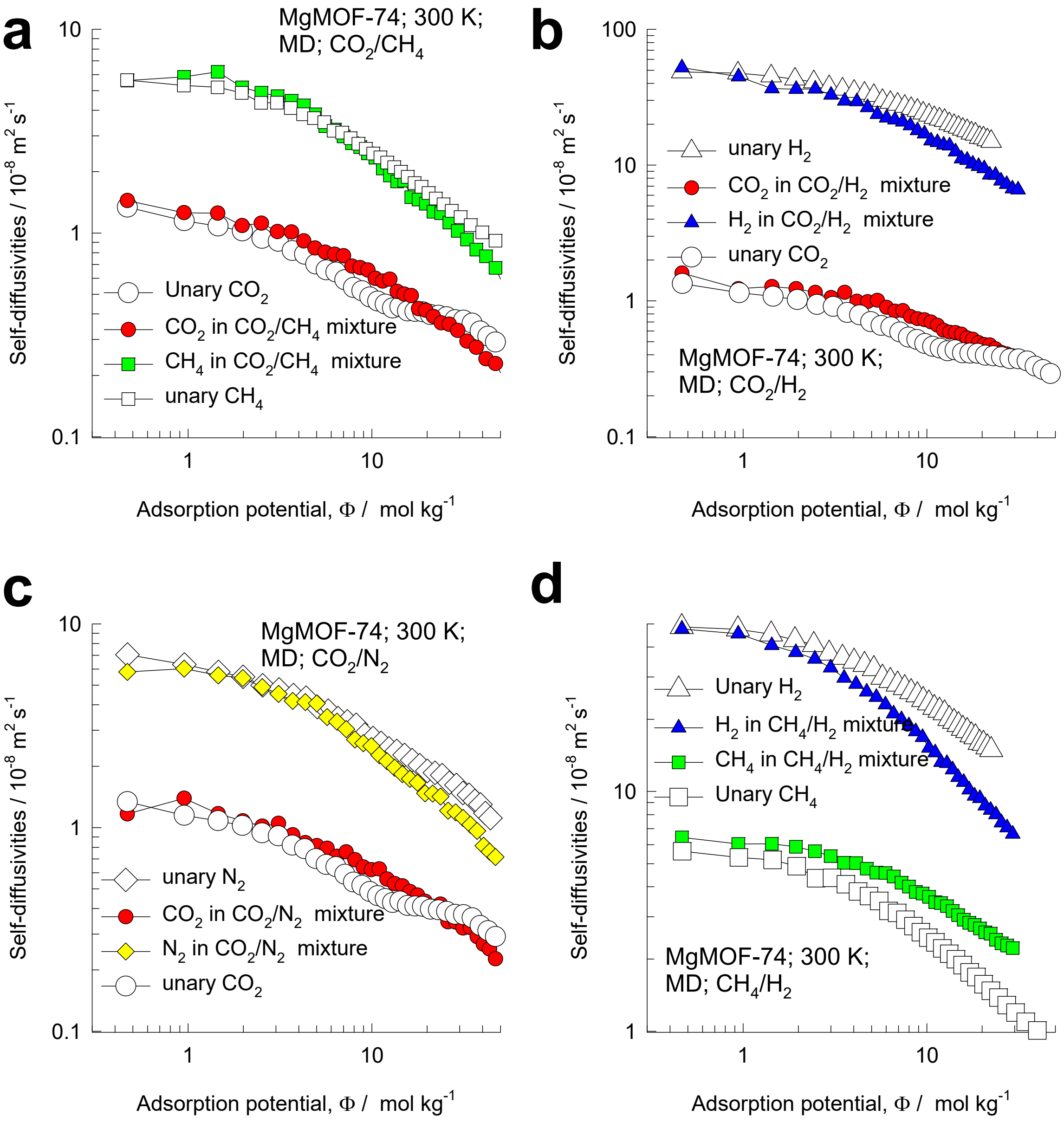

Figure S35. MD simulations of the self-diffusivities, $D_{i,self}$, of components in equimolar (q_1=q_2) binary (a) CO_2/CH_4, (b) CO_2/H_2, (c) CO_2/N_2, and (d) CH_4/H_2 mixtures in MgMOF-74 at 300 K, plotted as a function of the adsorption potential, $\Phi \equiv \pi A / RT$. Also plotted (using open symbols) are the corresponding values of the unary self-diffusivities.

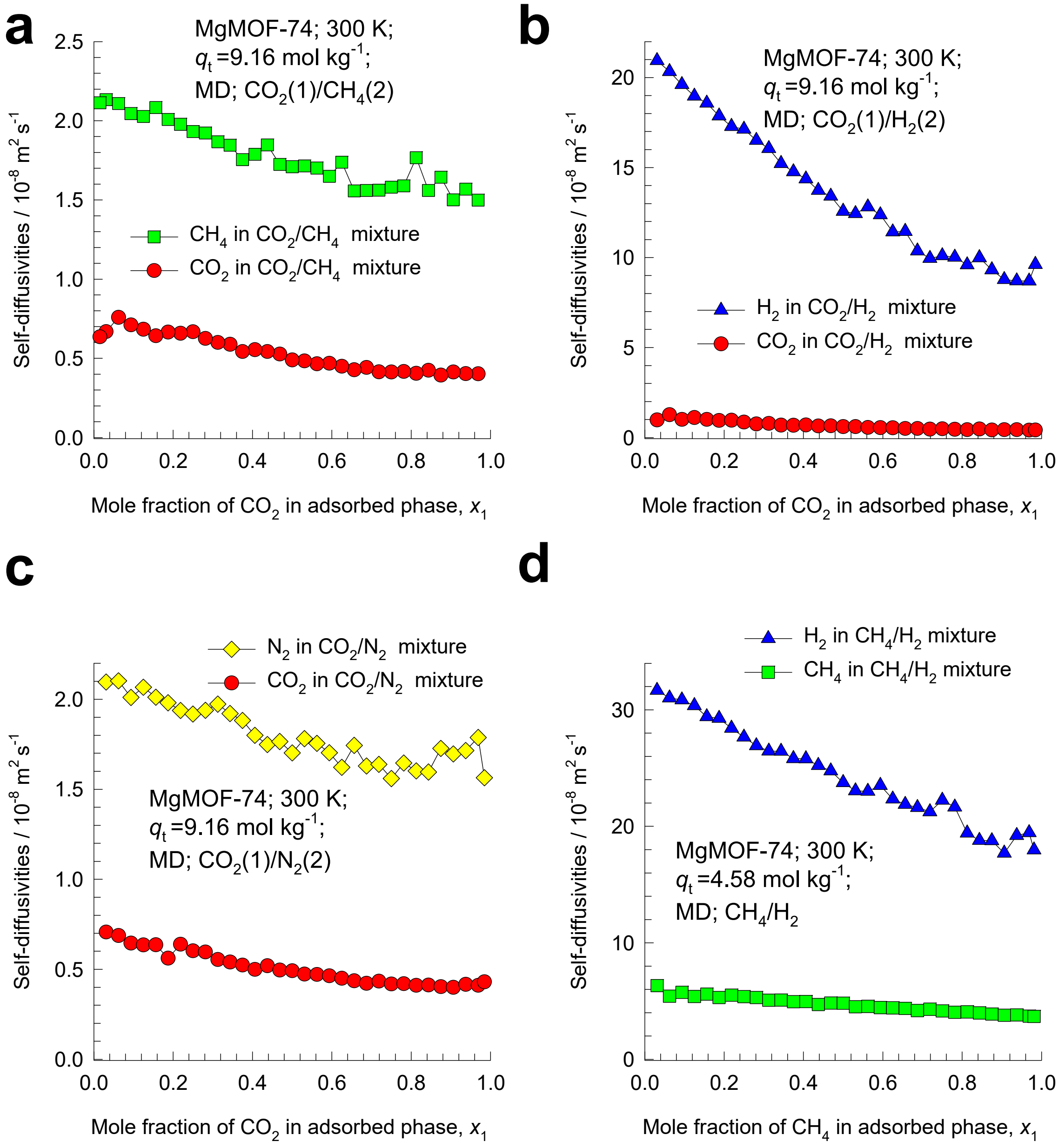

Figure S36. MD simulations of the self-diffusivities, $D_{i,self}$, of components in binary (a) CO_2/CH_4, (b) CO_2/H_2, (c) CO_2/N_2, and (d) CH_4/H_2 mixtures in MgMOF-74 at 300 K, plotted as a function of the adsorbed phase composition, x_1. The total loading $q_t = q_1 + q_2$ in these mixtures is held constant and the mole fraction of the adsorbed phase is varied.

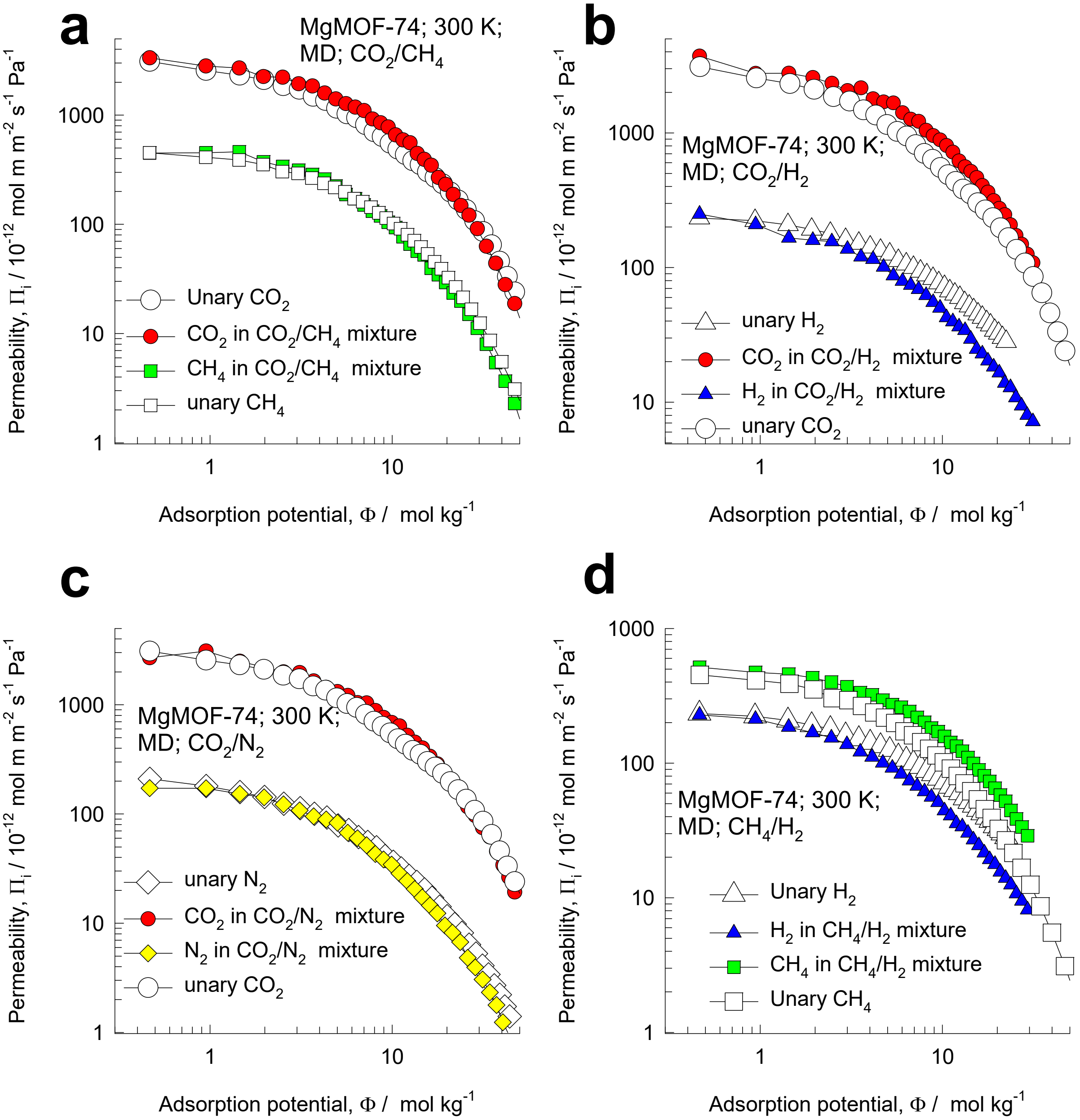

Figure S37. CBMC/MD simulations of the permeabilities, Π_i, of components in equimolar (q_1=q_2) binary (a) CO_2/CH_4, (b) CO_2/H_2, (c) CO_2/N_2, and (d) CH_4/H_2 mixtures in MgMOF-74 at 300 K, plotted as a function of the adsorption potential, $\Phi \equiv \pi A / RT$. Also plotted (using open symbols) are the corresponding values of the unary permeabilities.

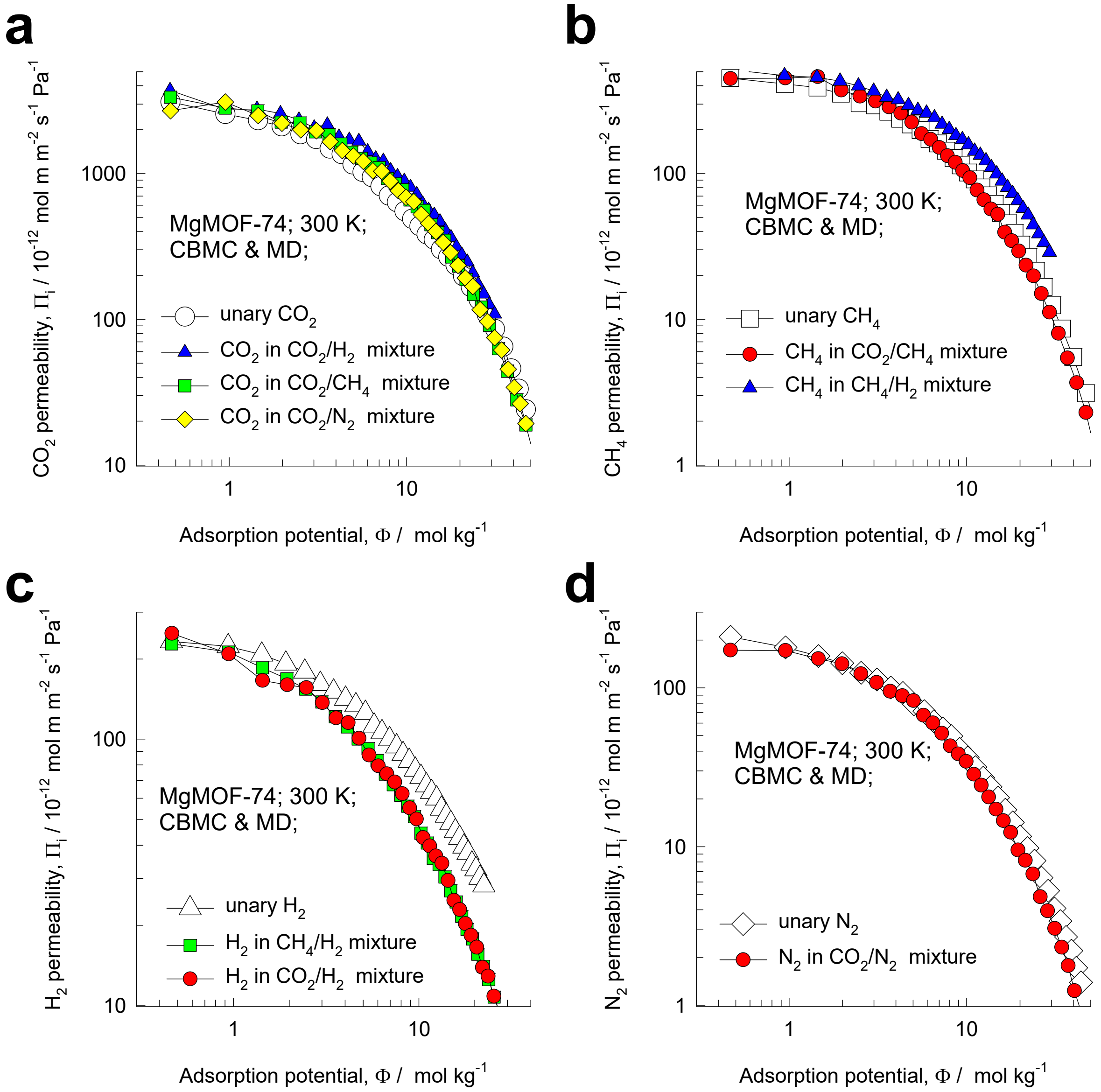

Figure S38. CBMC/MD simulations of the permeabilities, Π_i, of (a) CO_2, (b) CH_4, (c) H_2, and (d) N_2 in different equimolar (q_1=q_2) binary mixtures in MgMOF-74 at 300 K, plotted as a function of the adsorption potential, $\Phi \equiv \pi A / RT$. Also plotted (using open symbols) are the corresponding values of the unary permeabilities.

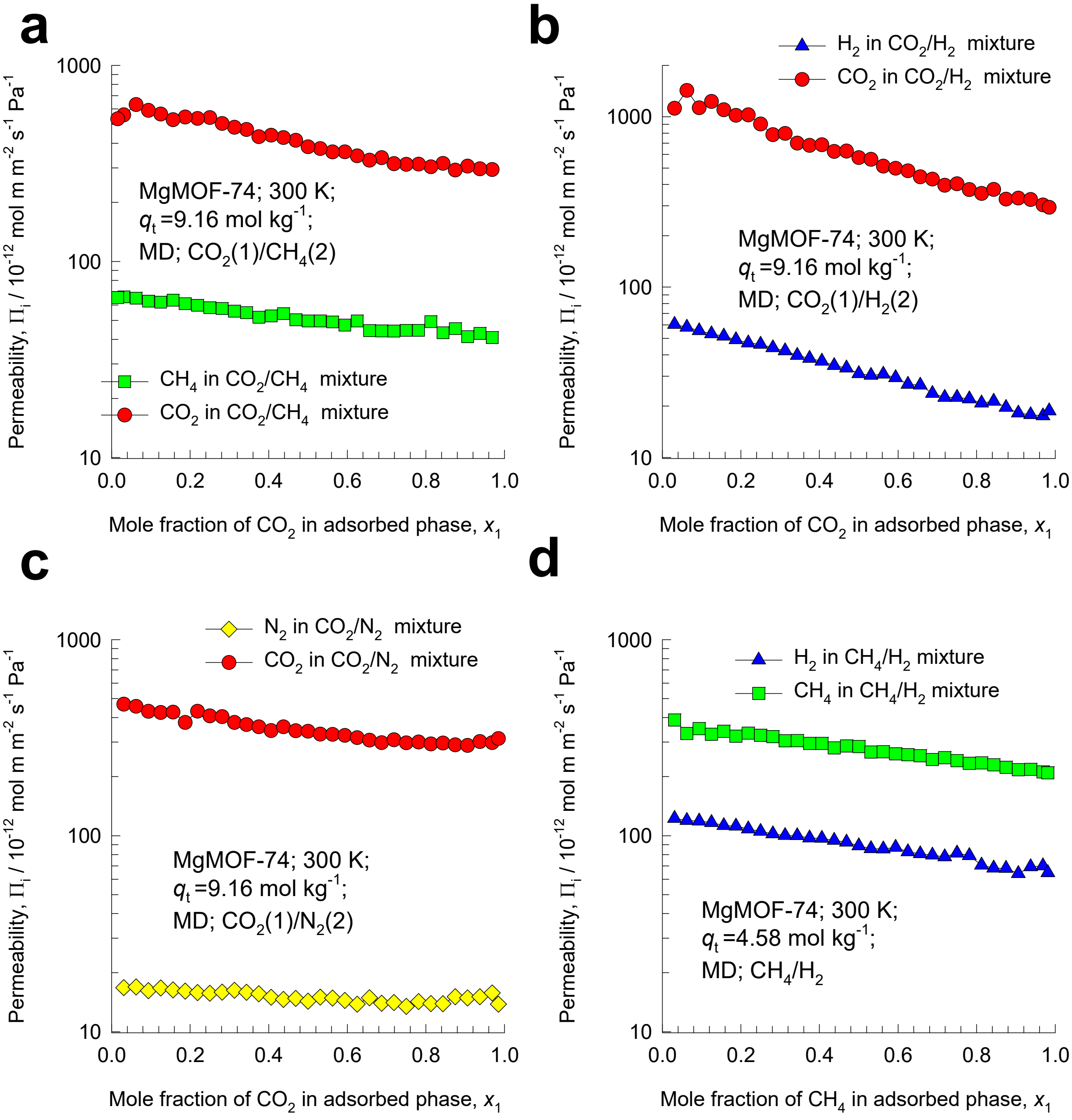

Figure S39. CBMC/MD simulations of the permeabilities, Π_i , of components in binary (a) CO_2/CH_4, (b) CO_2/H_2, (c) CO_2/N_2, and (d) CH_4/H_2 mixtures in MgMOF-74 at 300 K, plotted as a function of the adsorbed phase composition, x_1. The total loading $q_t = q_1 + q_2$ in these mixtures is held constant and the mole fraction of the adsorbed phase is varied.

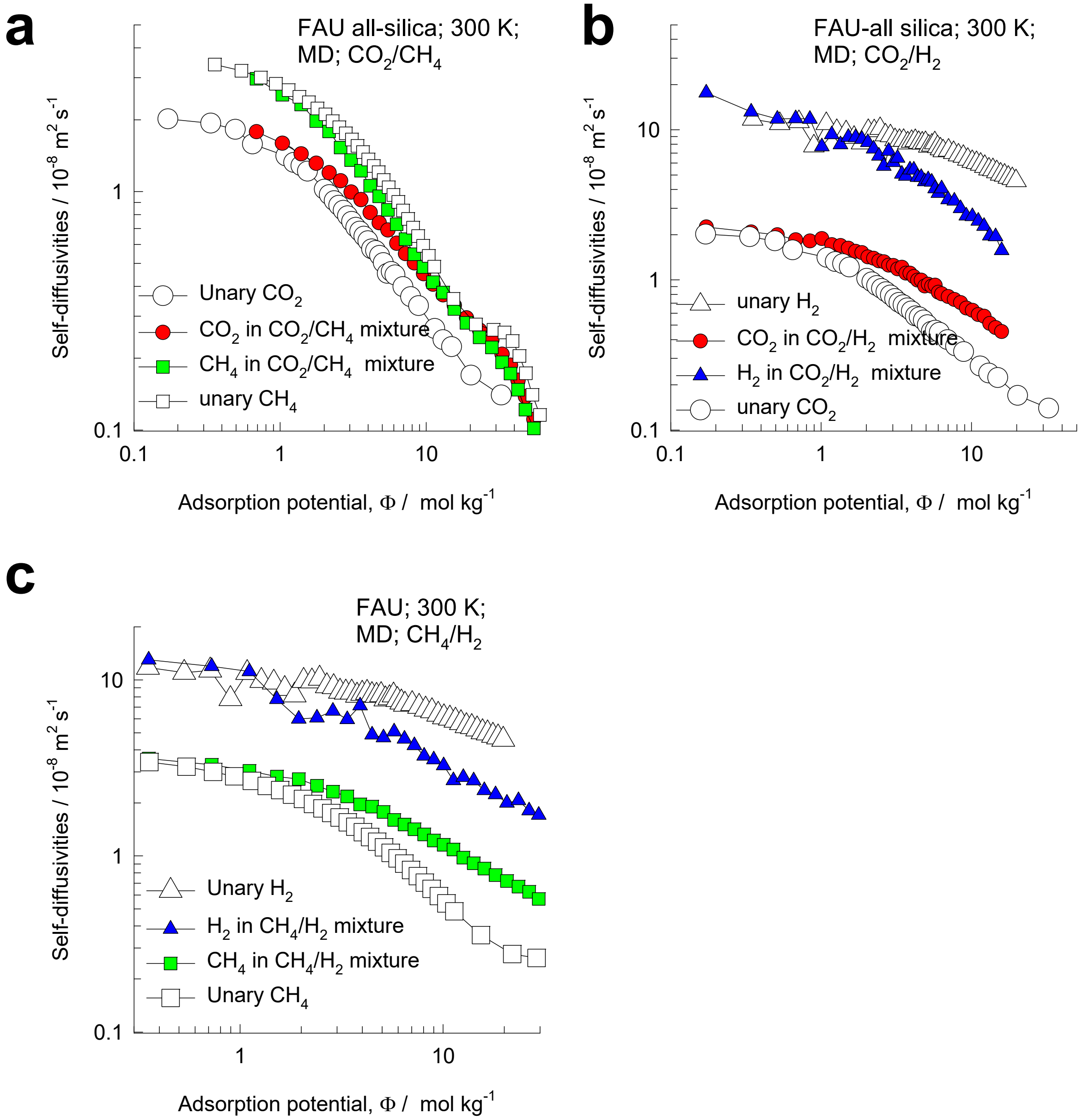

Figure S40. MD simulations of the self-diffusivities, $D_{i,self}$, of components in equimolar (q_1=q_2) binary (a) CO_2/CH_4, (b) CO_2/H_2, and(c) CH_4/H_2 mixtures in all-silica FAU zeolite at 300 K, plotted as a function of the adsorption potential, $\Phi \equiv \pi A / RT$. Also plotted (using open symbols) are the corresponding values of the unary self-diffusivities.

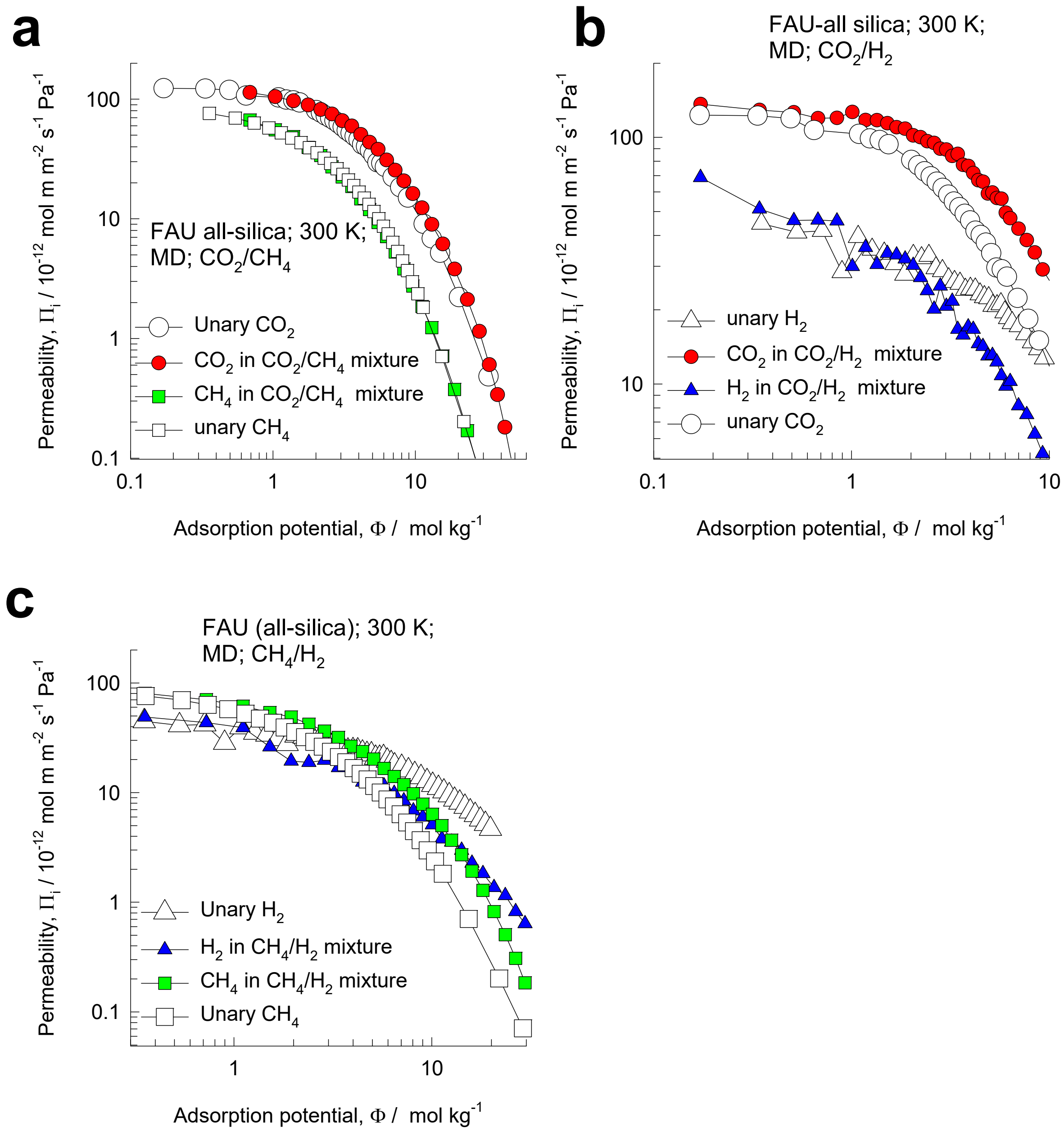

Figure S41. CBMC/MD simulations of the permeabilities, Π_i, of components in equimolar (q_1=q_2) binary (a) CO_2/CH_4, (b) CO_2/H_2, and(c) CH_4/H_2 mixtures in all-silica FAU zeolite at 300 K, plotted as a function of the adsorption potential, $\Phi \equiv \pi A / RT$. Also plotted (using open symbols) are the corresponding values of the unary permeabilities.

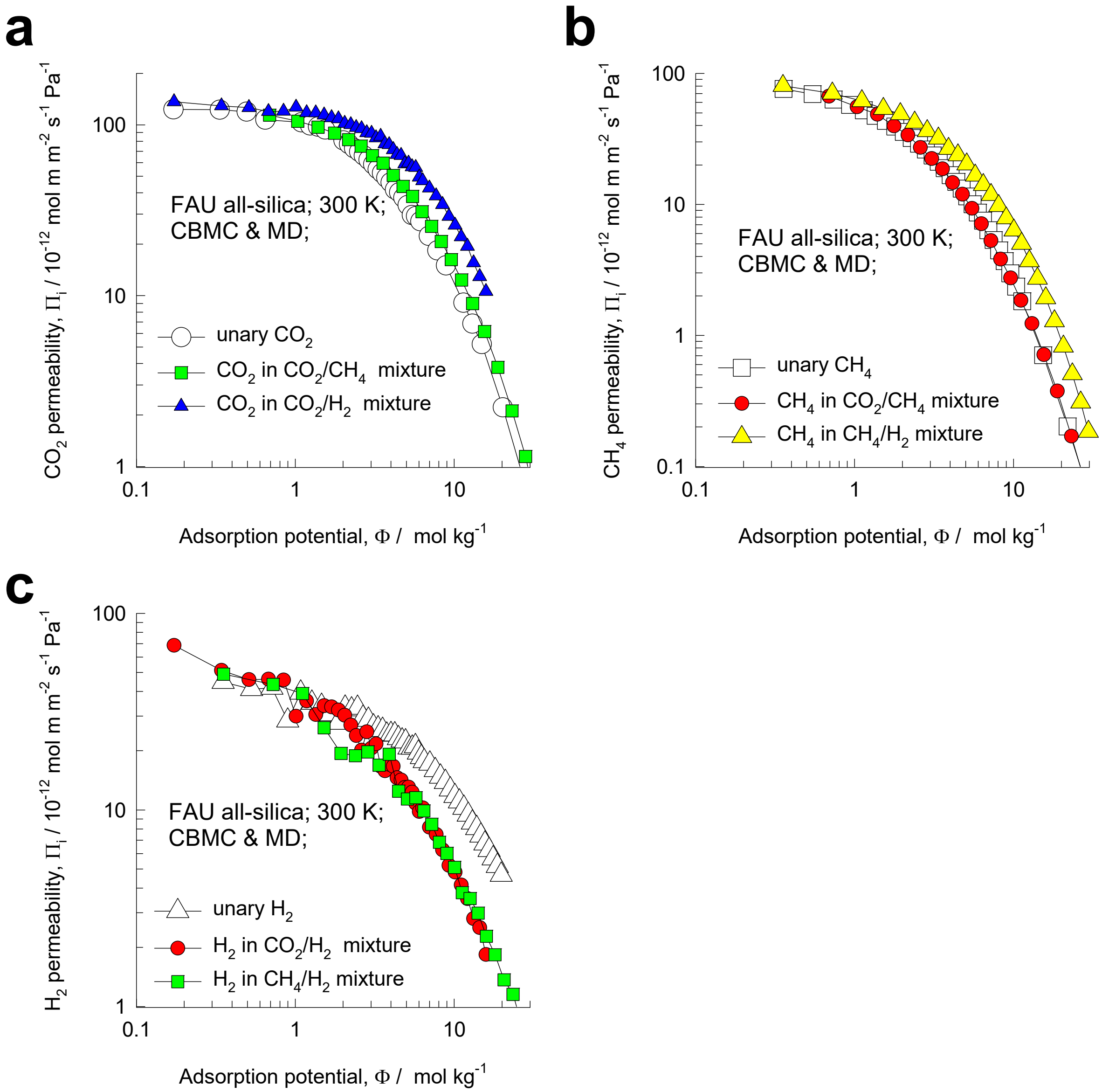

Figure S42. CBMC/MD simulations of the permeabilities, Π_i, of (a) CO$_2$, (b) CH$_4$, and (c) H$_2$ in different equimolar (q_1=q_2) binary mixtures all-silica FAU zeolite at 300 K, plotted as a function of the adsorption potential, $\Phi \equiv \pi A / RT$. Also plotted (using open symbols) are the corresponding values of the unary permeabilities.

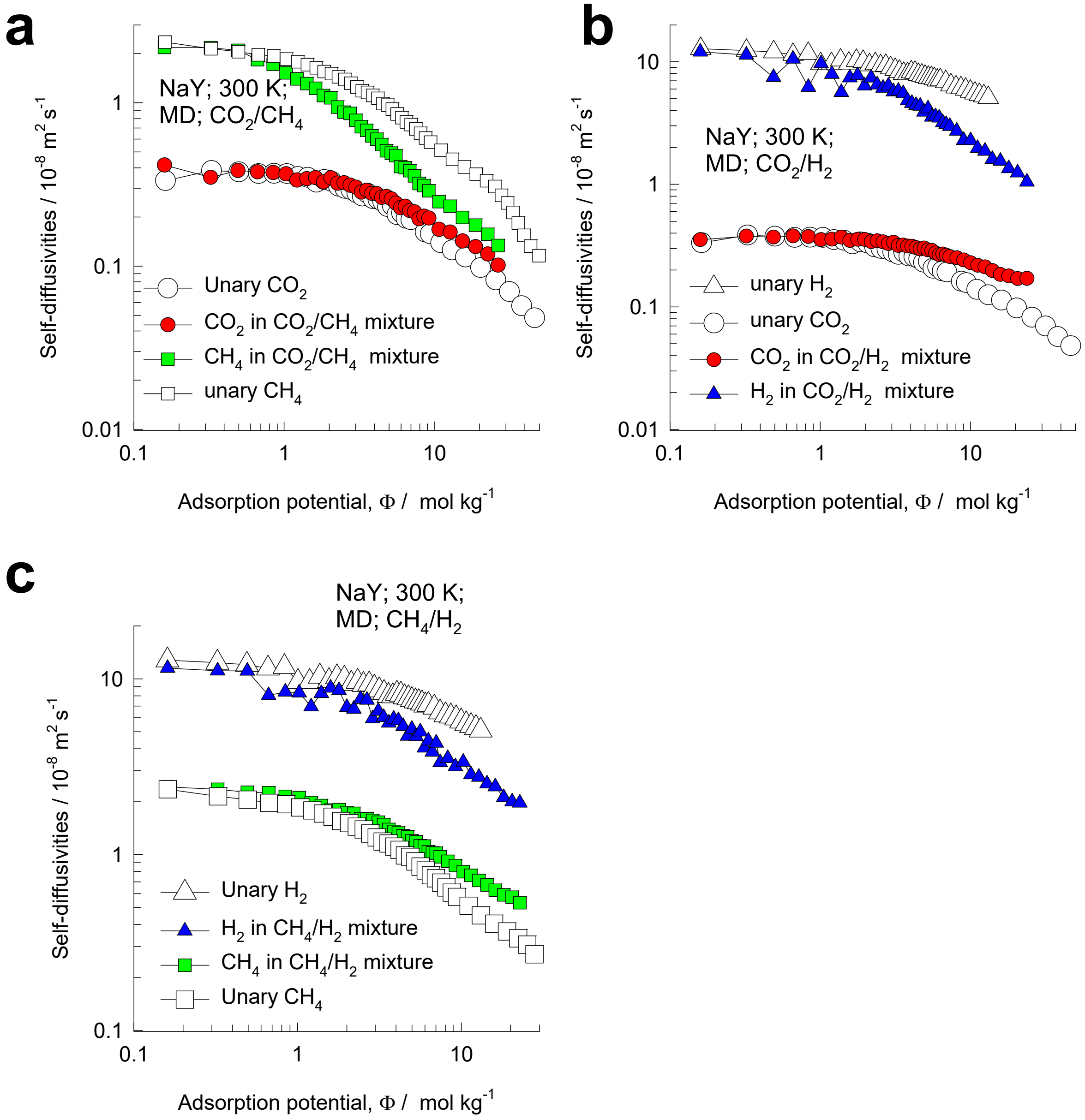

Figure S43. MD simulations of the self-diffusivities, $D_{i,self}$, of components in equimolar (q_1=q_2) binary (a) CO_2/CH_4, (b) CO_2/H_2, and(c) CH_4/H_2 mixtures in NaY zeolite at 300 K, plotted as a function of the adsorption potential, $\Phi \equiv \pi A / RT$. Also plotted (using open symbols) are the corresponding values of the unary self-diffusivities.

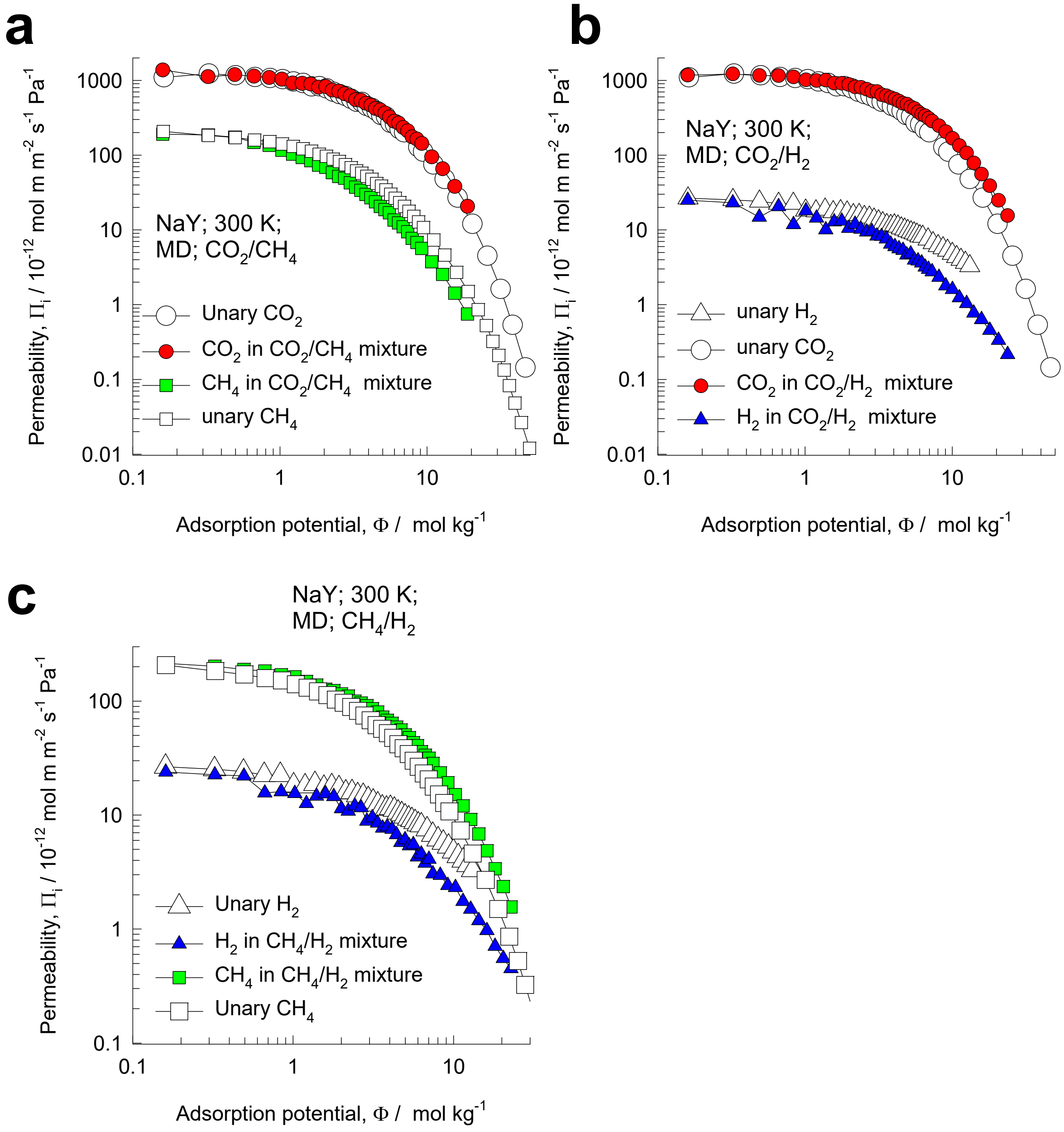

Figure S44. CBMC/MD simulations of the permeabilities, Π_i, of components in equimolar (q_1=q_2) binary (a) CO_2/CH_4, (b) CO_2/H_2, and(c) CH_4/H_2 mixtures mixtures in NaY zeolite at 300 K, plotted as a function of the adsorption potential, $\Phi \equiv \pi A / RT$. Also plotted (using open symbols) are the corresponding values of the unary permeabilities.

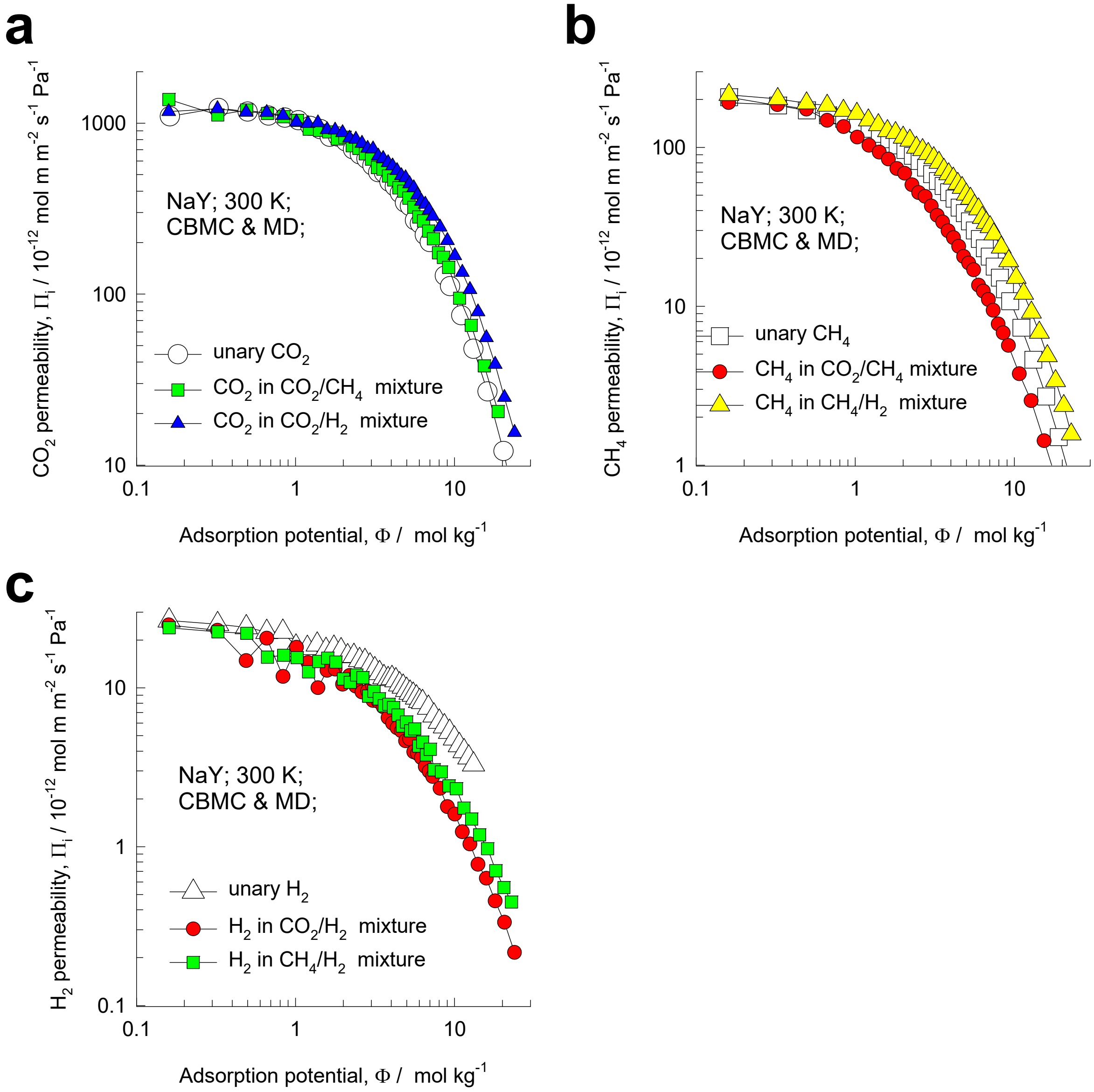

Figure S45. CBMC/MD simulations of the permeabilities, Π_i, of (a) CO$_2$, (b) CH$_4$, and (c) H$_2$ in different equimolar (q_1=q_2) binary mixtures NaY zeolite at 300 K, plotted as a function of the adsorption potential, $\Phi \equiv \pi A / RT$. Also plotted (using open symbols) are the corresponding values of the unary permeabilities.

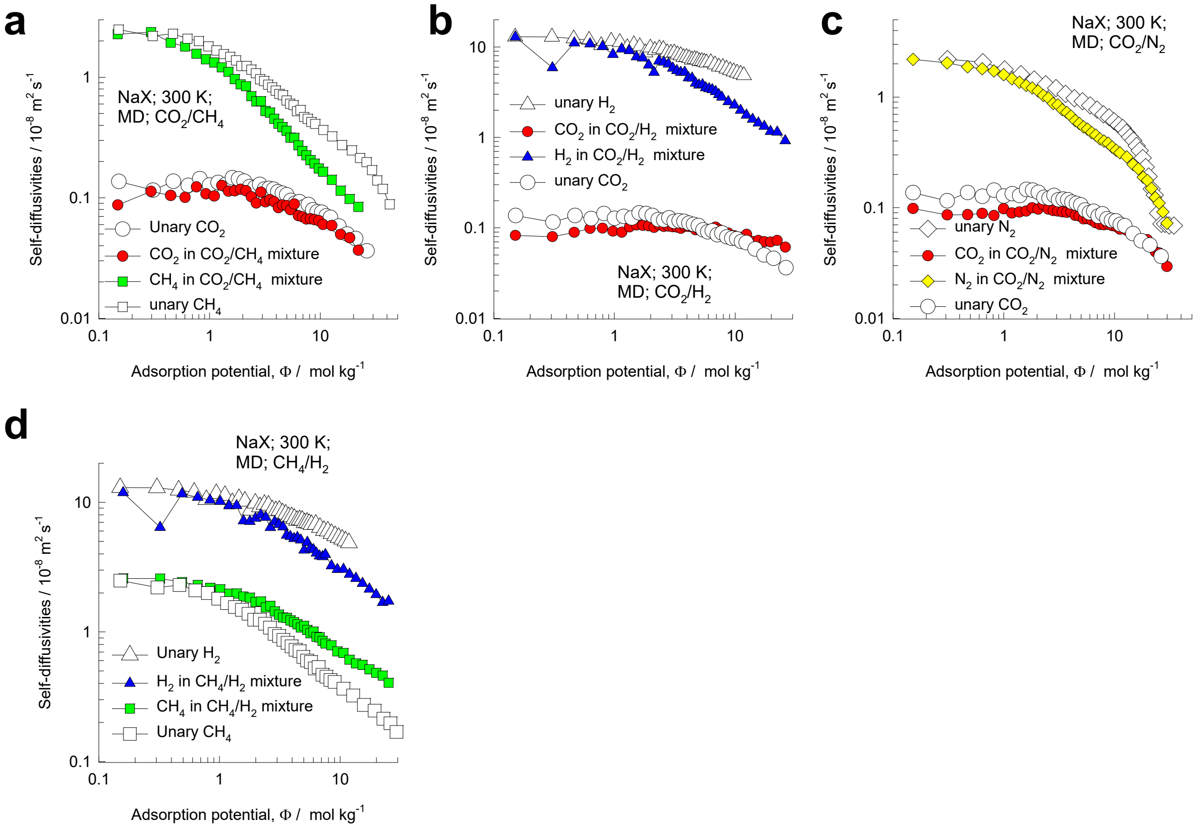

Figure S46. MD simulations of the self-diffusivities, $D_{i,self}$, of components in equimolar (q_1=q_2) binary (a) CO_2/CH_4, (b) CO_2/H_2, (c) CO_2/N_2 , and (d) CH_4/H_2 mixtures in NaX zeolite at 300 K, plotted as a function of the adsorption potential, $\Phi \equiv \pi A / RT$. Also plotted (using open symbols) are the corresponding values of the unary self-diffusivities.

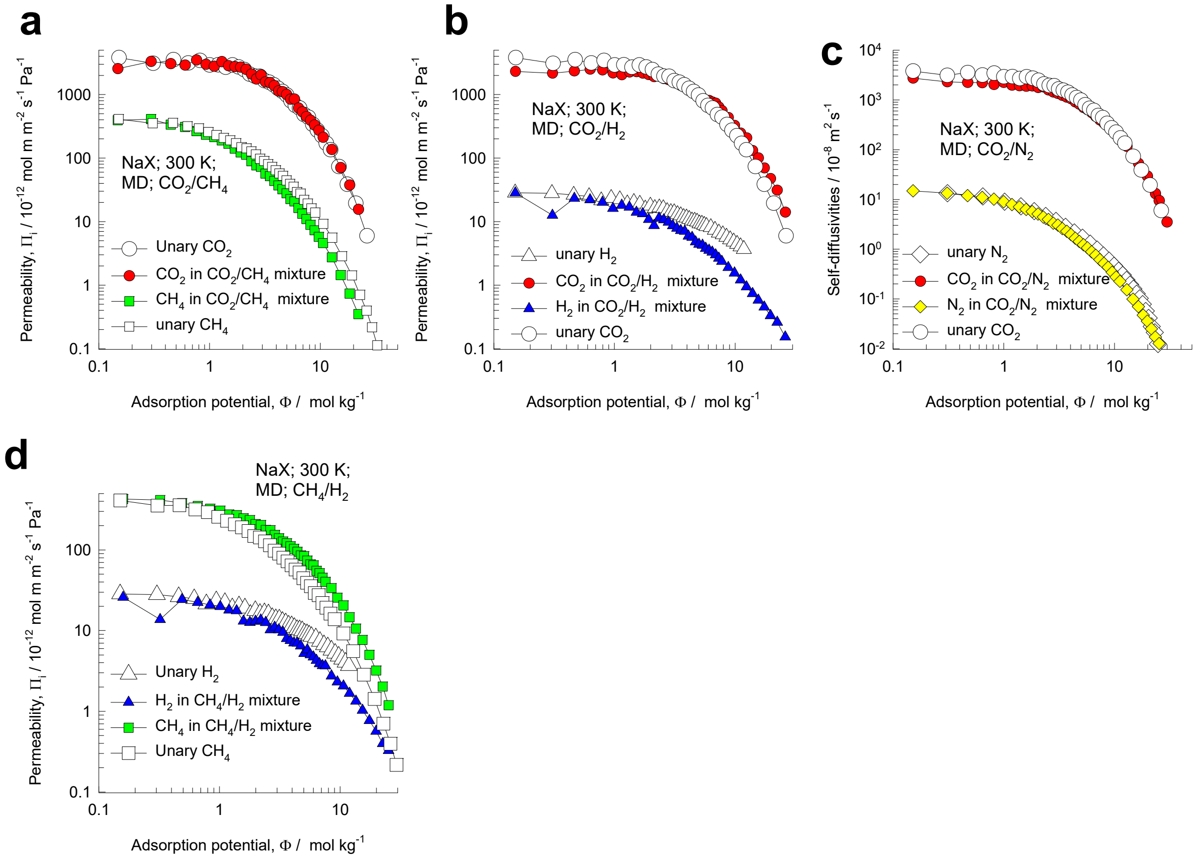

Figure S47. CBMC/MD simulations of the permeabilities, Π_i, of components in equimolar (q_1=q_2) binary (a) CO_2/CH_4, (b) CO_2/H_2, (c) CO_2/N_2 , and (d) CH_4/H_2 mixtures in NaX zeolite at 300 K, plotted as a function of the adsorption potential, $\Phi \equiv \pi A / RT$. Also plotted (using open symbols) are the corresponding values of the unary permeabilities.

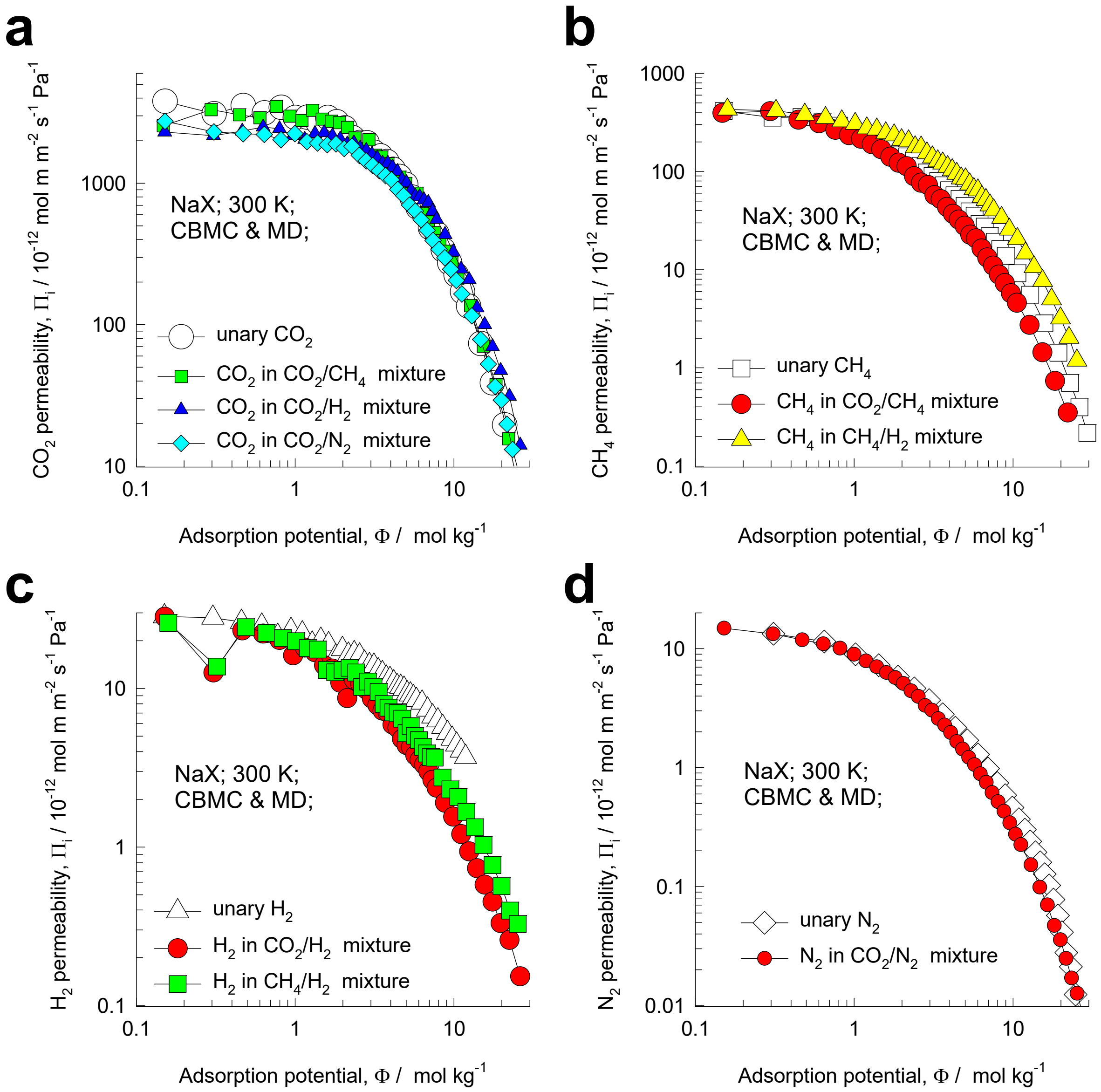

Figure S48. CBMC/MD simulations of the permeabilities, Π_i, of (a) CO_2, (b) CH_4, (c) H_2, and (d) N_2 in different equimolar ($q_1=q_2$) binary mixtures NaX zeolite at 300 K, plotted as a function of the adsorption potential, $\Phi \equiv \pi A / RT$. Also plotted (using open symbols) are the corresponding values of the unary permeabilities.

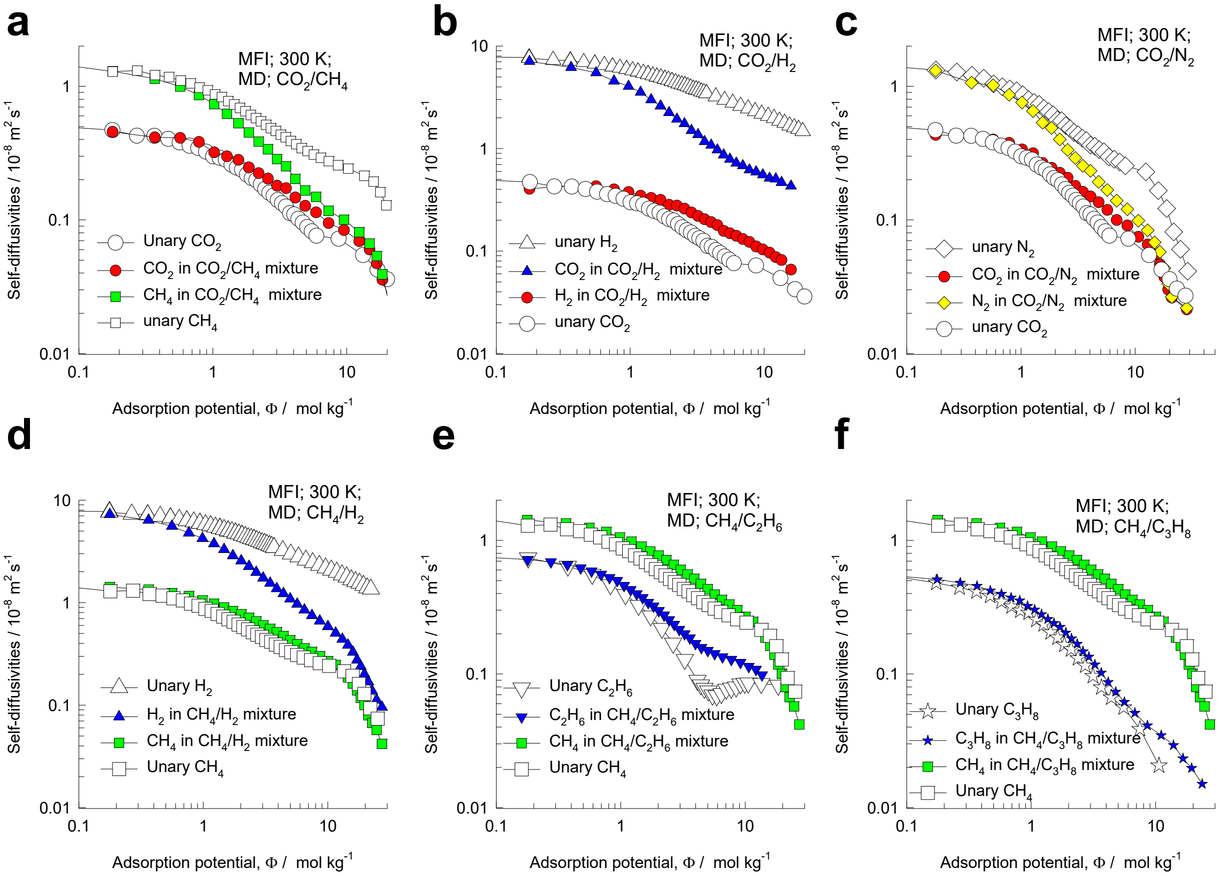

Figure S49. MD simulations of the self-diffusivities, $D_{i,self}$, of components in equimolar (q_1=q_2) binary (a) CO_2/CH_4, (b) CO_2/H_2, (c) CO_2/N_2, (d) CH_4/H_2 (e) CH_4/C_2H_6, and (f) CH_4/C_3H_8 mixtures in MFI zeolite at 300 K, plotted as a function of the adsorption potential, $\Phi \equiv \pi A / RT$. Also plotted (using open symbols) are the corresponding values of the unary self-diffusivities.

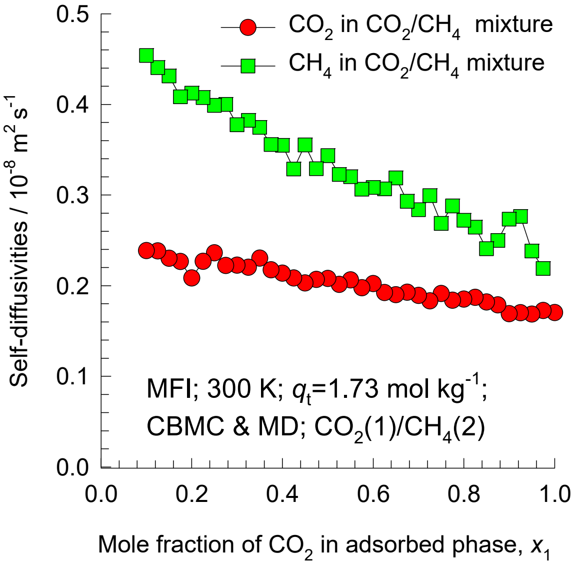

Figure S50. MD simulations of the self-diffusivities, $D_{i,self}$, of components in binary CO_2/CH_4 mixtures in MFI at 300 K, plotted as a function of the adsorbed phase composition, x_1. The total loading $q_t = q_1 + q_2$ in this mixture is held constant and the mole fraction of the adsorbed phase is varied.

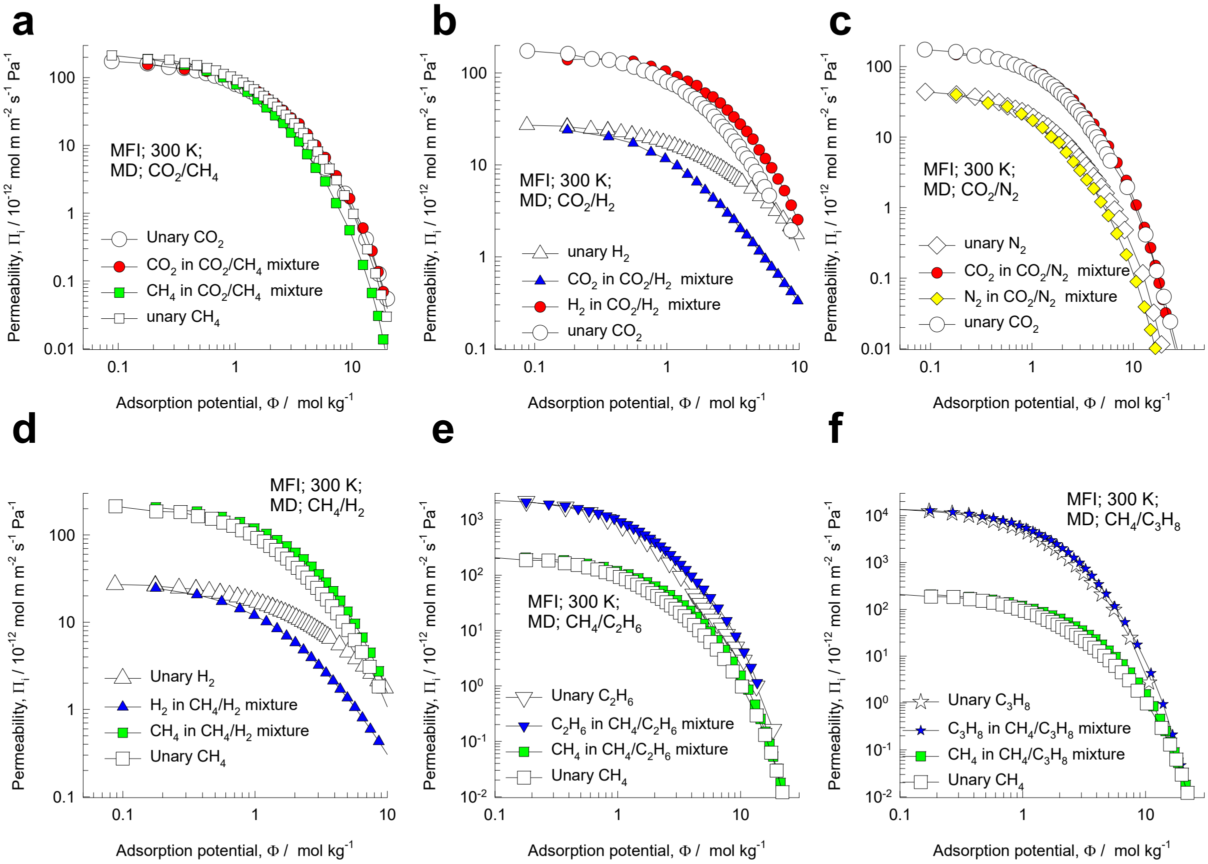

Figure S51. CBMC/MD simulations of the permeabilities, Π_i, of components in equimolar (q_1=q_2) binary (a) CO_2/CH_4, (b) CO_2/H_2, (c) CO_2/N_2, (d) CH_4/H_2 (e) CH_4/C_2H_6, and (f) CH_4/C_3H_8 mixtures in MFI zeolite at 300 K, plotted as a function of the adsorption potential, $\Phi \equiv \pi A / RT$. Also plotted (using open symbols) are the corresponding values of the unary permeabilities.

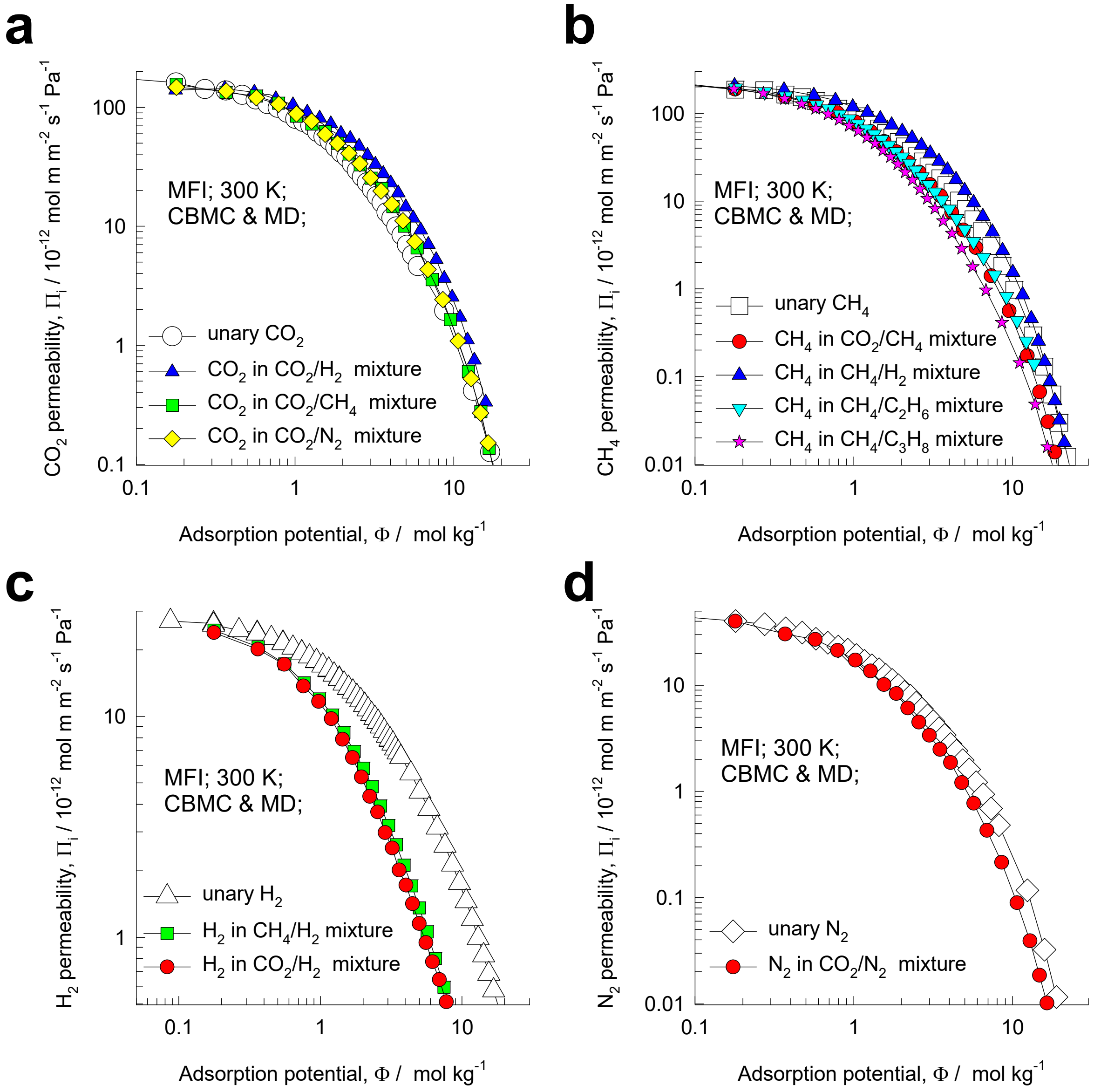

Figure S52. CBMC/MD simulations of the permeabilities, Π_i, of (a) CO$_2$, (b) CH$_4$, (c) H$_2$, and (d) N$_2$ in different equimolar (q_1=q_2) binary mixtures in MFI zeolite at 300 K, plotted as a function of the adsorption potential, $\Phi \equiv \pi A / RT$. Also plotted (using open symbols) are the corresponding values of the unary permeabilities.

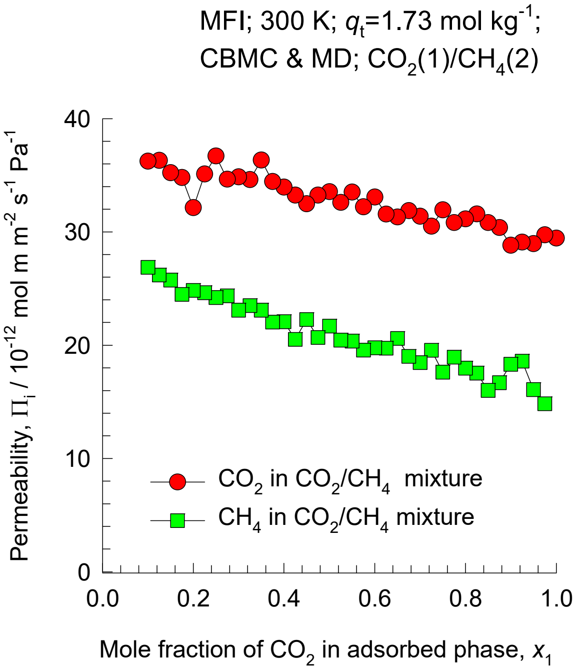

Figure S53. CBMC/MD simulations of the permeabilities, Π_i, of components in binary CO_2/CH_4 mixtures in MFI at 300 K, plotted as a function of the adsorbed phase composition, x_1. The total loading $q_t = q_1 + q_2$ in these mixtures is held constant and the mole fraction of the adsorbed phase is varied.

10 Comparison of Membrane Permeation Selectivities

10.1 CBMC simulation campaigns

CBMC simulation campaigns for adsorption of three different binary mixtures (CO_2/CH_4, CO_2/N_2, CO_2/H_2) was undertaken in all-silica zeolites (CHA, DDR, FAU, MFI), cation-exchanged zeolites (NaY, NaX), MgMOF-74, BTP-COF and ZIF-8 at a temperature $T = 300$ K. In the campaigns, the bulk fluid phase composition held constant at $\frac{f_1}{f_1+f_2} \equiv y_1$, and the bulk fluid phase fugacity $f_t = f_1 + f_2$ was varied over a wide range from the Henry regime of adsorption, $f_t \to 0$; $\Phi \equiv \frac{\pi A}{RT} \to 0$, to pore saturation conditions, typically $\Phi \equiv \frac{\pi A}{RT} > 50$.

10.2 Adsorption selectivity, S_{ads}

For binary mixtures consisting of components 1, and 2, the adsorption selectivity, S_{ads}, is defined by

$$S_{ads} = \frac{q_1/q_2}{f_1/f_2} = \frac{q_1/q_2}{y_1/y_2} \tag{S48}$$

where q_1 and q_2 are the molar loadings of the components 1, and 2 in the adsorbed phase in equilibrium with a bulk gas phase mixture with mole fractions $y_1 = \frac{f_1}{f_1+f_2}; y_2 = \frac{f_2}{f_1+f_2}$. In view of eqs (S12), and (S13), we may re-write eq (S14) as the ratio of the sorption pressures

$$S_{ads} = \frac{q_1/q_2}{f_1/f_2} = \frac{x_1/f_1}{x_2/f_2} = \frac{P_2^0}{P_1^0} \tag{S49}$$

Applying the restriction specified by eq (S8), it follows that S_{ads} is uniquely determined by the adsorption potential $\Phi \equiv \frac{\pi A}{RT}$.

To demonstrate the Figure S54a shows CBMC simulation data of the adsorption selectivity, S_{ads}, for CO_2(1)/CH_4(2) mixtures in CHA zeolite at 300 K; the bulk gas phase mole fractions are maintained at $y_1 = 0.5$, or $y_1 = 0.15$ and S_{ads} is plotted as a function of the bulk gas mixture fugacity, $f_t = f_1 + f_2$. Figure S54b shows CBMC simulation data of adsorption selectivity, S_{ads}, for CO_2(1)/CH_4(2) mixtures in CHA zeolite at 300 K; the total bulk gas mixture fugacity is held constant, $f_t = f_1 + f_2 = 10^6$ Pa, and S_{ads} is plotted as a function of the bulk gas mixture of CO_2(1), y_1. In Figure S54c, all three data sets are plotted as function of the adsorption potential $\Phi \equiv \frac{\pi A}{RT}$. It is noteworthy, that the CBMC simulated data for S_{ads} is uniquely determined by $\Phi \equiv \frac{\pi A}{RT}$, as anticipated by the IAST.

Also determined from the CBMC simulations is the separation potential, Δq,

$$\Delta q = q_1 \frac{y_2}{y_1} - q_2 \tag{S50}$$

The separation potential represents that maximum amount of component 2 (less strongly adsorbed), that can be recovered during the adsorption cycle of fixed bed separations.[63-65]

10.3 Permeation selectivity, S_{perm}

The membrane permeation selectivity, S_{perm}, is defined as the ratio of the permeabilities

$$S_{perm} = \frac{\Pi_1}{\Pi_2} \tag{S51}$$

In view of eq (S46), we write

$$S_{perm} = \frac{D_{1,self} q_1 / f_1}{D_{2,self} q_2 / f_2} = S_{ads} \times S_{diff} \tag{S52}$$

Comparison of Membrane Permeation Selectivities

In eq (S52), the diffusion selectivity $S_{diff} = \frac{D_{1,self}}{D_{2,self}}$ for each binary mixture is determined from the MD simulations reported in Chapter 9, Permeation of Binary Mixtures in Microporous Materials for the same binary mixture, determined at the same adsorption potential $\Phi \equiv \frac{\pi A}{RT}$.

10.4 List of Figures for Comparison of Membrane Permeation Selectivities

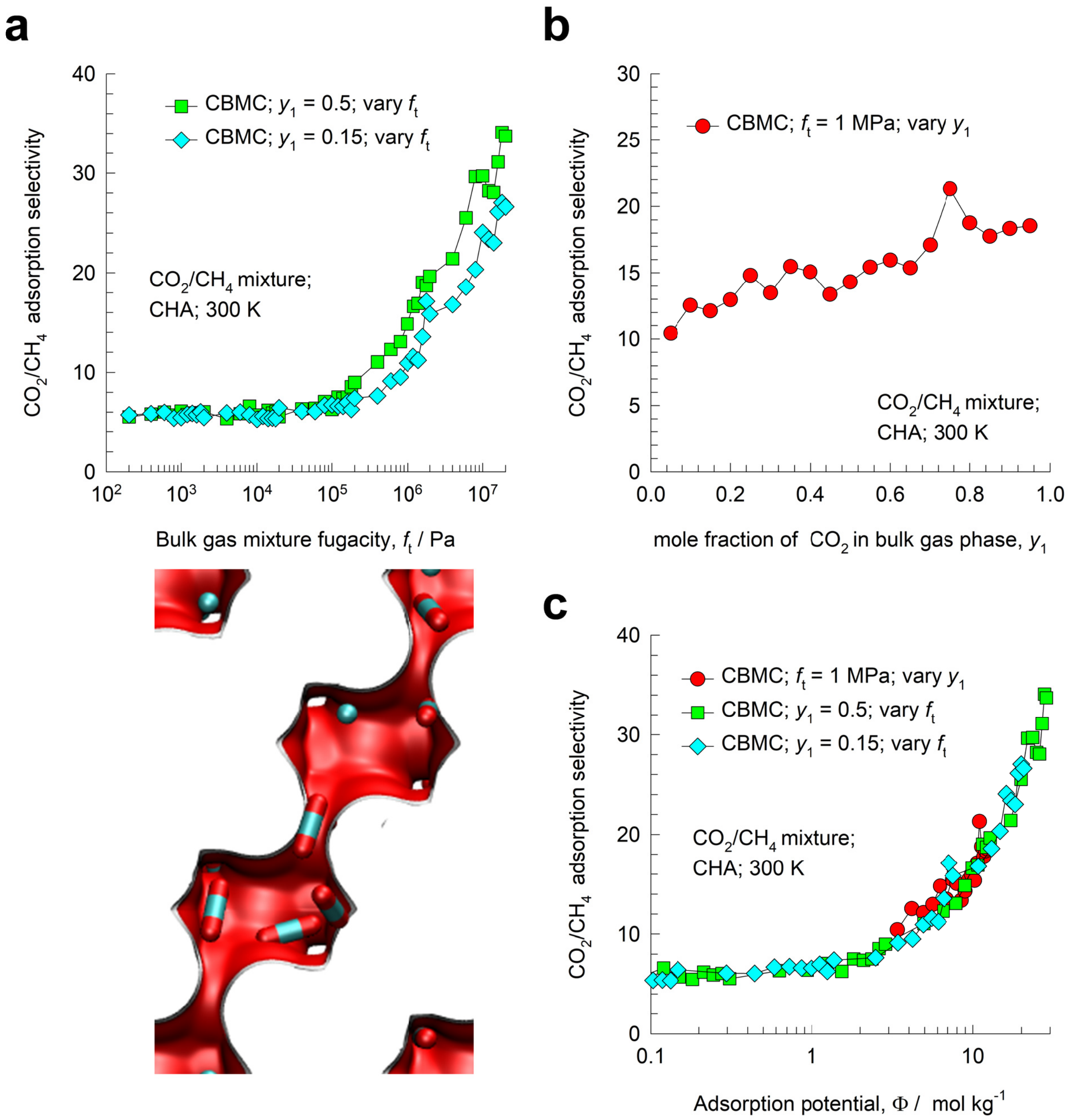

Figure S54. (a, b, c) CBMC simulations of the adsorption selectivity, S_{ads}, for CO2(1)/CH4(2) mixtures in CHA zeolite at 300 K. In (a) the bulk gas phase mole fractions are maintained at $y_1 = 0.5$, or $y_1 = 0.15$ and S_{ads} is plotted as a function of the bulk gas mixture fugacity, $f_t = f_1 + f_2$. In (b) the total bulk gas mixture fugacity is held constant, $f_t = f_1 + f_2 = 10^6$ Pa, and S_{ads} is plotted as a function of the bulk gas mole fraction of CO$_2$(1), y_1. In (c) all three sets of data are plotted as function of the adsorption potential $\Phi \equiv \frac{\pi A}{RT}$.

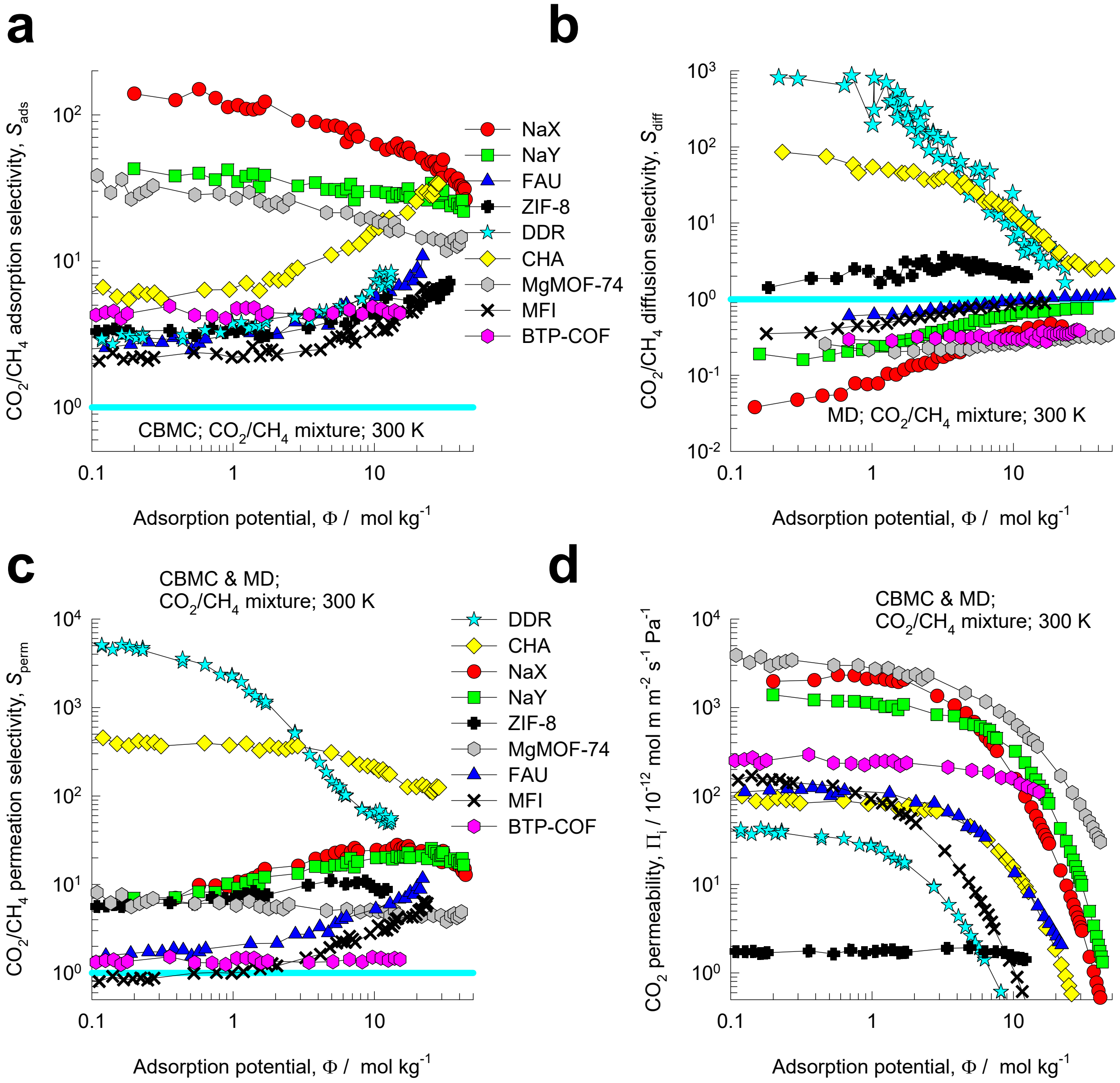

Figure S55. Comparison of (a) S_{ads}, adsorption selectivity, (b) diffusion selectivity, $S_{diff} = D_{1,self} / D_{2,self}$, (c) permeation selectivity, $S_{perm} = \Pi_1 / \Pi_2$, and (d) CO$_2$ permeability, Π_1, for CO$_2$(1)/CH$_4$(2) mixtures with $\frac{f_1}{f_1+f_2} \equiv y_1 = 0.5$ in all-silica zeolites (CHA, DDR, FAU, MFI), cation-exchanged zeolites (NaY, NaX), MgMOF-74, BTP-COF and ZIF-8.

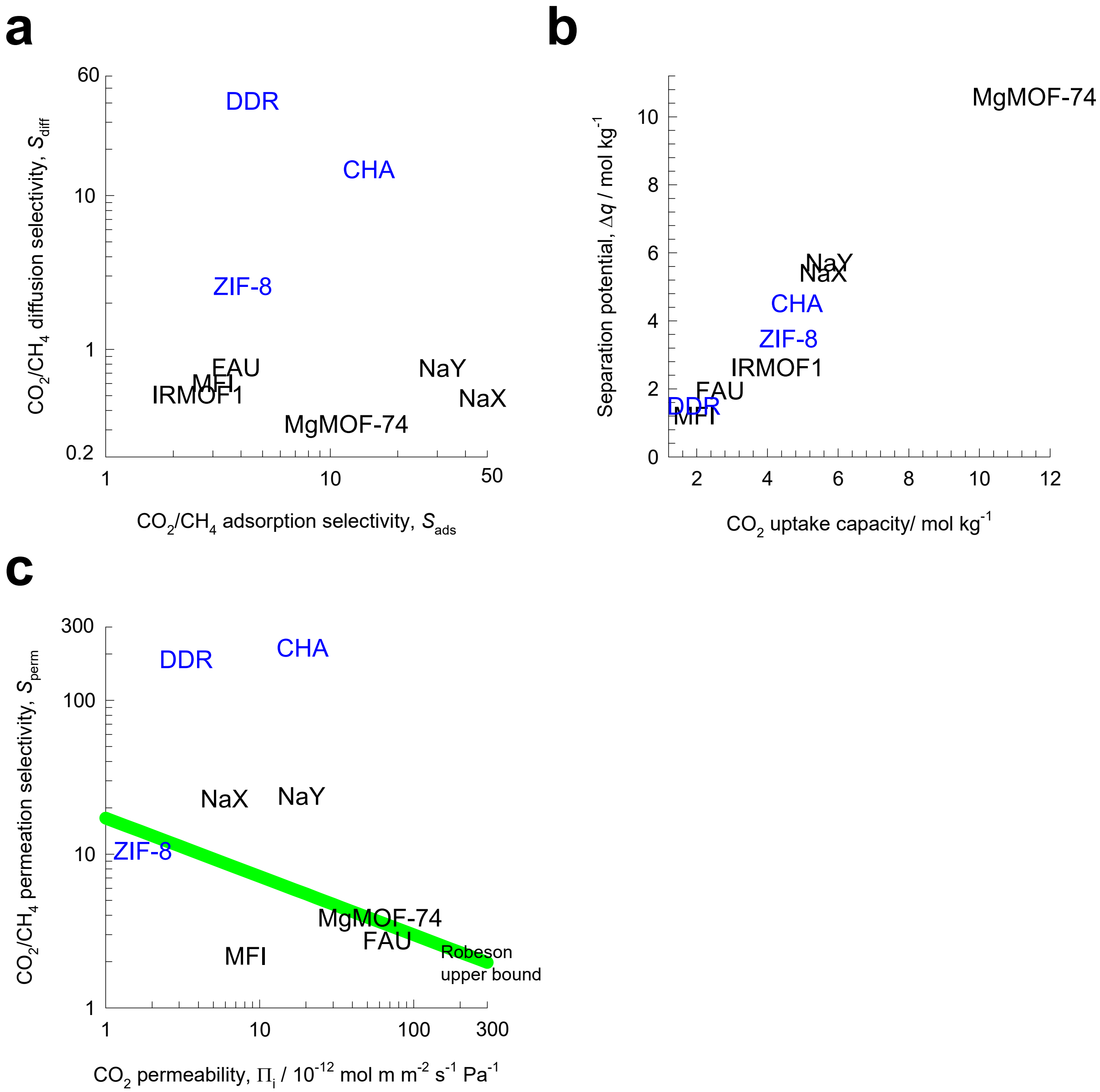

Figure S56. (a) Plot of S_{ads} vs $S_{diff} = D_{1,self} / D_{2,self}$, (b) Plot of Δq vs CO$_2$ uptake capacity, and (c) Plot of $S_{perm} = \Pi_1 / \Pi_2$ vs CO$_2$ permeability, Π_1, for CO$_2$(1)/CH$_4$(2) mixtures with $\frac{f_1}{f_1 + f_2} \equiv y_1 = 0.5$ in all-silica zeolites (CHA, DDR, FAU, MFI), cation-exchanged zeolites (NaY, NaX), MgMOF-74, and ZIF-8 at $f_t = f_1 + f_2 = 1$ MPa and temperature $T = 300$ K.

Comparison of Membrane Permeation Selectivities

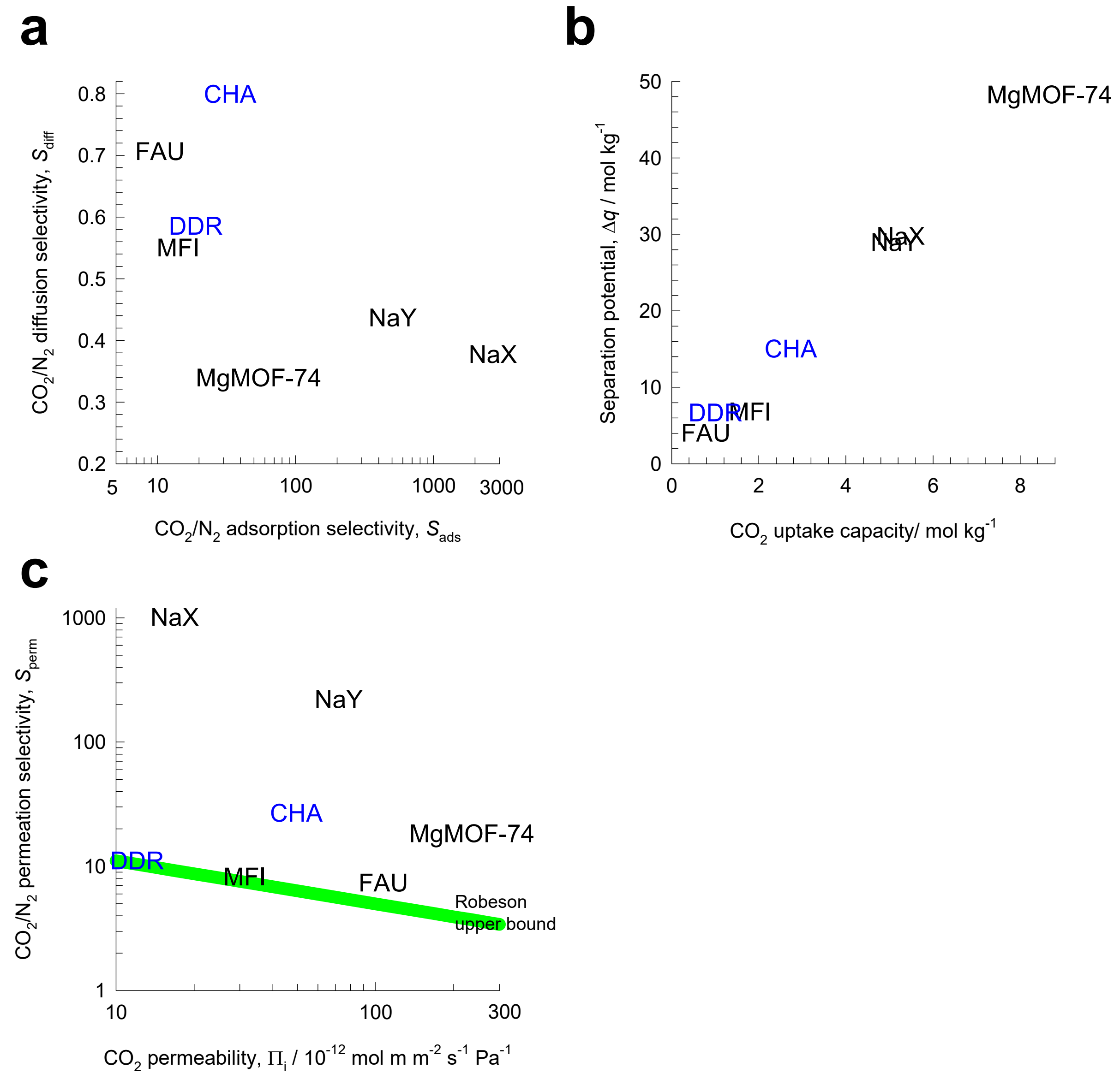

Figure S57. (a) Plot of S_{ads} vs $S_{diff} = D_{1,self} / D_{2,self}$, (b) Plot of Δq vs CO_2 uptake capacity, and (c) Plot of $S_{perm} = \Pi_1 / \Pi_2$ vs CO_2 permeability, Π_1, for $CO_2(1)/N_2(2)$ mixtures with $\frac{f_1}{f_1 + f_2} \equiv y_1 = 0.15 = 1 - y_2$ in all-silica zeolites (CHA, DDR, FAU, MFI), cation-exchanged zeolites (NaY, NaX), MgMOF-74, and ZIF-8 at $f_t = f_1 + f_2 = 1$ MPa and temperature $T = 300$ K.

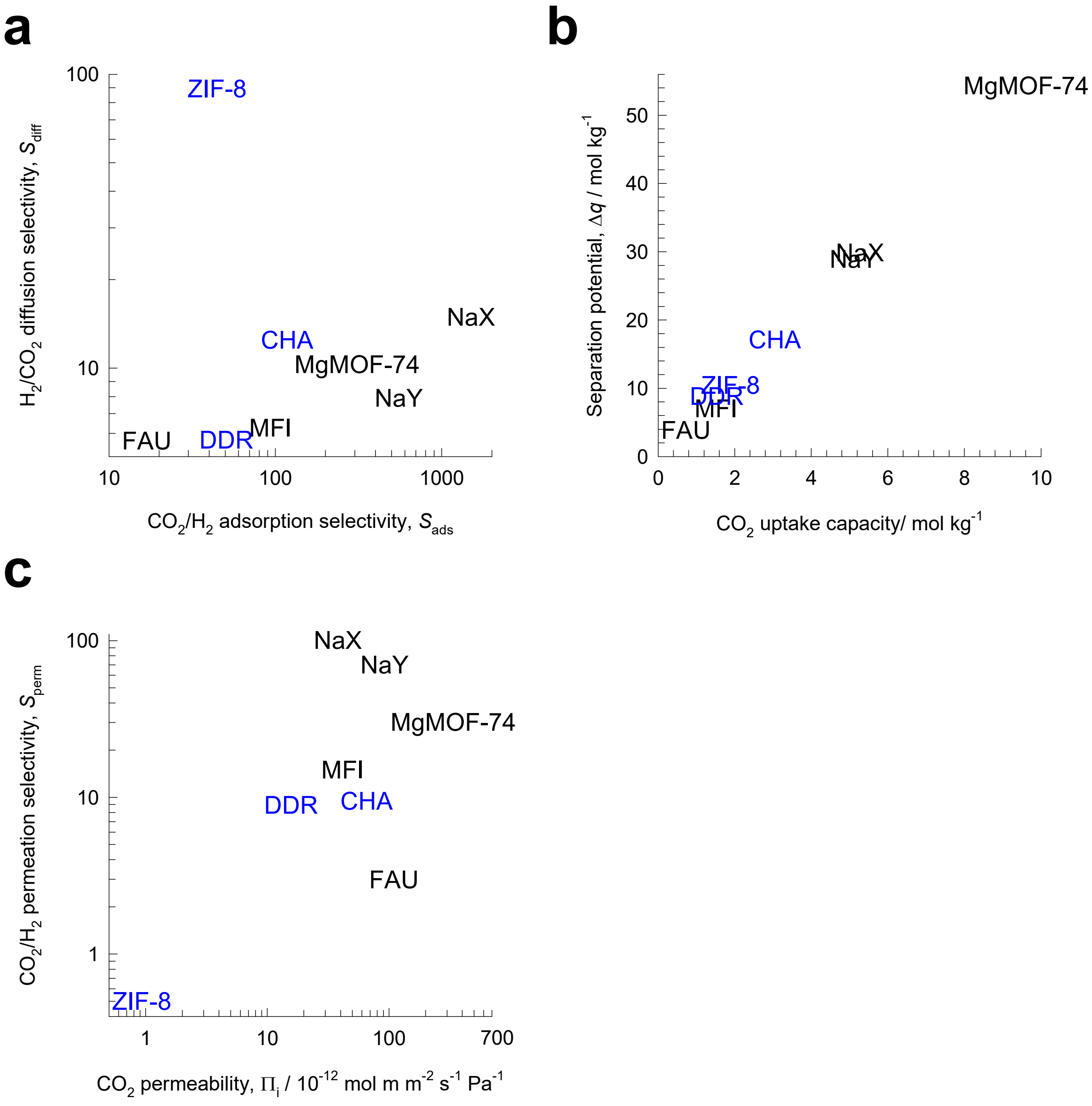

Figure S58. (a) Plot of S_{ads} vs $S_{diff} = D_{1,self}/D_{2,self}$, (b) Plot of Δq vs CO$_2$ uptake capacity, and (c) Plot of $S_{perm} = \Pi_1/\Pi_2$ vs CO$_2$ permeability, Π_1, for CO$_2$(1)/H$_2$(2) mixtures with $\frac{f_1}{f_1+f_2} \equiv y_1 = 0.15 = 1 - y_2$ in all-silica zeolites (CHA, DDR, FAU, MFI), cation-exchanged zeolites (NaY, NaX), MgMOF-74, and ZIF-8 at $f_t = f_1 + f_2$ = 1 MPa and temperature T = 300 K.

11 SAPO-34 membrane permeation

SAPO-34 has the same structural topology as CHA zeolite, consisting of cages of volume 316 Å^3, separated by 3.8 Å × 4.2 Å 8-ring windows.[66-69]

For adsorption in SAPO-34, the model based on statistical thermodynamics described in Chapter 3 of Ruthven[45] is particularly relevant and useful

$$q_i = \frac{q_{i,sat}}{\Omega_i} \frac{b_i f_i + \sum_{m=2}^{\Omega_i} \frac{(b_i f_i)^m}{(m-1)!} \left[\frac{1 - \frac{m}{\Omega_i + 1}}{1 - \frac{1}{\Omega_i + 1}} \right]^m}{1 + b_i f_i + \sum_{m=2}^{\Omega_i} \frac{(b_i f_i)^m}{(m)!} \left[\frac{1 - \frac{m}{\Omega_i + 1}}{1 - \frac{1}{\Omega_i + 1}} \right]^m} \tag{S53}$$

In Equation (S53) q_i represents the loading in mol kg^{-1}, $q_{i,sat}$ is the saturation loading in mol kg^{-1}, and Ω_i is maximum capacity expressed in molecules per cage. Based on the atomic composition of SAPO-34 used in our experiments of Li et al.,[70] $(Si_{0.061}Al_{0.483}P_{0.455})O_2$, we calculate $q_{i,sat} = 1.369\Omega_i$.

The unary isotherms fit parameters are provided in Table S12.

The mixture adsorption equilibrium was determined using the IAST.

Experimental data of Li et al.[70-72] for component permeances for CO_2/CH_4, CO_2/H_2, CO_2/N_2, CH_4/H_2, CH_4/N_2, CH_4/Ar, and N_2/H_2 mixtures in SAPO-34 membrane at 295 K are compared to unary permeation data in Figure S59, Figure S60, Figure S61, Figure S62, Figure S63, Figure S64, Figure S65. The permeance data are plotted as function of upstream partial pressures, $p_{i0.}$

Experimental data of Li et al.[70-72] for permeances of CO_2, CH_4, N_2, and H_2 determined for unary and equimolar binary mixture permeation across SAPO-34 membrane at 295 K are presented in Figure S66 as function of the adsorption potential $\pi A/RT$, calculated at the upstream face of membrane.

11.1 List of Tables for SAPO-34 membrane permeation

Table S12. Pure component isotherm fit data for guest species in SAPO-34, as tabulated in Li et al.[70]

Molecule	b_i	Ω_i	$q_{i,sat}$
CO_2	7.67×10^{-5}	6	8.2
CH_4	5.87×10^{-6}	6	8.2
N_2	1.26×10^{-6}	6	8.2
H_2	2.84×10^{-7}	9	12.3
O_2	1.2×10^{-6}	6	8.2
CO	2.31×10^{-6}	6	8.2
Ar	1.26×10^{-6}	6	8.2

b_i is expressed in Pa^{-1}, Ω_i in molecules per cage, $q_{i,sat}$ in mol kg^{-1}.

11.2 List of Figures for SAPO-34 membrane permeation

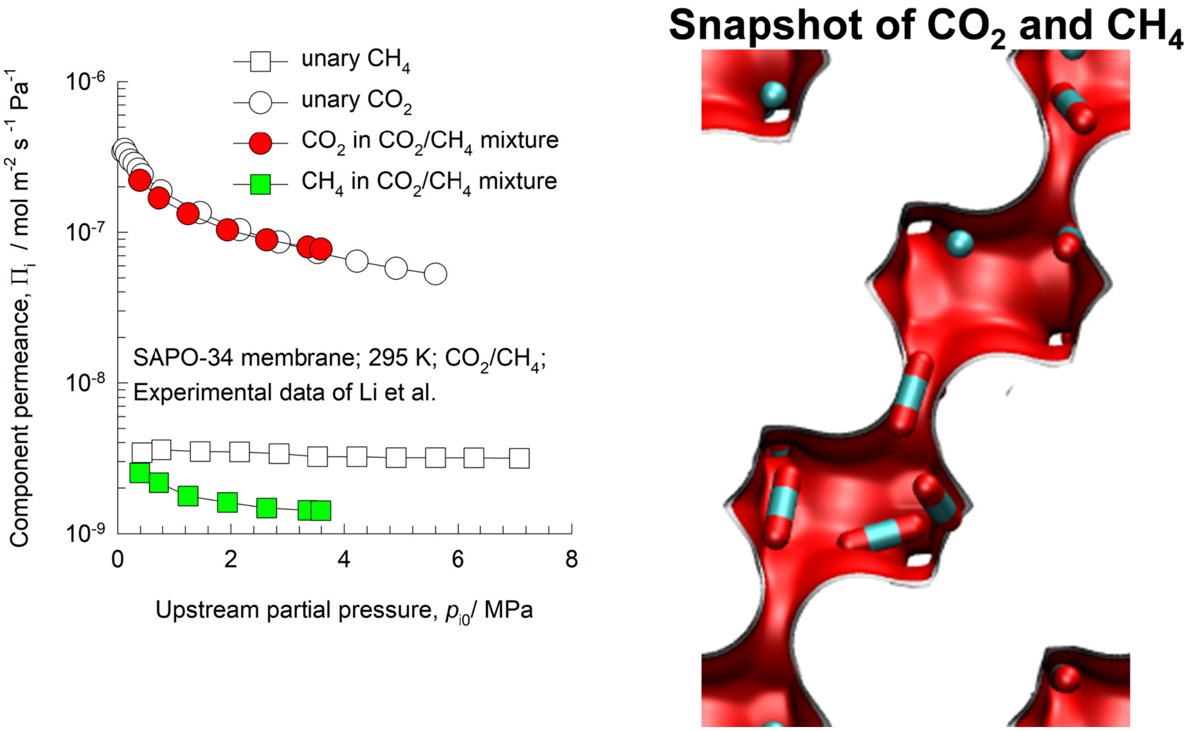

Figure S59. Experimental data for component permeances for CO_2/CH_4 mixtures in SAPO-34 membrane at 295 K, compared to unary permeation data. The data are plotted as function of upstream partial pressures, p_{i0}.

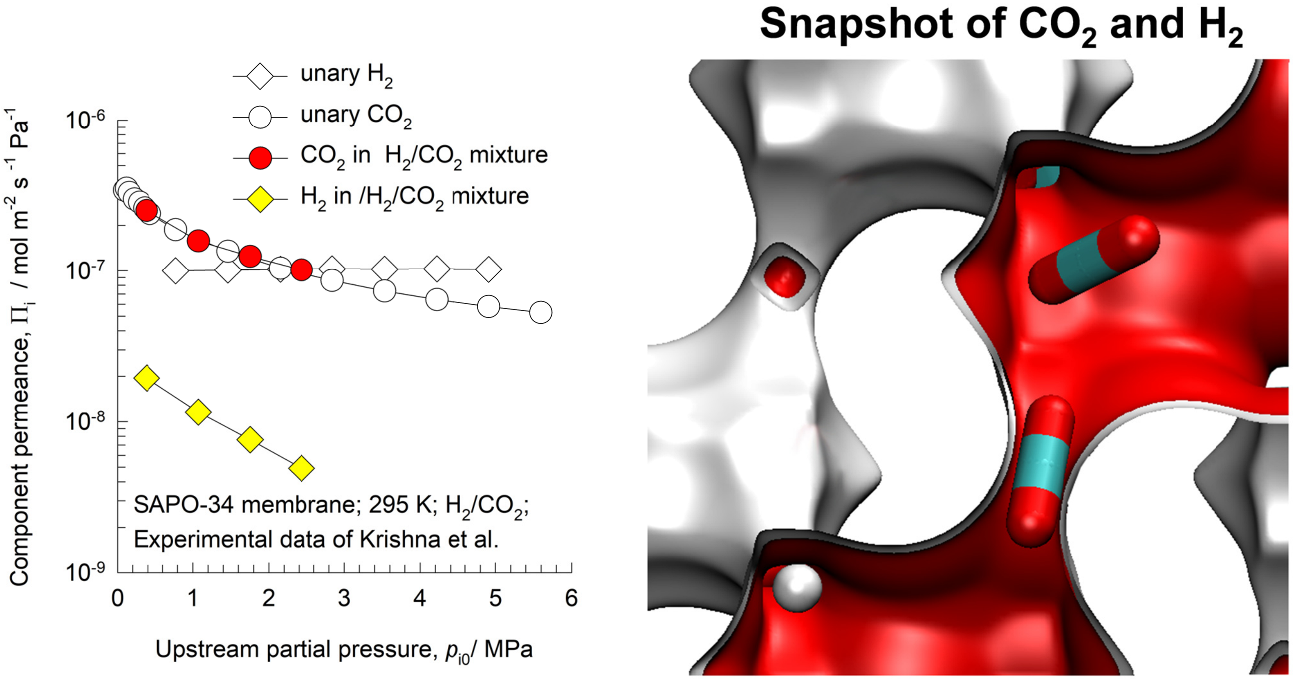

Figure S60. Experimental data for component permeances for CO_2/H_2 mixtures in SAPO-34 membrane at 295 K, compared to unary permeation data. The data are plotted as function of upstream partial pressures, p_{i0}.

SAPO-34 membrane permeation

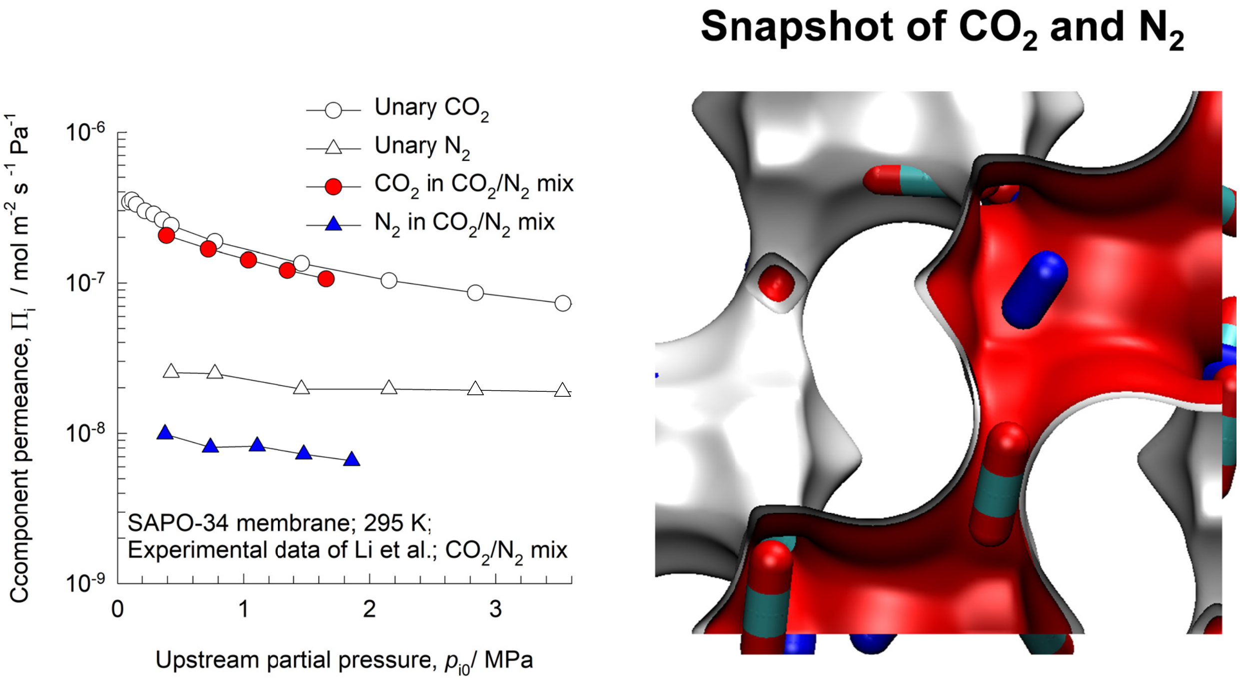

Figure S61. Experimental data for component permeances for CO$_2$/N$_2$ mixtures in SAPO-34 membrane at 295 K, compared to unary permeation data. The data are plotted as function of upstream partial pressures, p_{i0}.

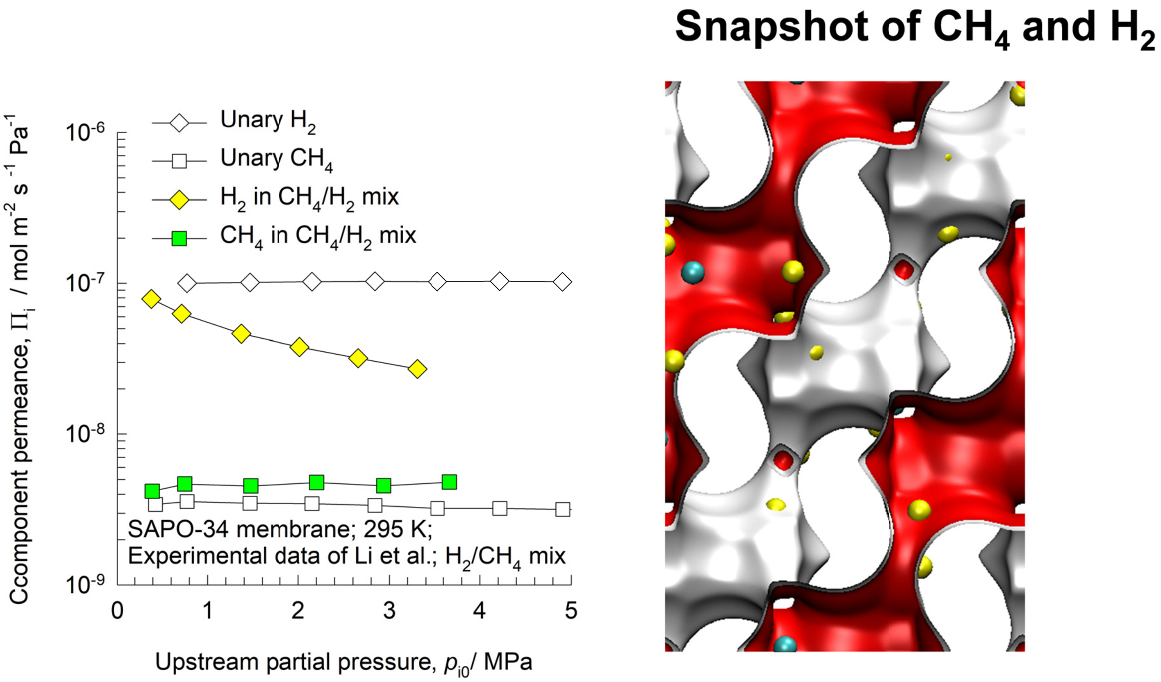

Figure S62. Experimental data for component permeances for CH_4/H_2 mixtures in SAPO-34 membrane at 295 K, compared to unary permeation data. The data are plotted as function of upstream partial pressures, p_{i0}.

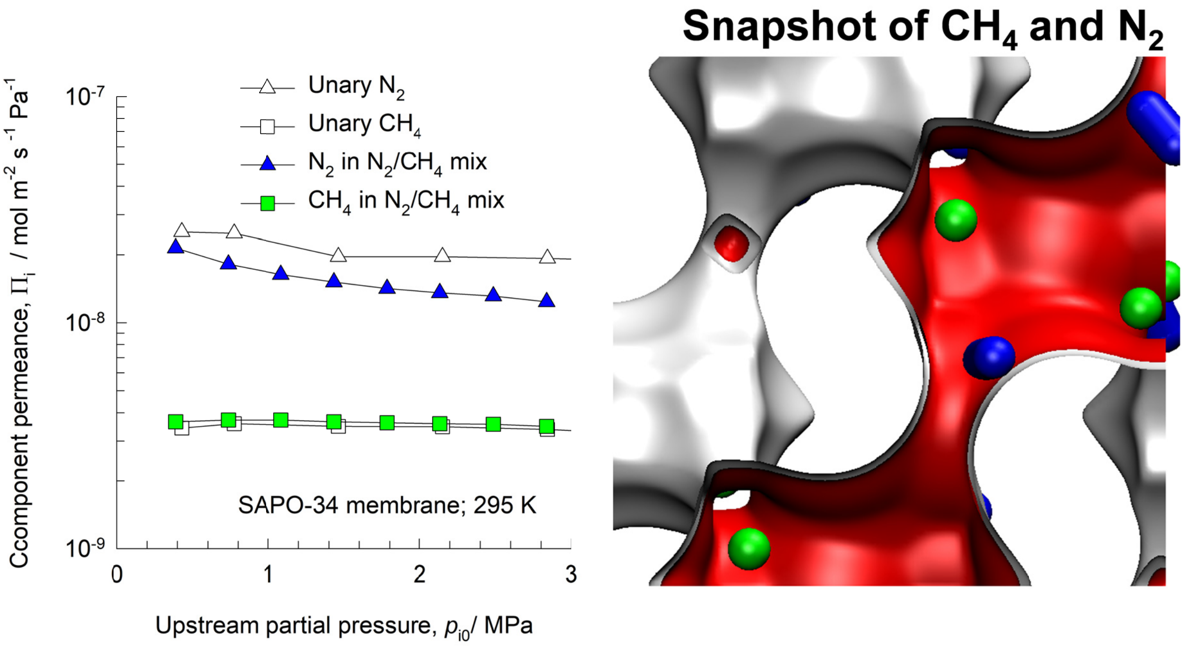

Figure S63. Experimental data for component permeances for CH_4/N_2 mixtures in SAPO-34 membrane at 295 K, compared to unary permeation data. The data are plotted as function of upstream partial pressures, p_{i0}.

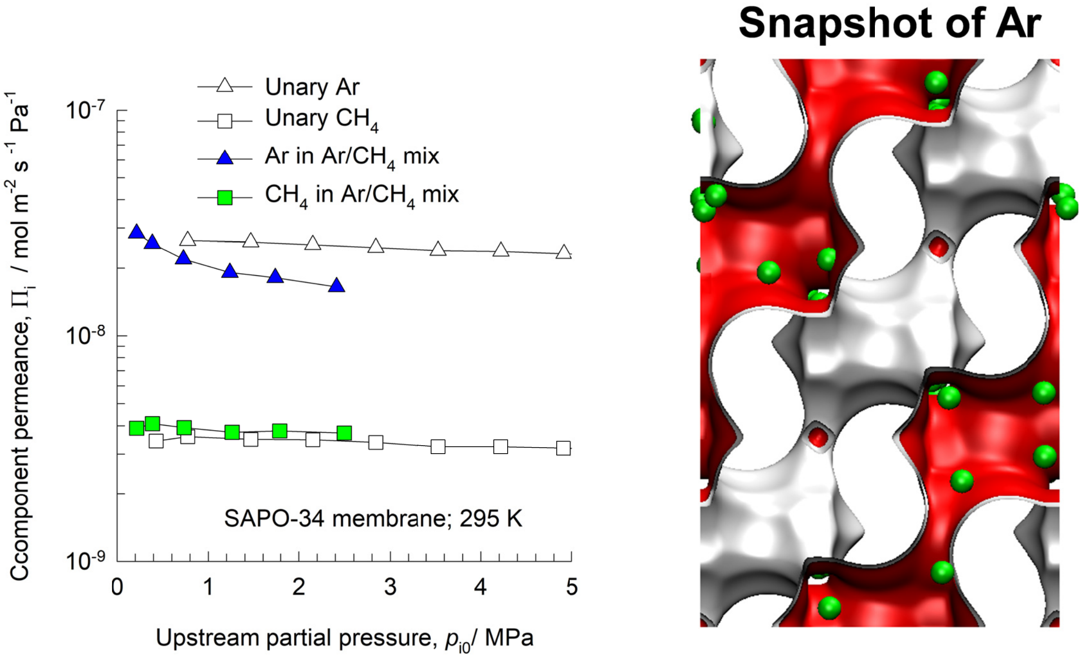

Figure S64. Experimental data for component permeances for CH_4/Ar mixtures in SAPO-34 membrane at 295 K, compared to unary permeation data. The data are plotted as function of upstream partial pressures, p_{i0}.

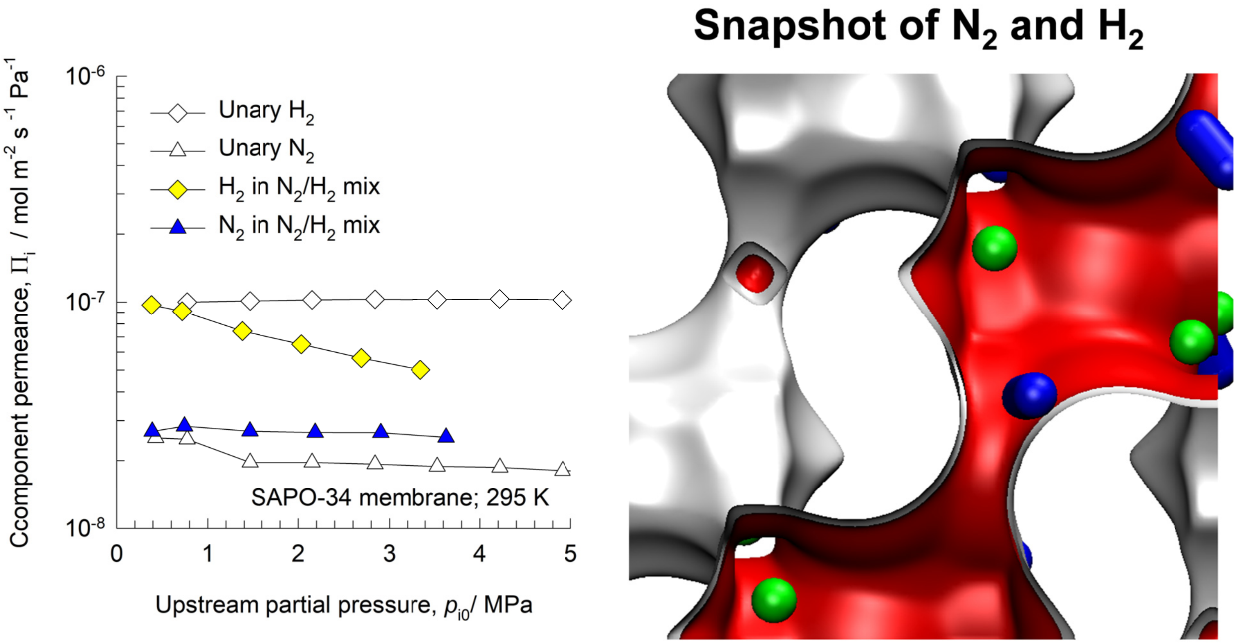

Figure S65. Experimental data for component permeances for N_2/H_2 mixtures in SAPO-34 membrane at 295 K, compared to unary permeation data. The data are plotted as function of upstream partial pressures, p_{i0}.

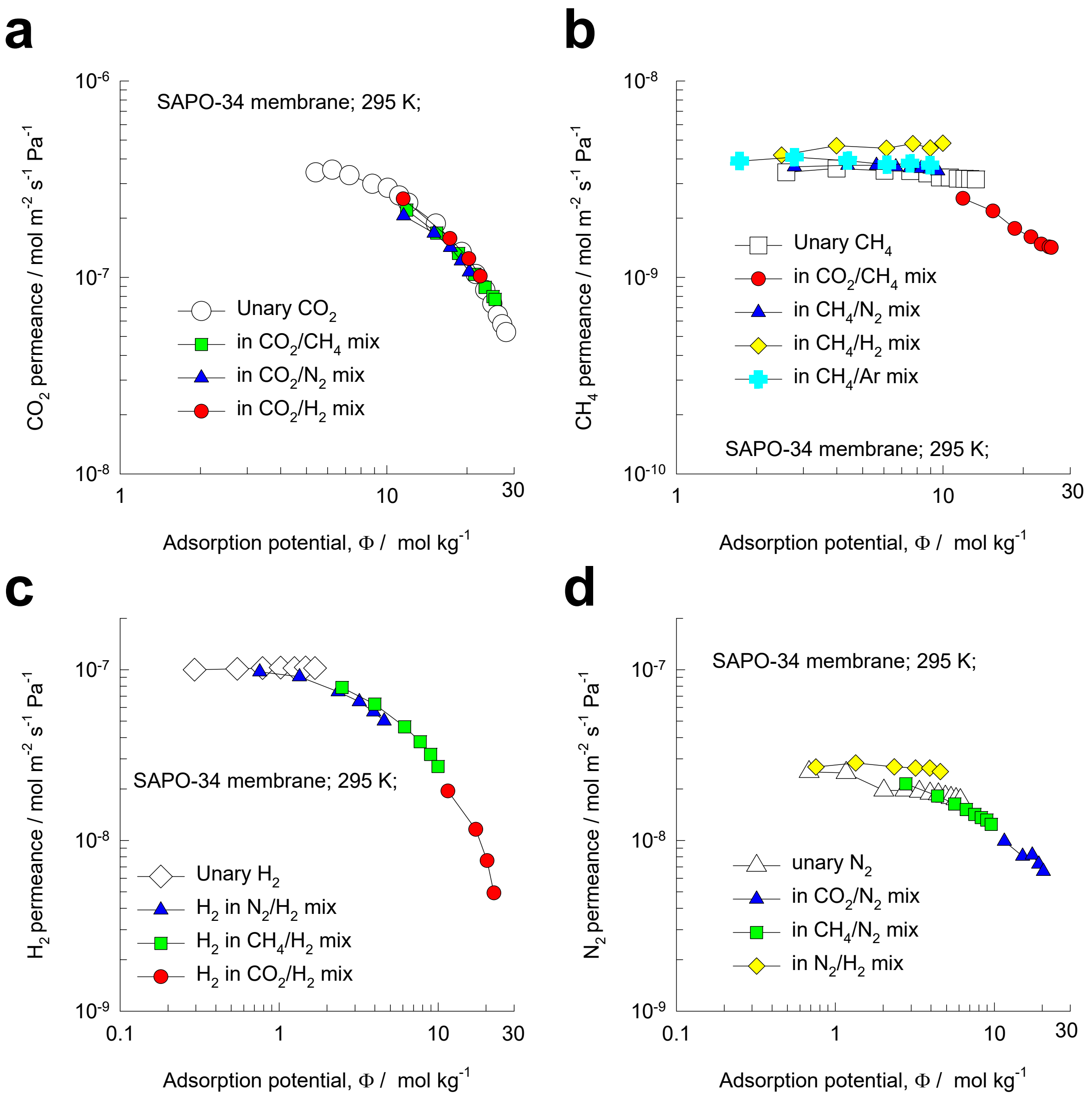

Figure S66. Re-analysis of the experimental data for permeances of (a) CO_2, (b) CH_4, (c) H_2, and (d) N_2 determined for unary and equimolar binary mixture permeation across SAPO-34 membrane at 295 K. The data are plotted as function of the adsorption potential $\Phi \equiv \pi A / RT$ at the upstream face of the membrane.

12 Nomenclature

Latin alphabet

A	surface area per kg of framework, $\mathrm{m^2\ kg^{-1}}$
A_{12}, A_{21}	Margules parameters, dimensionless
b_A	dual-Langmuir-Freundlich constant for species *i* at adsorption site A, $\mathrm{Pa}^{-\nu A}$
b_B	dual-Langmuir-Freundlich constant for species *i* at adsorption site B, $\mathrm{Pa}^{-\nu B}$
C	constant used in eq (S35) and eq (S39), $\mathrm{kg\ mol^{-1}}$
$D_\mathrm{i,self}$	self-diffusivity of species *i*, $\mathrm{m^2\ s^{-1}}$
f_i	partial fugacity of species *i*, Pa
f_t	total fugacity of bulk fluid mixture, Pa
n	number of species in the mixture, dimensionless
N_i	molar flux of species *i* with respect to framework, $\mathrm{mol\ m^{-2}\ s^{-1}}$
p_i	partial pressure of species *i* in mixture, Pa
p_t	total system pressure, Pa
P_i^0	sorption pressure, Pa
q_i	component molar loading of species *i*, $\mathrm{mol\ kg^{-1}}$
$q_\mathrm{i,sat}$	molar loading of species *i* at saturation, $\mathrm{mol\ kg^{-1}}$
q_t	total molar loading in mixture, $\mathrm{mol\ kg^{-1}}$
R	gas constant, 8.314 $\mathrm{J\ mol^{-1}\ K^{-1}}$
S_ads	adsorption selectivity, dimensionless
S_diff	diffusion selectivity, dimensionless
S_perm	permeation selectivity, dimensionless

Nomenclature

T	absolute temperature, K
V_p	accessible pore volume, m^3 kg^{-1}
x_i	mole fraction of species *i* in adsorbed phase, dimensionless
y_i	mole fraction of species *i* in bulk gas phase, dimensionless

Greek alphabet

δ	thickness of membrane, m
γ_i	activity coefficient of component *i* in adsorbed phase, dimensionless
Λ_{ij}	Wilson parameters, dimensionless
μ_i	molar chemical potential of component *i*, J mol^{-1}
π	spreading pressure, N m^{-1}
θ	fractional occupancy, dimensionless
Θ_i	loading of species *i*, molecules per unit cell
$\Theta_{i,sat}$	saturation loading of species *i*, molecules per unit cell
Θ_t	total mixture loading, molecules per unit cage, or per unit cell
ν	exponent in dual-Langmuir-Freundlich isotherm, dimensionless
Π_i	membrane permeability of species *i*, mol m m^{-2} s^{-1} Pa^{-1}
ρ	framework density, kg m^{-3}
Φ	adsorption potential, mol kg^{-1}

Subscripts

1	referring to component 1
2	referring to component 2
i	referring to component *i*

t	referring to total mixture
sat	referring to saturation conditions
δ	referring to conditions at downstream face of membrane

13 References

(1) Baerlocher, C.; Meier, W. M.; Olson, D. H. *Atlas of Zeolite Framework Types*. 5th Edition, Elsevier: Amsterdam, 2002.

(2) Baerlocher, C.; McCusker, L. B. Database of Zeolite Structures. http://www.iza-structure.org/databases/, International Zeolite Association, 10 January 2002.

(3) Krishna, R. Diffusion in Porous Crystalline Materials. *Chem. Soc. Rev.* **2012**, *41*, 3099-3118.

(4) Krishna, R. The Maxwell-Stefan Description of Mixture Diffusion in Nanoporous Crystalline Materials. *Microporous Mesoporous Mater.* **2014**, *185*, 30-50.

(5) Krishna, R. Describing the Diffusion of Guest Molecules inside Porous Structures. *J. Phys. Chem. C* **2009**, *113*, 19756-19781.

(6) Krishna, R.; van Baten, J. M. Investigating the Relative Influences of Molecular Dimensions and Binding Energies on Diffusivities of Guest Species Inside Nanoporous Crystalline Materials *J. Phys. Chem. C* **2012**, *116*, 23556-23568.

(7) Krishna, R.; van Baten, J. M. Investigating the Influence of Diffusional Coupling on Mixture Permeation across Porous Membranes *J. Membr. Sci.* **2013**, *430*, 113-128.

(8) Krishna, R.; van Baten, J. M. Influence of Adsorption Thermodynamics on Guest Diffusivities in Nanoporous Crystalline Materials. *Phys. Chem. Chem. Phys.* **2013**, *15*, 7994-8016.

(9) Krishna, R.; van Baten, J. M. Insights into diffusion of gases in zeolites gained from molecular dynamics simulations. *Microporous Mesoporous Mater.* **2008**, *109*, 91-108.

(10) Krishna, R.; van Baten, J. M. Diffusion of alkane mixtures in MFI zeolite. *Microporous Mesoporous Mater.* **2008**, *107*, 296-298.

(11) Krishna, R.; van Baten, J. M. In silico screening of metal-organic frameworks in separation applications. *Phys. Chem. Chem. Phys.* **2011**, *13*, 10593-10616.

(12) Krishna, R.; van Baten, J. M. In Silico Screening of Zeolite Membranes for CO_2 Capture. *J. Membr. Sci.* **2010**, *360*, 323-333.

(13) Krishna, R.; van Baten, J. M. Describing Mixture Diffusion in Microporous Materials under Conditions of Pore Saturation. *J. Phys. Chem. C* **2010**, *114*, 11557-11563.

(14) Krishna, R.; van Baten, J. M. Diffusion of alkane mixtures in zeolites. Validating the Maxwell-Stefan formulation using MD simulations. *J. Phys. Chem. B* **2005**, *109*, 6386-6396.

(15) Ryckaert, J. P.; Bellemans, A. Molecular dynamics of liquid alkanes. *Faraday Discuss. Chem. Soc.* **1978**, *66*, 95-106.

(16) Dubbeldam, D.; Calero, S.; Vlugt, T. J. H.; Krishna, R.; Maesen, T. L. M.; Smit, B. United Atom Forcefield for Alkanes in Nanoporous Materials. *J. Phys. Chem. B* **2004**, *108*, 12301-12313.

(17) Kumar, A. V. A.; Jobic, H.; Bhatia, S. K. Quantum effects on adsorption and diffusion of hydrogen and deuterium in microporous materials *J. Phys. Chem. B* **2006**, *110*, 16666-16671.

(18) Makrodimitris, K.; Papadopoulos, G. K.; Theodorou, D. N. Prediction of permeation properties of CO_2 and N_2 through silicalite via molecular simulations. *J. Phys. Chem. B* **2001**, *105*, 777-788.

(19) García-Pérez, E.; Parra, J. B.; Ania, C. O.; García-Sánchez, A.; Van Baten, J. M.; Krishna, R.; Dubbeldam, D.; Calero, S. A computational study of CO_2, N_2 and CH_4 adsorption in zeolites. *Adsorption* **2007**, *13*, 469-476.

(20) García-Sánchez, A.; Ania, C. O.; Parra, J. B.; Dubbeldam, D.; Vlugt, T. J. H.; Krishna, R.; Calero, S. Development of a Transferable Force Field for Carbon Dioxide Adsorption in Zeolites. *J. Phys. Chem. C* **2009**, *113*, 8814-8820.

(21) Banerjee, R.; Phan, A.; Wang, B.; Knobler, C.; Furukawa, H.; O'Keeffe, M.; Yaghi, O. M. High-Throughput Synthesis of Zeolitic Imidazolate Frameworks and Application to CO_2 Capture. *Science* **2008**, *319*, 939-943.

(22) Britt, D.; Furukawa, H.; Wang, B.; Glover, T. G.; Yaghi, O. M. Highly efficient separation of carbon dioxide by a metal-organic framework replete with open metal sites. *Proc. Natl. Acad. Sci. U.S.A.* **2009**, *106*, 20637-20640.

(23) Rosi, N. L.; Kim, J.; Eddaoudi, M.; Chen, B.; O'Keeffe, M.; Yaghi, O. M. Rod Packings and Metal-Organic Frameworks Constructed from Rod-Shaped Secondary Building Units. *J. Am. Chem. Soc.* **2005**, *127*, 1504-1518.

(24) Dietzel, P. D. C.; Panella, B.; Hirscher, M.; Blom, R.; Fjellvåg, H. Hydrogen adsorption in a nickel based coordination polymer with open metal sites in the cylindrical cavities of the desolvated framework. *Chem. Commun.* **2006**, 959-961.

(25) Dietzel, P. D. C.; Besikiotis, V.; Blom, R. Application of metal–organic frameworks with coordinatively unsaturated metal sites in storage and separation of methane and carbon dioxide. *J. Mater. Chem.* **2009**, *19*, 7362-7370.

(26) Caskey, S. R.; Wong-Foy, A. G.; Matzger, A. J. Dramatic Tuning of Carbon Dioxide Uptake via Metal Substitution in a Coordination Polymer with Cylindrical Pores. *J. Am. Chem. Soc.* **2008**, *130*, 10870-10871.

(27) Yazaydın, A. Ö.; Snurr, R. Q.; Park, T. H.; Koh, K.; Liu, J.; LeVan, M. D.; Benin, A. I.; Jakubczak, P.; Lanuza, M.; Galloway, D. B.; Low, J. J.; Willis, R. R. Screening of Metal-Organic Frameworks for Carbon Dioxide Capture from Flue Gas using a Combined Experimental and Modeling Approach. *J. Am. Chem. Soc.* **2009**, *131*, 18198-18199.

(28) Rappé, A. K.; Casewit, C. J.; Colwel, K. S.; Goddard, W. A.; Skiff, W. M. UFF, A Full Periodic Table Force Field for Molecular Mechanics and Molecular Dynamics Simulations. *J. Am. Chem. Soc.* **1992**, *114*, 10024-10035.

(29) Mayo, S. L.; Olafson, B. D.; Goddard, W. A. DREIDING: A Generic Force Field for Molecular Simulations. *J. Phys. Chem.* **1990**, *94*, 8897-8909.

(30) Yang, Q.; Zhong, C. Understanding Hydrogen Adsorption in Metal-Organic Frameworks with Open Metal Sites: A Computational Study. *J. Phys. Chem. B* **2006**, *110*, 655-658.

(31) Jorgensen, W. L.; Maxwell, D. S.; Tirado-Rives, J. Development and Testing of the OPLS All-Atom Force Field on Conformational Energetics and Properties of Organic Liquids. *J. Am. Chem. Soc.* **1996**, *118*, 11225-11236.

(32) Zhou, M.; Wang, Q.; Zhang, L.; Liu, Y. C.; Kang, Y. Adsorption Sites of Hydrogen in Zeolitic Imidazolate Frameworks. *J. Phys. Chem. B* **2009**, *113*, 11049-11053.

(33) Xu, Q.; Zhong, C. A General Approach for Estimating Framework Charges in Metal-Organic Frameworks. *J. Phys. Chem. C* **2010**, *114*, 5035-5042.

(34) Myers, A. L.; Monson, P. A. Adsorption in Porous Materials at High Pressure: Theory and Experiment. *Langmuir* **2002**, *18*, 10261-10273.

(35) Babarao, R.; Hu, Z.; Jiang, J.; Chempath, S.; Sandler, S. I. Storage and separation of CO_2 and CH_4 in silicalite, C_{168} schwarzite, and IRMOF-1: A comparative study from Monte Carlo simulation. *Langmuir* **2007**, *23*, 659-666.

(36) Babarao, R.; Jiang, J. Exceptionally high CO_2 storage in covalent-organic frameworks: Atomistic simulation study. *Energy Environ. Sci.* **2008**, *1*, 139-143.

(37) Frenkel, D.; Smit, B. *Understanding Molecular Simulations: From Algorithms to Applications*. 2nd Edition, Academic Press: San Diego, 2002.

(38) Talu, O.; Myers, A. L. Molecular Simulation of Adsorption: Gibbs Dividing Surface and Comparison with Experiment. *A.I.Ch.E.J.* **2001**, *47*, 1160-1168.

(39) Skoulidas, A. I.; Sholl, D. S. Transport diffusivities of CH_4, CF_4, He, Ne, Ar, Xe, and SF_6 in silicalite from atomistic simulations. *J. Phys. Chem. B* **2002**, *106*, 5058-5067.

(40) Düren, T.; Millange, F.; Férey, G.; Walton, K. S.; Snurr, R. Q. Calculating Geometric Surface Areas as a Characterization Tool for Metal-Organic Frameworks. *J. Phys. Chem. C* **2007**, *111*, 15350-15356.

(41) Foster, M. D.; Rivin, I.; Treacy, M. M. J.; Friedrichs, O. D. A geometric solution to the largest-free-sphere problem in zeolite frameworks. *Microporous Mesoporous Mater.* **2006**, *90*, 32-38.

(42) Smith, W.; Forester, T. R.; Todorov, I. T. The DL_POLY Molecular Simulation Package. http://www.cse.clrc.ac.uk/msi/software/DL_POLY/index.shtml, Warrington, England, March 2006.

(43) SARA Computing & Networking Services. https://subtrac.sara.nl/userdoc/wiki/lisa/description, Amsterdam, 16 January 2008.

(44) Myers, A. L.; Prausnitz, J. M. Thermodynamics of Mixed Gas Adsorption. *A.I.Ch.E.J.* **1965**, *11*, 121-130.

(45) Ruthven, D. M. *Principles of Adsorption and Adsorption Processes*. John Wiley: New York, 1984.

(46) Talu, O.; Myers, A. L. Rigorous Thermodynamic Treatment of Gas-Adsorption. *A.I.Ch.E.J.* **1988**, *34*, 1887-1893.

(47) Siperstein, F. R.; Myers, A. L. Mixed-Gas Adsorption. *A.I.Ch.E.J.* **2001**, *47*, 1141-1159.

(48) Krishna, R.; Van Baten, J. M. Elucidation of Selectivity Reversals for Binary Mixture Adsorption in Microporous Adsorbents. *ACS Omega* **2020**, *5*, 9031-9040. https://doi.org/10.1021/acsomega.0c01051.

(49) Krishna, R.; Van Baten, J. M. Using Molecular Simulations for Elucidation of Thermodynamic Non-Idealities in Adsorption of CO_2-containing Mixtures in NaX Zeolite. *ACS Omega* **2020**, *5*, 20535-20542. https://doi.org/10.1021/acsomega.0c02730.

(50) Krishna, R.; Van Baten, J. M. Water/Alcohol Mixture Adsorption in Hydrophobic Materials: Enhanced Water Ingress caused by Hydrogen Bonding. *ACS Omega* **2020**, *5*, 28393-28402. https://doi.org/10.1021/acsomega.0c04491.

(51) Krishna, R.; Van Baten, J. M. Investigating the Non-idealities in Adsorption of CO_2-bearing Mixtures in Cation-exchanged Zeolites. *Sep. Purif. Technol.* **2018**, *206*, 208-217. https://doi.org/10.1016/j.seppur.2018.06.009.

(52) Krishna, R. Occupancy Dependency of Maxwell−Stefan Diffusivities in Ordered Crystalline Microporous Materials. *ACS Omega* **2018**, *3*, 15743-15753. https://doi.org/10.1021/acsomega.8b02465.

(53) Talu, O.; Zwiebel, I. Multicomponent Adsorption Equilibria of Nonideal Mixtures. *A.I.Ch.E.J.* **1986**, *32*, 1263-1276.

(54) Krishna, R.; van Baten, J. M. Unified Maxwell-Stefan Description of Binary Mixture Diffusion in Micro- and Meso- Porous Materials. *Chem. Eng. Sci.* **2009**, *64*, 3159-3178.

(55) Krishna, R.; van Baten, J. M. Onsager coefficients for binary mixture diffusion in nanopores. *Chem. Eng. Sci.* **2008**, *63*, 3120-3140.

(56) Krishna, R. Adsorptive separation of $CO_2/CH_4/CO$ gas mixtures at high pressures. *Microporous Mesoporous Mater.* **2012**, *156*, 217-223.

(57) Krishna, R.; van Baten, J. M. Investigating the potential of MgMOF-74 membranes for CO_2 capture. *J. Membr. Sci.* **2011**, *377*, 249-260.

(58) Krishna, R.; van Baten, J. M. Maxwell-Stefan modeling of slowing-down effects in mixed gas permeation across porous membranes. *J. Membr. Sci.* **2011**, *383*, 289-300.

(59) Krishna, R.; van Baten, J. M. Investigating the Validity of the Knudsen Prescription for Diffusivities in a Mesoporous Covalent Organic Framework. *Ind. Eng. Chem. Res.* **2011**, *50*, 7083-7087.

(60) Krishna, R.; van Baten, J. M. Investigating the Validity of the Bosanquet Formula for Estimation of Diffusivities in Mesopores. *Chem. Eng. Sci.* **2012**, *69*, 684-688.

References

(61) Krishna, R.; van Baten, J. M.; Baur, R. Highlighting the Origins and Consequences of Thermodynamic Nonidealities in Mixture Separations using Zeolites and Metal-Organic Frameworks. *Microporous Mesoporous Mater.* **2018**, *267*, 274-292. http://dx.doi.org/10.1016/j.micromeso.2018.03.013.

(62) Krishna, R.; van Baten, J. M. Segregation effects in adsorption of CO_2 containing mixtures and their consequences for separation selectivities in cage-type zeolites. *Sep. Purif. Technol.* **2008**, *61*, 414-423.

(63) Krishna, R. Screening Metal-Organic Frameworks for Mixture Separations in Fixed-Bed Adsorbers using a Combined Selectivity/Capacity Metric. *RSC Adv.* **2017**, *7*, 35724-35737. https://doi.org/10.1039/C7RA07363A.

(64) Krishna, R. Methodologies for Screening and Selection of Crystalline Microporous Materials in Mixture Separations. *Sep. Purif. Technol.* **2018**, *194*, 281-300. https://doi.org/10.1016/j.seppur.2017.11.056.

(65) Krishna, R. Metrics for Evaluation and Screening of Metal-Organic Frameworks for Applications in Mixture Separations. *ACS Omega* **2020**, *5*, 16987−17004. https://doi.org/10.1021/acsomega.0c02218.

(66) Olson, D. H.; Camblor, M. A.; Vallaescusa, L. A.; Kuehl, G. H. Light hydrocarbon sorption properties of pure silica Si-CHA and ITQ-3 and high silica ZSM-58. *Microporous Mesoporous Mater.* **2004**, *67*, 27-33.

(67) Hedin, N.; DeMartin, G. J.; Roth, W. J.; Strohmaier, K. G.; Reyes, S. C. PFG NMR self-diffusion of small hydrocarbons in high silica DDR, CHA and LTA structures. *Microporous Mesoporous Mater.* **2008**, *109*, 327-334.

(68) Ruthven, D. M.; Reyes, S. C. Adsorptive separation of light olefins from paraffins. *Microporous Mesoporous Mater.* **2007**, *104*, 59-66.

(69) Khalighi, M.; Chen, Y. F.; Farooq, S.; Karimi, I. A.; Jiang, J. W. Propylene/Propane Separation Using SiCHA. *Ind. Eng. Chem. Res.* **2013**, *52*, 3877-3892.

(70) Li, S.; Falconer, J. L.; Noble, R. D.; Krishna, R. Interpreting unary, binary and ternary mixture permeation across a SAPO-34 membrane with loading-dependent Maxwell-Stefan diffusivities. *J. Phys. Chem. C* **2007**, *111*, 5075-5082.

(71) Li, S.; Falconer, J. L.; Noble, R. D.; Krishna, R. Modeling permeation of CO_2/CH_4, CO_2/N_2, and N_2/CH_4 mixtures across SAPO-34 membrane with the Maxwell-Stefan equations. *Ind. Eng. Chem. Res.* **2007**, *46*, 3904-3911.

(72) Krishna, R.; Li, S.; van Baten, J. M.; Falconer, J. L.; Noble, R. D. Investigation of slowing-down and speeding-up effects in binary mixture permeation across SAPO-34 and MFI membranes. *Sep. Purif. Technol.* **2008**, *60*, 230-236.